molecular systems biology

Specificity, propagation, and memory of pericentric heterochromatin

Katharina Müller-Ott[1], Fabian Erdel[1], Anna Matveeva[2], Jan-Philipp Mallm[1], Anne Rademacher[1], Matthias Hahn[3], Caroline Bauer[1], Qin Zhang[2], Sabine Kaltofen[1,†], Gunnar Schotta[3], Thomas Höfer[2] & Karsten Rippe[1,*]

Abstract

The cell establishes heritable patterns of active and silenced chromatin via interacting factors that set, remove, and read epigenetic marks. To understand how the underlying networks operate, we have dissected transcriptional silencing in pericentric heterochromatin (PCH) of mouse fibroblasts. We assembled a quantitative map for the abundance and interactions of 16 factors related to PCH in living cells and found that stably bound complexes of the histone methyltransferase SUV39H1/2 demarcate the PCH state. From the experimental data, we developed a predictive mathematical model that explains how chromatin-bound SUV39H1/2 complexes act as nucleation sites and propagate a spatially confined PCH domain with elevated histone H3 lysine 9 trimethylation levels via chromatin dynamics. This "nucleation and looping" mechanism is particularly robust toward transient perturbations and stably maintains the PCH state. These features make it an attractive model for establishing functional epigenetic domains throughout the genome based on the localized immobilization of chromatin-modifying enzymes.

Introduction

Epigenetic networks control the accessibility of DNA for transcription, DNA repair, and replication machineries. They establish and maintain different functional chromatin states through cell division via protein factors that set or remove specific modifications of histones and DNA in the absence of alterations of the DNA sequence (Berger *et al*, 2009). These chromatin signals in turn recruit architectural chromatin components or chromatin remodeling factors in a highly dynamic manner and regulate genome access (McBryant *et al*, 2006; Taverna *et al*, 2007; Campos & Reinberg, 2009; Clapier & Cairns, 2009; Erdel *et al*, 2011a). On a global scale, the concerted and targeted activity of these networks results in the formation of the denser, transcriptionally repressed heterochromatin state and the more open and biologically active euchromatin, which can be distinguished at the resolution of the light microscope (Grewal & Jia, 2007; Eissenberg & Reuter, 2009). A prototypic example for a constitutive heterochromatin domain is pericentric heterochromatin (PCH) in mouse cells (Probst & Almouzni, 2008). It is characterized by its high content of repetitive major satellite repeats and repressive epigenetic marks such as 5-methylcytosine (5meC) the binding of proteins with a methyl-CpG-binding domain that recognize this modification, trimethylation of histone H3 lysine residue 9 (H3K9me3), and histone H4 lysine residue 20 (H4K20me3), as well as hypoacetylation of histones (Probst & Almouzni, 2008). The H3K9me3 modification is set by the histone methylases SUV39H1 and SUV39H2 (in the following "SUV39H" refers to both isoforms), while SUV4-20H1 and SUV4-20H2 set H4K20me2 and promote H4K20me3 ("SUV4-20H" for both isoforms) (Kwon & Workman, 2008; Schotta *et al*, 2008; Eissenberg & Reuter, 2009; Byrum *et al*, 2013).

A central protein component of PCH is heterochromatin protein 1 (HP1) that is present in three very similar isoforms HP1α, HP1β, and HP1γ in mice and humans (Maison & Almouzni, 2004; Hiragami & Festenstein, 2005; Kwon & Workman, 2008). HP1 contains an N-terminal chromodomain (CD) and a C-terminal chromoshadow-domain (CSD) connected by a flexible linker region. The CD interacts specifically with H3 histone tails that carry the K9me3 modification (Jacobs & Khorasanizadeh, 2002; Fischle *et al*, 2003). HP1 is able to form homo- and heterodimers (Nielsen *et al*, 2001; Yamamoto & Sonoda, 2003; Rosnoblet *et al*, 2011), interacts with SUV39H1 (Aagaard *et al*, 1999; Yamamoto & Sonoda, 2003), SUV4-20H2 (Schotta *et al*, 2004; Souza *et al*, 2009), the DNA methylase DNMT1 (Fuks *et al*, 2003; Lehnertz *et al*, 2003; Smallwood *et al*,

1 Deutsches Krebsforschungszentrum (DKFZ) and BioQuant, Research Group Genome Organization & Function, Heidelberg, Germany
2 Deutsches Krebsforschungszentrum (DKFZ) and BioQuant, Division Theoretical Systems Biology, Heidelberg, Germany
3 Munich Center for Integrated Protein Science and Adolf Butenandt Institute, Ludwig Maximilians University, Munich, Germany
*Corresponding author. Tel: +49 6221 5451376; Fax: +49 6221 5451487; E-mail: karsten.rippe@dkfz.de
†Present address: Biochemistry & Structural Biology, Lund University, Lund, Sweden

2007) as well as the methyl-CpG-binding proteins MBD1 and MECP2 (Fujita *et al*, 2003; Agarwal *et al*, 2007). SUV39H1 interacts with the DNA methylation-associated proteins DNMT1, MBD1, and MECP2 (Lunyak *et al*, 2002; Fujita *et al*, 2003; Fuks *et al*, 2003; Esteve *et al*, 2006). Thus, a complex protein–protein interaction network exists in PCH. The interactions constituting this network in mammalian cells have been studied mostly *in vitro* or via immunoprecipitation experiments and have not been probed comprehensively in living cells.

Since HP1 interacts with SUV39H via its CSD, a feedback loop of HP1 binding-mediated H3K9 methylation has been proposed as a mechanism for propagating the H3K9me3 mark to adjacent nucleosomes (Schotta *et al*, 2002; Grewal & Jia, 2007; Eissenberg & Reuter, 2009). Theoretical models based on a combination of such feedback loops have suggested the existence of two discrete chromatin states that can stably co-exist ("bistability") for a certain range of conditions (Schreiber & Bernstein, 2002; Dodd *et al*, 2007; Angel *et al*, 2011). Hathaway *et al* have proposed an alternative, "monostable" model of heterochromatin propagation through interactions between neighboring nucleosomes (Hathaway *et al*, 2012). However, direct evidence on how such epigenetic networks might operate in living cells is lacking. In particular, three crucial questions remained unanswered: (i) How is the separation of the genome in active and silenced chromatin states established and maintained and what are the factors that provide *specificity* for distinct euchromatic and heterochromatic states? (ii) How is the *confinement* of a given chromatin state to a certain genomic locus achieved? For the case of a feedback loop between SUV39H, HP1, and H3K9me3 in PCH, it is elusive why the H3K9me3 does not spread throughout the whole genome. (iii) How is a given chromatin state like that of PCH transmitted through the cell cycle?

Here, we have set out to address these issues by dissecting the mouse pericentric heterochromatin network centered around the H3K9 and H4K20 methylation. This model system has the advantage that the corresponding heterochromatin domains can be readily identified on fluorescence microscopy images as chromatin-dense spots, the chromocenters. Accordingly, we were able to distinguish the features of PCH from the surrounding *bona fide* euchromatin. By applying a combination of fluorescence microscopy-based imaging, bleaching and correlation methods (Müller *et al*, 2009; Erdel *et al*, 2011b) in conjunction with quantitative mechanistic modeling, we identified distinct complexes of stably bound SUV39H

as the component that defines the PCH state. We further demonstrate that these SUV39H complexes represent "nucleation sites" that are sufficient to provide specificity, confined propagation of the H3K9me3 mark as well as cellular memory to transmit the PCH state through the cell cycle.

Results

The repressive PCH state is defined by enrichment of 5meC, MECP2, MBD1, and SUV39H

We quantitated the enrichment of the PCH-associated histone modifications H3K9me3, H4K20me3, the DNA methylation 5meC and the known proteins that set, remove, or recognize these modifications in the context of PCH in mouse NIH-3T3 fibroblasts: the histone H3K9 and histone H4K20 specific methylases SUV39H1, SUV39H2, SUV4-20H1, SUV4-20H2, all three isoforms of the H3K9me3-reader HP1 (HP1α, HP1β, and HP1γ), the histone demethylases JMJD2B and JMJD2C that remove H3K9me3, the DNA methylase DNMT1 as well as the methyl-CpG binding domain (MBD)-containing proteins MECP2, MBD1, MBD2, and MBD3 [see (Fodor *et al*, 2010) for a review of previously identified mammalian PCH components]. Furthermore, we included the transcription factors PAX3, PAX5, PAX7, and PAX9 in our analysis since a role for PAX3 in PCH assembly has been reported (Bulut-Karslioglu *et al*, 2012). Although the colocalization of these factors and histone marks with PCH was studied previously, a comprehensive quantitative analysis of their PCH-specificity and abundance has been lacking. Thus, we fluorescently labeled the factors of interest (Supplementary Fig S1) and determined the enrichment of GFP-tagged proteins in PCH using the workflow shown in Fig 1A: For each factor, the fluorescence intensity was measured in PCH as defined by foci with intense DAPI (4′,6-diamidino-2-phenylindole) staining and in the surrounding euchromatin of G1 phase cells. The enrichment of these factors in PCH was calculated, followed by normalization to the enrichment of core histone H2A and DAPI in PCH. Chromatin binding states were identified by fluorescence recovery after photobleaching (FRAP) and their enrichment in PCH was determined. Fluorescence correlation spectroscopy (FCS) was used to measure protein concentrations and the free diffusion coefficient in the cytoplasm, which served as a reference value. Protein enrichments, concentrations, chromatin

---

Figure 1. Quantitative analysis of core components of the pericentric heterochromatin (PCH) network.

A   Workflow of integrative PCH network analysis. The enrichment of different factors in PCH was measured based on confocal laser scanning microscopy (CLSM) images. Abundance and chromatin interactions were determined by fluorescence fluctuation microscopy methods (FRAP, FCS). Additional information on protein–protein interactions was obtained as described in the text and in Fig 2. Based on the experimental data, a network model was developed that explains the stable maintenance of PCH.

B   Enrichment of proteins, DNA methylation, H3K9me3, and H4K20me3 in PCH over euchromatic regions from fluorescence intensity measurements in G1 phase cells. The red line marks the chromatin compaction in PCH (1.8-fold enrichment of H2A-RFP). Labeled H2A, SUV39H1, and HP1 isoforms were stably expressed, the other proteins were transiently expressed, and modifications were immunostained. Error bars correspond to standard error of the mean (SEM).

C   Enrichment of transiently bound and immobilized protein fractions in PCH versus euchromatin determined by FRAP. Red lines indicate 2-fold and 10-fold enrichment levels. Error bars correspond to standard deviation (SD).

D   Absolute concentrations of stably bound proteins in the immobile FRAP fraction.

E   FRAP experiments of transiently expressed MBD1 and MECP2 in PCH and euchromatin (Eu). Data were fitted to yield chromatin binding parameters.

F   FRAP of SUV39H1 (stably expressed) and SUV39H2 (transiently expressed).

G   FRAP of transiently expressed SUV4-20H1 and SUV4-20H2.

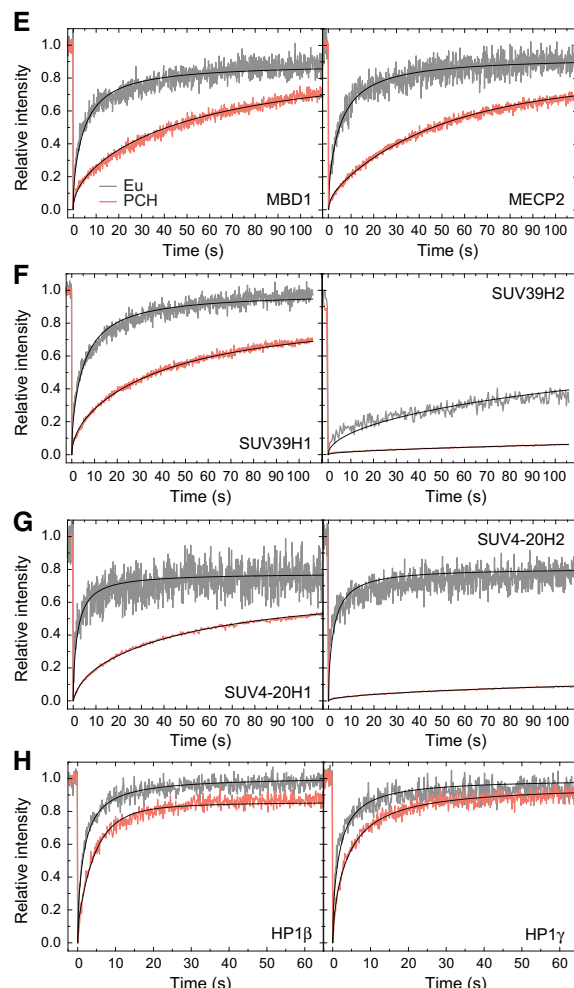H   FRAP of stably expressed HP1β and HP1γ. For additional data including HP1α, see Supplementary Table S2.

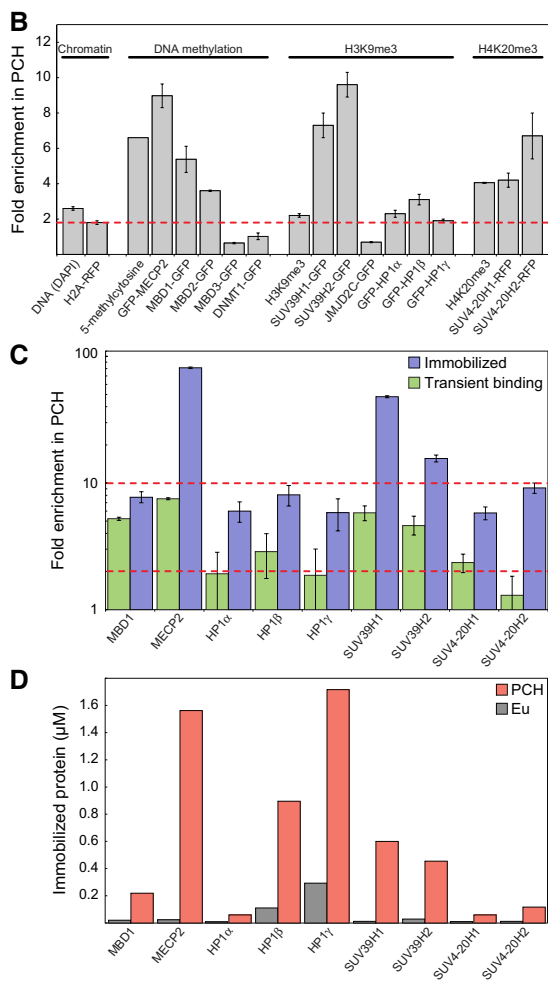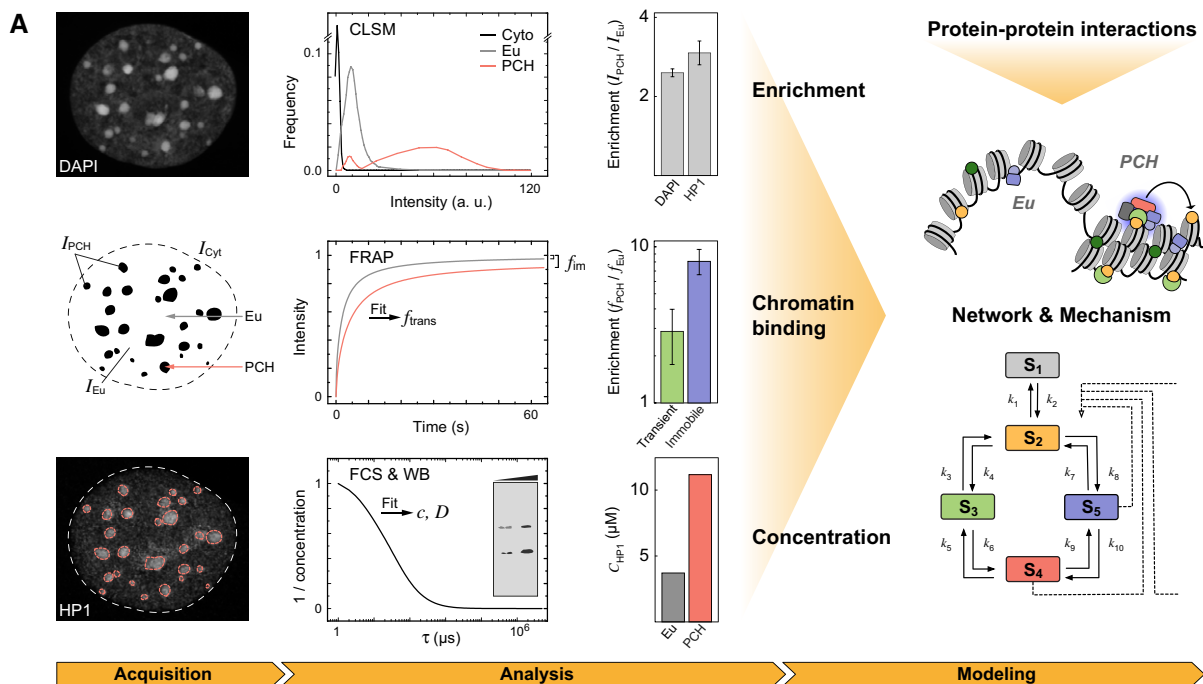**Figure 1.**

binding states, and protein–protein interactions were integrated into a quantitative molecular model for PCH.

PCH was about 1.8 ± 0.3-fold denser than euchromatin as determined from the H2A-RFP intensity, whereas the DNA stain with DAPI yielded a 2.7 ± 0.1-fold enrichment in PCH, possibly reflecting its binding preference for A/T-rich sequences. We conclude that chromatin is about 2-fold more compacted in PCH (Fig 1B). In terms of factors targeted to PCH during G1, we identified three different groups (Fig 1B): (i) Proteins displaying a diffuse distribution throughout the nucleus or a slight depletion in PCH, which is indicative of little PCH-specific interactions (JMJD2B/C, DNMT1, MBD3, and the PAX proteins). (ii) Factors whose PCH enrichment (2–3-fold) essentially followed the increased chromatin density and accordingly displayed only moderate specificity for PCH (MBD2, HP1, and H3K9me3). When normalized to the H2A-RFP chromatin density, the average enrichment of H3K9me3 in PCH was only 1.4 ± 0.2-fold. Measured values ranged from 0.8- to 1.6-fold between different experiments and antibodies used (Millipore and Abcam). (iii) Factors that were clearly enriched above the 2-fold DNA compaction in PCH and thus represent PCH-specific components (5meC, MECP2, MBD1, SUV39H, H4K20me3, SUV4-20H: ~4- to 10-fold). The PCH enrichment of 5meC measured by immunostaining varied between 2- and 5-fold, depending on antibody and fixation protocols used. From bisulfite sequencing data of major satellite repeats in NIH-3T3 cells, mouse embryonic stem cells (ESCs), and primary differentiated cells, we calculated an enrichment of 7 ± 1 (Wilson & Jones, 1984; Yamagata *et al*, 2007; Meissner *et al*, 2008; Arand *et al*, 2012).

To validate the functional role of SUV39H and H3K9me3 in PCH of our cellular system, we measured the abundance of satellite transcripts by quantitative real-time PCR in ESCs, immortalized mouse embryonic fibroblasts (iMEFs) and iMEFs that had *Suv39h1* and *Suv39h2* (iMEF *Suv39h* dn) deleted (Peters *et al*, 2001). The transcription levels of pericentric major satellites were 4.6 ± 0.2-fold higher in ESCs and 14 ± 2-fold higher in iMEF *Suv39h* dn cells as compared to fully differentiated iMEF wild-type (wt) cells (Supplementary Fig S2A). Thus, PCH-specific H3K9me3 levels in wild-type iMEFs, ESCs, and *Suv39h* dn iMEFs anti-correlate with satellite repeat transcription, in agreement with previous measurements (Lehnertz *et al*, 2003; Martens *et al*, 2005; Meshorer & Misteli, 2006). Importantly, the chromatin-dense chromocenters persisted in both *Suv39h* and *Suv4-20h* double null cells, showing that transcriptional silencing is not due to chromatin compaction *per se* (Supplementary Fig S2B and C). Decondensation of the chromocenters was only observed upon inhibition of histone deacetylation (Supplementary Fig S2D) in agreement with previous reports (Taddei *et al*, 2001). In summary, we conclude that the enrichment of 5meC as well as MECP2, MBD1, SUV39H1, and SUV39H2 proteins represent the hallmarks of PCH.

MECP2, SUV39H, and HP1 are the most abundant stably PCH-associated proteins

The above quantitative analysis of relative steady-state PCH enrichment levels lacks information on the absolute endogenous protein concentrations and does not resolve differences in binding kinetics. To address these issues, we integrated FCS and FRAP (Supplementary Fig S3A) (Müller *et al*, 2009). By combining quantitative FCS

and Western blot analysis, endogenous SUV39H and SUV4-20H concentrations were determined to be between 0.1–0.4 µM in euchromatin and 0.2–3.0 µM in PCH (Supplementary Fig S3B and C, Table 1, Supplementary Table S1). HP1 displayed the highest concentration of the factors studied of 19 ± 12 µM in euchromatin and 41 ± 25 µM in PCH, with HP1β and HP1γ being significantly more abundant than HP1α (Table 1, Supplementary Table S1). The diffusion coefficients measured by FCS in the cytoplasm were in the expected range and represent a reference value for the intracellular protein mobility of a given factor in the absence of chromatin interactions (Supplementary Table S1).

Chromatin binding in the nucleus was evaluated by FRAP (Fig 1E–H) with a reaction-diffusion analysis that yielded the effective diffusion coefficient D_{eff} (including transient binding interactions), the dissociation rate constant k_{off}, the pseudo on-rate k^*_{on} (including the free binding site concentration), and the protein fraction immobilized on the minute time scale (Supplementary Fig S3A). From these data, we calculated average protein residence times τ_{res} to different types of binding sites according to the following rationale (Table 1, Supplementary Tables S1 and S2): (i) The difference between D_{free} and D_{eff} indicated the presence of a protein pool, which binds transiently with $\tau_{res} \leq 0.5$ s. These represent the lowest affinity binding sites (class I) in our analysis. (ii) Kinetic on- and off-rates determined from the reaction-diffusion fit were used to characterize two additional types of binding sites, class II and class III, with $1/k_{off} = \tau_{res}$ in the range of 3–5 s (class II) and 25–100 s (class III). (iii) The highest affinity class IV binding sites comprised the protein fraction that was immobile during the measurement corresponding to a lower limit of τ_{res} of approximately 4 min.

Accordingly, we interpret transient interactions (class I) as unspecific chromatin binding interactions. These were present both in PCH and euchromatin and comprised essentially the entire protein pool of the H3K9me3 demethylases JMJD2B/C and the transcription factor PAX3 (Supplementary Table S2, Supplementary Fig S4A and B). Class II and class III binding sites were present in both euchromatin and PCH for the other proteins, albeit at different concentrations. With respect to the immobile protein fractions (class IV), we measured a particularly strong enrichment for MECP2 (~80-fold), SUV39H1 (~50-fold), and SUV39H2 (16-fold) in PCH as compared to euchromatin (Fig 1C). Immobile fractions of MBD1, SUV4-20H, and HP1 were about 8-fold enriched in PCH. When calculating the immobile fractions in terms of the absolute protein concentrations, the immobile fraction of the combined HP1 species was the largest (2.7 µM), followed by that of MECP2 (1.6 µM), SUV39H (1.1 µM), SUV4-20H (0.2 µM), and MBD1 (0.2 µM) (Fig 1D). Thus, the amount of immobilized HP1 provides enough protein molecules for interactions with MECP2/MBD1, SUV39H, and SUV4-20H at the high-affinity binding sites, although this HP1 fraction represents only approximately 7% of the total HP1 pool. Accordingly, we conclude that 1–3 µM of MECP2, SUV39H, HP1, and SUV4-20H are tightly bound ($k_{off} < 0.005$ s^{-1}) at PCH-specific sites that are mostly absent in euchromatin.

PCH proteins form a complex interaction network

Our finding that MECP2/MBD1, HP1, and SUV39H are present at similar concentrations of about 1–3 µM in a stably PCH-attached
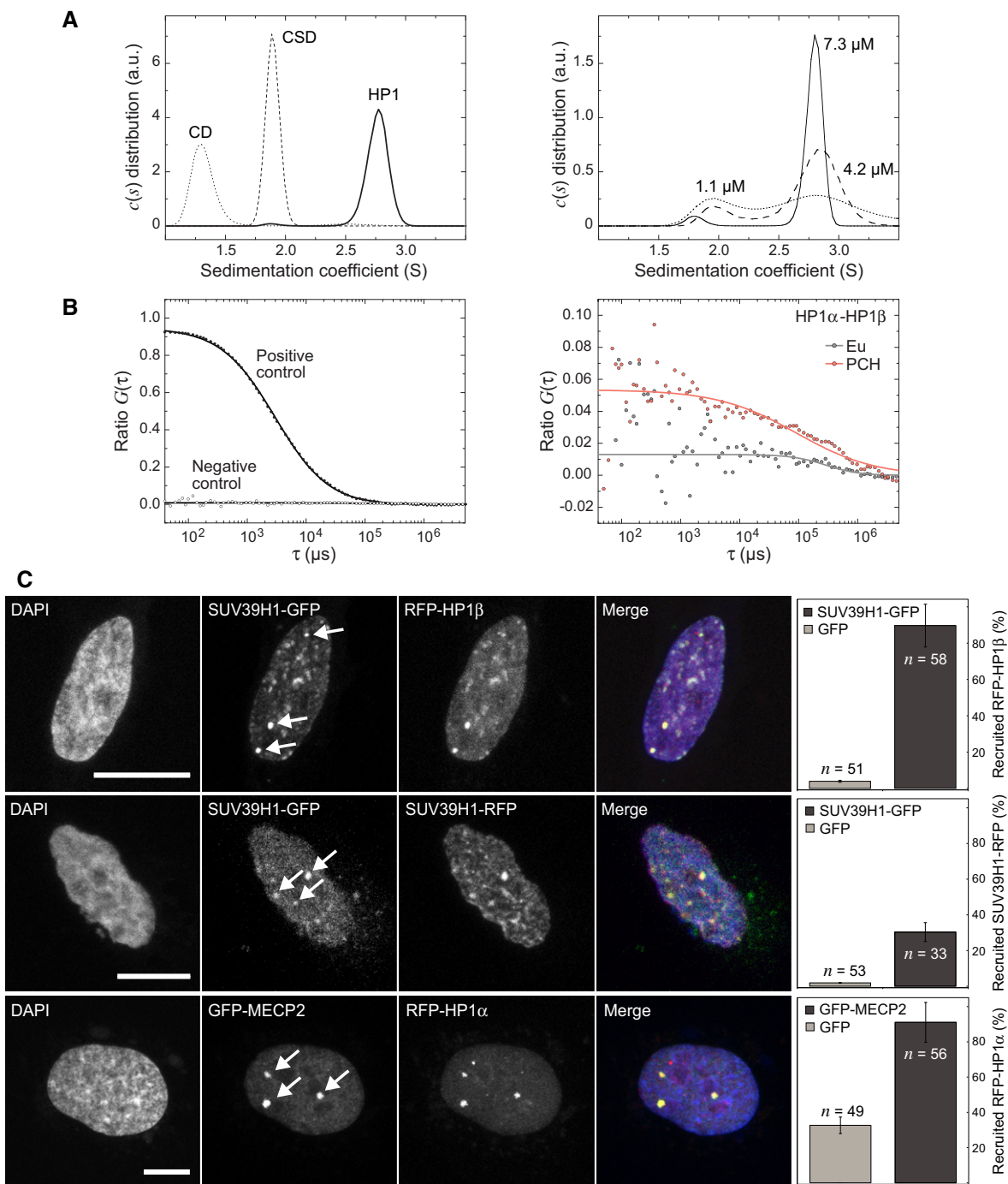
Figure 2. Protein–protein interaction analysis of HP1 and SUV39H1.

A Analytical ultracentrifugation (AUC) experiments of HP1β and its isolated domains. The sedimentation coefficient $c(s)$ distribution obtained from AUC sedimentation velocity runs in the concentration range from 8–30 μM showed dimerization of HP1β and the CSD (left panel) (Supplementary Table S3). Larger complexes were not observed. HP1β dimers dissociated at lower concentrations, which is reflected by two peaks in the $c(s)$ distribution (right panel). An equilibrium dissociation constant of 1–2 μM was determined from the relative molar fractions of monomer and dimer species.

B Protein–protein interaction analysis of soluble nucleoplasmic complexes by FCCS in transiently transfected NIH-3T3 cells. The parameter *ratio $G(\tau)$* reflects the amount of complexes containing GFP- and RFP-labeled proteins. Control measurements were conducted with double-labeled beads in buffer (positive control) and with inert GFP and RFP transiently expressed in NIH-3T3 cells (negative control). For HP1, homodimers and heterodimers were found. Additional FCCS measurements for HP1 and SUV39H1 are shown in Supplementary Fig S5A.

C F2H interaction analysis of SUV39H1 and other PCH proteins. Human U2OS cells were co-transfected with GBP-LacI and the indicated GFP and RFP constructs, resulting in tethering of the GFP-tagged protein to the three lac-operator integration sites. HP1β interacted with SUV39H1 in living cells with the percentage of colocalizations displayed in the barplot. Self-association of SUV39H1 and HP1α recruitment by MECP2 was also demonstrated. Isolated GFP was used as a negative control. Scale bars, 10 μm. Error bars correspond to SD. Further F2H interaction measurements are shown in Supplementary Fig S5B.

Table 1. Summary of binding interactions within the nucleus

	C_{Eu} (µM)	C_{PCH} (µM)	C_{Cyto} (µM)	Binding classes	Binding Eu class, fract. (µM)	Binding PCH class, fract. (µM)	Class I[e] τ_{res}	Class II τ_{res}	Class III τ_{res}	Class IV[f] τ_{res}
MECP2	1.22[a]	8.72[a]	0.15[a]	3	class I: 75% (0.9) class III[c]: 25% (0.3)	class I: 17% (1.5) class III: 65% (5.7) class IV: 18% (1.6)	≤ 0.5 s	–	25 s	~4 min
HP1α	0.5	1.0	0.06	3	class I: 40% (0.2) class II[e]: 60% (0.3)	class I: 24% (0.24) class II: 70% (0.70) class IV: 6% (0.06)	≤ 0.5 s	3 s	–	~4 min
HP1β	3.7	11.2	0.14	3	class I: 40% (1.5) class II[d]: 60% (2.2)	class I: 19% (2.1) class II: 73% (8.2) class IV: 8% (0.9)				
HP1γ	14.7	28.6	0.27	3	class I: 99% (14.5) class II[d]: 1% (0.15)	class I: 20% (5.7) class II: 74% (21.2) class IV: 6% (1.7)				
SUV39H1	0.42	3.0	0.053	4	class I: 32% (0.13) class II: 65% (0.27) class IV: 3% (0.01)	class I: 18% (0.54) class II: 33% (0.99) class III: 29% (0.87) class IV: 20% (0.60)	≤ 0.5 s	5 s	29 s	~4 min
SUV39H2	0.12[a]	0.88[a]	0.016[a]	2	class I: 24% (0.03) class IV: 76% (0.09)	class I: 9% (0.08) class IV: 91% (0.8)	≤ 0.5 s	–	–	~4 min
SUV4-20H1	0.07[b]	0.20[b]	0.026[b]	3	class I: 85% (0.06) class IV: 15% (0.01)	class I: 15% (0.03) class III: 55% (0.11) class IV: 30% (0.06)	≤ 0.5 s	–	25 s	~4 min
SUV4-20H2	0.08[b]	0.20[b]	0.026[b]	3	class I: 83% (0.066) class IV: 17% (0.014)	class I: 8% (0.016) class III: 33% (0.066) class IV: 59% (0.118)	≤ 0.5 s	–	100 s	~4 min
JMJD2C	n.d.	n.d.	n.d.	1	class I	class I	≤ 0.5 s	–	–	–

Endogenous protein concentrations are given in terms of monomers. Values were determined from FCS measurements of GFP-tagged proteins (Supplementary Table S1) and APD-imaging (Supplementary Materials and Methods). The ratio of endogenous to exogenous protein concentrations in the cytoplasm (Cyto), euchromatin (Eu), and heterochromatin (PCH) was determined by quantitative Western blot analysis. The minimal number of binding classes was determined from FRAP measurements and subsequent data fitting to either a diffusion or a reaction-diffusion model. From the fit, fractions of each binding class were determined and residence times were calculated according to $\tau_{res} = 1/k_{off}$.

[a]Values for endogenous SUV39H2 and MECP2 concentrations were determined from RNA expression levels measured in iMEF cells relative to SUV39H1 levels.
[b]For SUV4-20H, concentrations were measured in embryonic stem cells and represent also values in fibroblasts since concentrations do not change significantly during differentiation (Efroni *et al*, 2008).
[c]Class III binding of MECP2 in euchromatin was estimated by refitting the FRAP curves with a reaction-diffusion model.
[d]Class II binding of HP1 was estimated by refitting the FRAP curves with a reaction-diffusion model including a fixed off-rate, which has been determined for heterochromatin.
[e]For unspecific binding of class I, the residence time $\tau_{res} \leq 0.5$ s is given as an estimate of the upper boundary resulting from the time resolution of the FRAP measurements (not extractable from data fitting).
[f]The immobile fraction (class IV) is measured from the plateau value of the FRAP curve after measurements for 4–5 min. It gives the lower boundary of the proteins' residence time for which an approximate value of 4 min was used in the network model.

state (Fig 1D; Table 1) suggests that they assemble into a complex. Accordingly, we mapped their protein interactions *in vitro* and in living cells (Fig 2, Supplementary Fig S5, Supplementary Tables S3 and S4): First, we used analytical ultracentrifugation (AUC) to measure the association state of full-length HP1β and its isolated CD and CSD at physiological ionic strength. Full-length HP1β formed a dimer with an equilibrium dissociation constant of 1–2 µM (Fig 2A, Supplementary Table S3). No larger complexes were detectable up to a concentration of 30 µM. Dimerization was mediated by the CSD of HP1 since the isolated domain was found to be dimeric while the CD was monomeric in agreement with previous results (Ball *et al*, 1997; Nielsen *et al*, 2001). Second, HP1 association in living cells was studied by fluorescence cross correlation spectroscopy (FCCS) after transfecting cells stably expressing GFP-HP1α with RFP-HP1α, β or γ. A soluble nuclear HP1 fraction of 65 ± 34% formed a dimer with either the same HP1 isoform (homodimer) or another isoform

(heterodimer) (Fig 2B, Supplementary Fig S5A). Self-association of SUV39H1 was shown with a corresponding approach, yielding an approximately 24% fraction of soluble SUV39H1 present in homo-dimeric complexes (Supplementary Fig S5A). Third, we applied the fluorescent two-hybrid (F2H) method (Zolghadr *et al*, 2008; Chung *et al*, 2011) to evaluate the SUV39H1-SUV39H1 self-association and interactions of HP1-dimers with stably chromatin-bound SUV39H in living cells. Tethering of SUV39H1-GFP to the *lac*O arrays resulted in the recruitment of RFP-HP1 and SUV39H1-RFP (Fig 2C, Supplementary Fig S5B). Furthermore, a strong interaction of HP1 with MECP2 and MBD1 was observed. However, we could not confirm association of SUV39H1 with the MBD-proteins that was reported elsewhere (Supplementary Fig S5B) (Lunyak *et al*, 2002; Fujita *et al*, 2003; Fuks *et al*, 2003; Esteve *et al*, 2006). A summary of all (direct or indirect) protein–protein associations for the factors studied here is given in Supplementary Table S4. It reveals that the

proteins involved in DNA and histone methylation form a complex interaction network in living fibroblasts. We conclude that several of the above described protein–protein interactions cooperate to target SUV39H to PCH and provide the interaction energy for its stable tethering.

SUV4-20H operates downstream of SUV39H and stabilizes HP1 binding to PCH

SUV39H is required for the enrichment of H3K9me3, H4K20me3, SUV4-20H, and HP1 in PCH, and the loss of H3K9me3 and SUV39H leads to a strong increase in mobility of HP1 in PCH (Supplementary Figs S2B and S4C, Supplementary Table S5) as reported previously (Peters *et al*, 2001; Schotta *et al*, 2004; Müller *et al*, 2009). Immunostaining of 5meC revealed that this mark was maintained in iMEF *Suv39h* dn cells, and also the MBD-proteins MECP2 [as shown previously in (Brero *et al*, 2005)] and MBD1 remained enriched in PCH (Supplementary Fig S2B). This confirms that DNA methylation and enrichment of its reader proteins do not rely on SUV39H (Lehnertz *et al*, 2003; Brero *et al*, 2005).

To assess the influence of H4K20me3 on PCH, we analyzed heterochromatin proteins and histone modifications in iMEF *Suv4-20h* dn cells that lack both H4K20-specific methylases SUV4-20H1 and SUV4-20H2 (Supplementary Fig S2C) (Schotta *et al*, 2008). As expected, the H3K9me3 mark was unperturbed, and SUV39H as well as HP1 were still enriched at the chromocenters (Supplementary Fig S2C, Supplementary Table S5) (Schotta *et al*, 2004). However, FRAP analyses revealed that HP1 was more mobile in *Suv4-20h* dn cells as compared to wild-type cells (Supplementary Table S2). In particular, the immobile HP1 fraction was decreased to about half the wild-type value (Supplementary Fig S4D), the residence time of the bound fraction was shorter, and the effective diffusion coefficient increased. This suggests that SUV4-20H can enhance chromatin binding of HP1 although its binding to PCH occurs downstream of H3K9me3, SUV39H, and HP1.

HP1 stabilizes SUV39H1 binding at PCH and promotes H3K9 trimethylation

We knocked down all three HP1 isoforms with siRNAs to evaluate the effect of HP1 on SUV39H binding and H3K9me3 levels in chromocenters versus euchromatin on the single-cell level. The knock-down resulted in a wide range of HP1 expression levels in individual cells (determined by immunostaining) that correlated with SUV39H1 and H3K9me3 intensity signals (Fig 3A). Global nuclear expression levels of stably integrated SUV39H1-GFP followed that of HP1, suggesting that HP1 stabilizes the *Suv39h1* transcript or protein. In addition, the PCH enrichment of SUV39H1 was reduced at lower HP1 concentrations. While SUV39H1 expression levels and PCH enrichment were sensitive to HP1 abundance over the complete range of knockdown concentrations, the H3K9me3 levels remained constant for HP1 levels above 80% of the wild-type concentration. Thus, cells were able to compensate for variations of HP1 and SUV39H1 concentrations to some extent. Below 80% of HP1, the heterochromatic H3K9me3 levels decayed gradually with decreasing HP1

expression until euchromatic levels were reached (Fig 3A and B). Thus, HP1 contributes to the enrichment of SUV39H1 in PCH and is required for maintaining wild-type H3K9me3 levels. Euchromatic H3K9me3 levels decreased slightly with reduced HP1 concentrations (Fig 3A). This could be related to interactions of HP1 with the histone methylases G9A and SETDB1 that are preferentially active in euchromatin (Tachibana *et al*, 2002; Chin *et al*, 2007; Loyola *et al*, 2009).

SUV39H is responsible for depositing H3K9me3 preferentially in PCH

To quantify the contribution of SUV39H in catalyzing H3K9 trimethylation, we determined the H3K9me3 levels of euchromatin and PCH in wild-type and *Suv39h* dn iMEFs based on the relative H3K9me3 immunofluorescence signal in the same sample preparation (Fig 3C, Supplementary Fig S2B). In wild-type cells, an average H3K9me3 level of $38 \pm 3\%$ in PCH and $28 \pm 1\%$ in euchromatin was calculated based on a total H3K9me3 level of 28% reported previously for mouse fibroblasts (Fodor *et al*, 2006). The corresponding values in the *Suv39h* dn cells were $13 \pm 2\%$ (PCH) and $25 \pm 4\%$ (euchromatin), from which the relative methylation rate of SUV39H can be estimated according to a simple quantitative model: Nucleosomes can carry H3K9me3 (M) or lack this modification (U) (Fig 3D, Supplementary Materials and Methods). Since the JMJD2B/C demethylases were homogeneously distributed in the nucleus and displayed similar mobility in both euchromatin and PCH (Supplementary Fig S4A), the demethylation rate k_{-m} is assumed to be equal in both chromatin states. The resulting H3K9me3 level in each state is solely determined by the ratio of methylation rate k_m to k_{-m}. This yields an 8-fold preference of SUV39H for methylation of PCH versus euchromatin, while the euchromatin-specific methylation provided by other methylases like SETDB1 and G9A is roughly 2-fold higher in euchromatin than in PCH (Fig 3D). Notably, the SUV39H specificity for PCH correlates well with the enrichment of chromatin-bound SUV39H molecules in PCH (16- to 50-fold, Fig 1C). Thus, we conclude that the SUV39H-dependent H3K9me3 modification is directly related to the amount of chromatin-bound enzyme.

Silenced major satellite repeats are enriched with SUV39H, H3K9me3, HP1, and 5meC

To corroborate that SUV39H binding to chromatin concurs with HP1 and H3K9me3 at sites of DNA methylation, we conducted an analysis by ChIP-seq (chromatin immunoprecipitation followed by DNA sequencing). The enrichment of HP1β, SUV39H1, SUV39H2, and H3K9me3 at major satellite repeats was evaluated in neural progenitor cells (NPCs) using the H3K36me3 modification as a reference signature for transcriptionally active chromatin. NPCs were generated *in vitro* from ESCs and represent a well-established model system for studying epigenetic modifications and chromatin composition established during differentiation (Teif *et al*, 2012; Lorthongpanich *et al*, 2013). SUV39H1, SUV39H2, H3K9me3, and HP1β were enriched at the canonical major satellite repeat sequence while no enrichment was detected for H3K36me3 (Fig 4A and B). Furthermore, we analyzed the distribution of bound
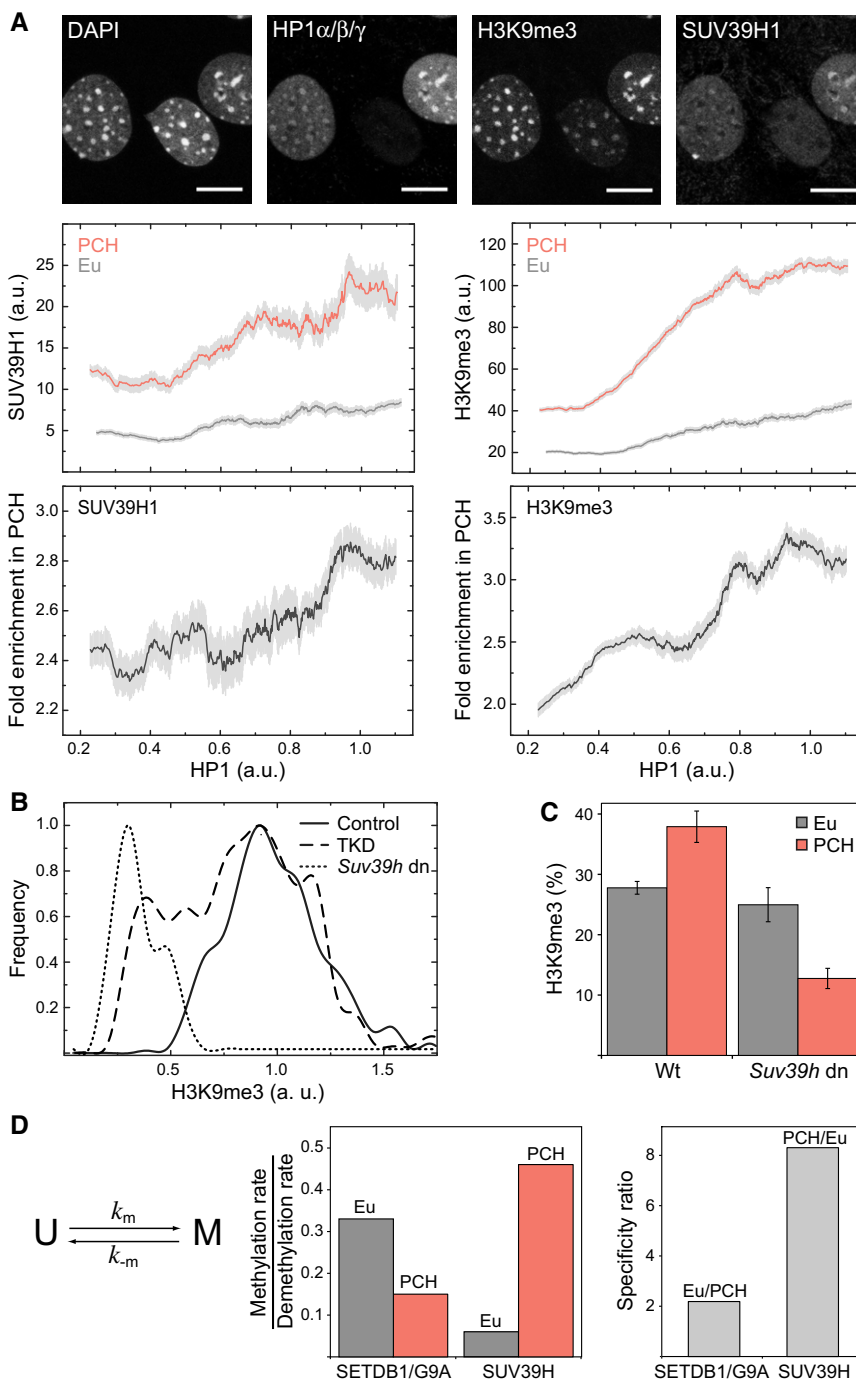
Figure 3. Effect of perturbation of HP1 and SUV39H protein expression.

A   Triple knockdown of HP1α/β/γ by siRNA in NIH-3T3 cells stably expressing SUV39H1-GFP. As apparent from HP1 immunostaining (top) knockdown efficiencies varied largely between individual cells so that a large range of endogenous HP1 concentration was covered. The effects on the abundance of SUV39H1-GFP and the H3K9me3 mark were detected by immunostaining (upper plot panels). Their fold enrichment within PCH is presented in the bottom panels. Light gray bars depict SEM.

B   Frequency distribution of methylation levels per PCH focus in wild-type (wt) cells (control, solid line), *Suv39h* dn cells (*Suv39h* dn, dotted line), and HP1 triple-knockdown cells (TKD, dashed line) transfected with HP1 siRNA.

C   Comparison of H3K9me3 levels in wild-type and *Suv39h* dn cells determined from quantitative imaging after immunostaining. H3K9me3 in PCH was largely reduced in *Suv39h* dn cells while euchromatic levels were unperturbed (see also Supplementary Fig S2B). Absolute H3K9me3 levels were calculated based on the global cellular H3K9me3 level reported previously (Waterston *et al*, 2002; Fodor *et al*, 2006). Error bars correspond to SEM.

D   Average methylation rates were determined based on a simple model assuming an unmethylated and a methylated state for each nucleosome. From the steady-state levels of H3K9me3 in wild-type and *Suv39h* dn cells, the relative rate constants for the transitions are derived. SUV39H methylates PCH with a specificity ratio of 8, whereas SETDB1/G9A methylate preferentially euchromatic regions but with a lower specificity ranging from 1.5–2.2.

proteins at 16 uniquely mappable intergenic/intronic major satellite repeats annotated by the RepeatMasker tool (Fig 4C and D). Of these repeats, 12 were enriched for SUV39H, H3K9me3, and HP1β while H3K36me3 was depleted. Another two repeats resided in an inactive state with low H3K36me3 and higher H3K9me3 levels but lacked enrichment of SUV39H or HP1β. In contrast, the two active repeats carrying H3K36me3 lacked SUV39H, H3K9me3, and HP1β. Thus, the ChIP-seq analysis corroborates our conclusions that stable chromatin binding of SUV39H and transcriptional repression

of major repeats correlate with the presence of HP1 and H3K9me3. Based on the 5meC distribution reported elsewhere (Lorthongpanich *et al*, 2013), we calculated CpG methylation levels of $88 \pm 8\%$ at the 12 inactive intergenic/intronic repeats loaded with SUV39H, H3K9me3, and HP1. The two active repeats had similar CpG densities and similar CpG methylation levels of $86 \pm 2\%$. Since the normalized 5meC density was only slightly higher at 1.3 ± 0.1-fold for silenced repeats compared to transcribed ones, we conclude that 5meC is not the dominant silencing factor for these repeats.
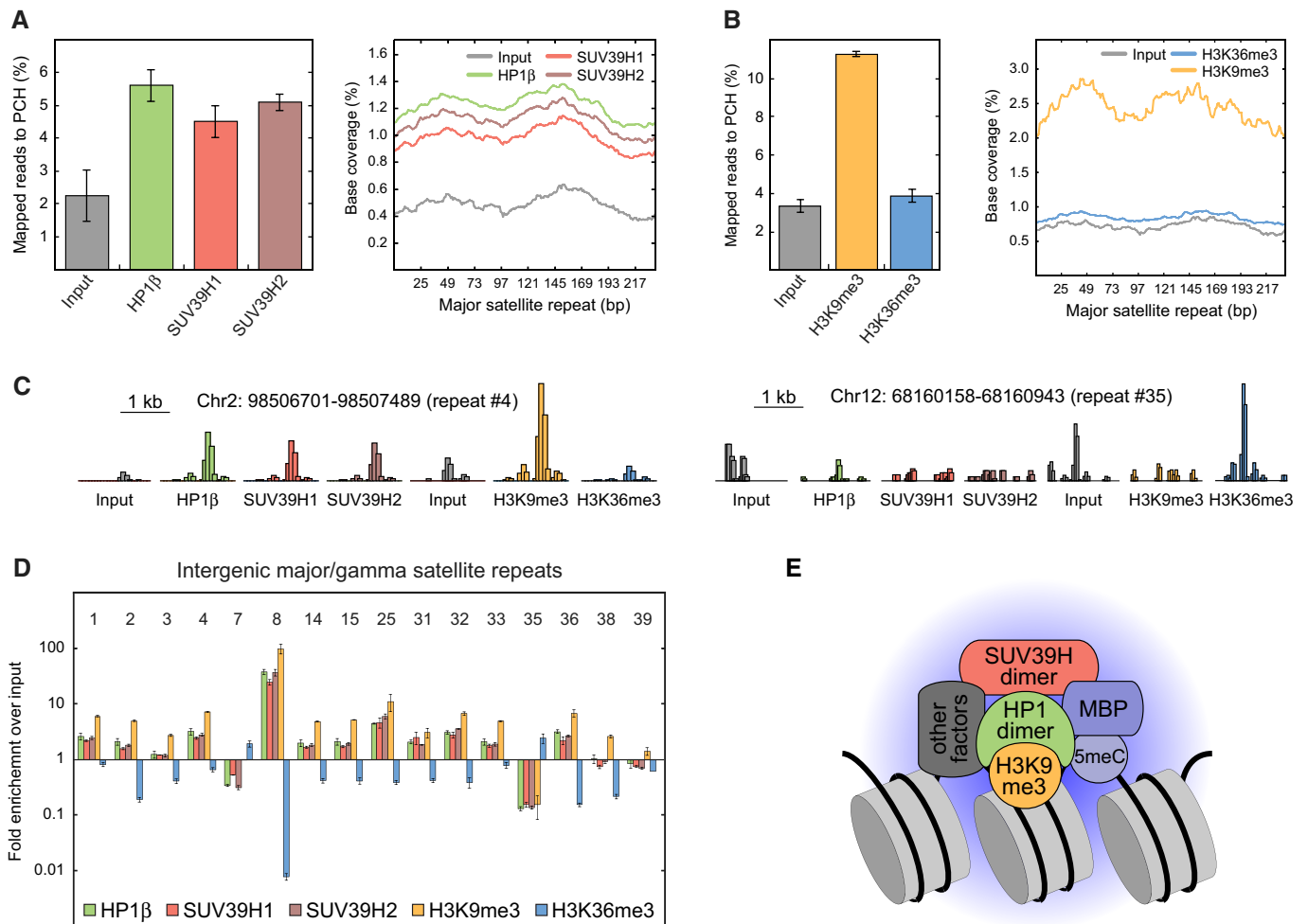

Figure 4. Genome-wide ChIP-seq analysis of HP1, SUV39H, and H3K9me3 enrichment at major satellite repeats.

A   Fraction of total sequencing reads that mapped to the consensus sequence of major satellite repeats (gamma satellites, GSAT) after ChIP-seq of HP1β, SUV39H1, or SUV39H2. Mild sonication conditions were applied in neural progenitor cells (NPCs). The histogram shows the distribution of the mapped reads along the consensus sequence. Error bars correspond to SD.

B   Same as panel A but for ChIP-seq of H3K9me3 and H3K36me3 and with stronger sonication conditions.

C   Representative sequencing read distributions at interspersed major satellites that can be uniquely identified in the genome. Two repeats located on chromosomes 2 and 12 (no. 4 and no. 35 in panel D) are depicted. HP1 and SUV39H were enriched at the transcriptionally inactive repeat (no. 4) that additionally had a high level of the repressive H3K9me3 mark and a low level of the activating H3K36 trimethylation. At the actively transcribed repeat (no. 35) marked by H3K36me3, binding of SUV39H and HP1 was at background levels. The height of the histogram is normalized to total reads.

D   Enrichment of all mapped sequencing reads to interspersed GSAT regions over input control. The 16 regions that can be uniquely mapped are shown. Error bars correspond to SD.

E   Composition of the HP1-SUV39H nucleation complex as inferred from the enrichment of stably bound protein in PCH, protein–protein interaction measurements and ChIP-seq analysis. The postulated complex comprises a HP1 dimer binding H3K9me3-modified nucleosomes and interacting with a SUV39H dimer. Binding of SUV39H is further stabilized by methyl-binding proteins (MBPs) that recognize 5meC and possibly by other interacting factors.

SUV39H methylases remain attached to chromatin during mitosis

Many proteins remain attached to PCH during mitosis (Lewis *et al*, 1992; Fujita *et al*, 1999; Bachman *et al*, 2001; Craig *et al*, 2003; Hayakawa *et al*, 2003; Easwaran *et al*, 2004; Kourmouli *et al*, 2004; Mateescu *et al*, 2004; Brero *et al*, 2005; Fischle *et al*, 2005; Hirota *et al*, 2005; McManus *et al*, 2006; Schermelleh *et al*, 2007; Hahn *et al*, 2013). Thus, the PCH state might be transmitted through cell division by stably bound bookmarking factors. Since SUV39H1 also remains bound to chromosomes in metaphase (Melcher *et al*, 2000), we analyzed its localization in all mitotic phases (Fig 5A). Notably, SUV39H1 remained attached to chromatin through mitosis. From FRAP experiments on mitotic cells, we found $5 \pm 3\%$ of SUV39H1 stably bound to chromatin (Fig 5B, Supplementary Table S6). Since euchromatin and PCH cannot be distinguished on mitotic chromosomes, this should be compared to the weighted average of bound SUV39H1 in PCH and euchromatin of interphase cells ($4 \pm 1\%$). Thus, most SUV39H remained stably bound, suggesting that it serves a bookmarking function for PCH.

The cell cycle-dependent chromatin interactions of HP1 and SUV39H1 were further analyzed by FRAP (Supplementary Table S6). Co-transfection of RFP-tagged proliferating cell nuclear antigen (PCNA) served as a marker for G1 and S phase and delocalized HP1 as an indicator for G2 phase. SUV39H1 showed relatively similar chromatin interaction throughout interphase (Supplementary Fig S1C, Supplementary Table S6). All HP1 isoforms had comparable cell cycle-dependent mobility, and HP1α is shown as an example (Supplementary Table S6). While HP1 exhibited considerable chromatin binding in G1 and S phase consistent with previous findings (Cheutin *et al*, 2003; Festenstein *et al*, 2003; Schmiedeberg *et al*, 2004; Dialynas *et al*, 2007), HP1 mobility could best be described by a diffusion model for both euchromatin and PCH in G2, indicating significantly reduced chromatin interactions. The immobile fraction in PCH was reduced to euchromatin values of $3 \pm 2\%$. The remaining fraction of approximately 3% stably tethered HP1 corresponds to a concentration of 1.2 μM, which is similar to the amount of immobile SUV39H and SUV4-20H in PCH. In summary, our combined imaging- and FRAP-based analyses provide evidence that a considerable fraction of SUV39H remains stably bound to chromatin throughout the cell cycle including all phases of mitosis. Likewise, H3K9me3, HP1, 5meC, MECP2, and MBD1 remained available to enhance SUV39H chromatin interactions. This is consistent with an inheritance mechanism in which the PCH state is transmitted via chromatin-bound bookmarking factors.

Stable SUV39H-containing complexes in PCH arise from multiple protein–protein interactions

Our protein–chromatin and protein–protein interaction data can be rationalized with a model in which SUV39H and HP1 can bind either separately to weaker affinity binding sites with ΔG_{SUV39H} and ΔG_{HP1}, respectively, or to high-affinity sites where both proteins interact with chromatin and are additionally linked by protein–protein interactions. This interaction could be further stabilized by MECP2 or MBD1, which themselves display high-affinity PCH binding, or by other additional factors. The binding free energy $\Delta G_{HP1\text{-}SUV39H}$ of an HP1-SUV39H complex to these high-affinity sites can be approximated as $\Delta G_{HP1} + \Delta G_{SUV39H}$. Based on our FRAP data

(Supplementary Table S2), dissociation constants and residence times for the individual binding reactions to H3K9 trimethylated nucleosomes are $K_d = 19$ μM and $\tau_{res} = 3$ s for HP1, and $K_d = 4$ μM and $\tau_{res} = 13$ s for SUV39H1. Together, these contributions lead to a highly stable chromatin-bound HP1-SUV39H complex with $K_d \approx 0.07$ nM and a corresponding residence time of several minutes, which is consistent with the immobile fraction in our FRAP experiments. Based on the limiting concentration measured for immobilized SUV39H (Table 1, Supplementary Table S7), this complex can only be sparsely distributed throughout PCH, that is the stoichiometry equals one complex per 170 nucleosomes.

Immobilized SUV39H1 is sufficient to form a *de novo* H3K9me3 domain

The correlation between the highly enriched stably chromatin-bound SUV39H fraction (Fig 1C) and the steady-state H3K9me3 levels (Fig 3C) in PCH prompted us to ask whether these stably bound complexes are responsible for the deposition of H3K9me3 in PCH. To test if immobilized SUV39H1 is sufficient to establish a methylated chromatin domain, GFP-SUV39H1 was tethered to the nuclear lamina via a GFP-binding protein that was fused to Lamin B1 (Rothbauer *et al*, 2008) in living iMEF *Suv39h* dn cells. Subsequently, the localization of H3K9me3 was monitored with an RFP-tagged chromodomain (CD) of HP1 (Fig 6A and B). A quantitative analysis of the averaged H3K9me3 profile across the lamina revealed *de novo* H3K9me3 modifications at the nuclear lamina for wild-type SUV39H1 but not for the inactive SUV39H1-H324L-mutant (Fig 6A and C). Thus, immobilized SUV39H methylates nucleosomes that are brought into spatial proximity. The slightly increased width of the profile at half maximum for H3K9me3 (0.47 ± 0.03 μm) versus that of GFP-SUV39H1 (0.40 ± 0.02 μm) indicated that the newly formed H3K9me3 regions extended for < 0.1 μm into the nuclear interior. Thus, the trimethylation mark did not spread beyond those chromatin loci that could transiently interact with tethered SUV39H1 via chromatin dynamics, although free GFP-SUV39H1 was present in the nucleoplasm as detected by FCS.

We conclude that the endogenous propagation of H3K9me3 in PCH can originate from relatively sparsely distributed immobilized SUV39H complexes that locally extend H3K9me3 to spatially adjacent sites. The underlying molecular spreading mechanism might be chromatin looping that can efficiently promote interactions within limited genomic distances of several kilobases or < 100 nm (Rippe, 2001; Erdel *et al*, 2013).

The dynamics of protein binding and histone modifications in PCH can be integrated into a quantitative network model

Based on our experimental observations and data analysis, we developed a quantitative model for the epigenetic network centered around H3K9me3 in PCH with all parameters compiled in Supplementary Table S7. It is based on stably bound SUV39H complexes that are specifically tethered to PCH via multiple interactions (Fig 4E). These SUV39H complexes represent nucleation sites that mediate confined propagation of H3K9me3 via chromatin looping (Rippe, 2001; Erdel *et al*, 2013) (Fig 7A). In particular, such a mechanism rationalizes the experimental findings on the limited extension of H3K9me3 from
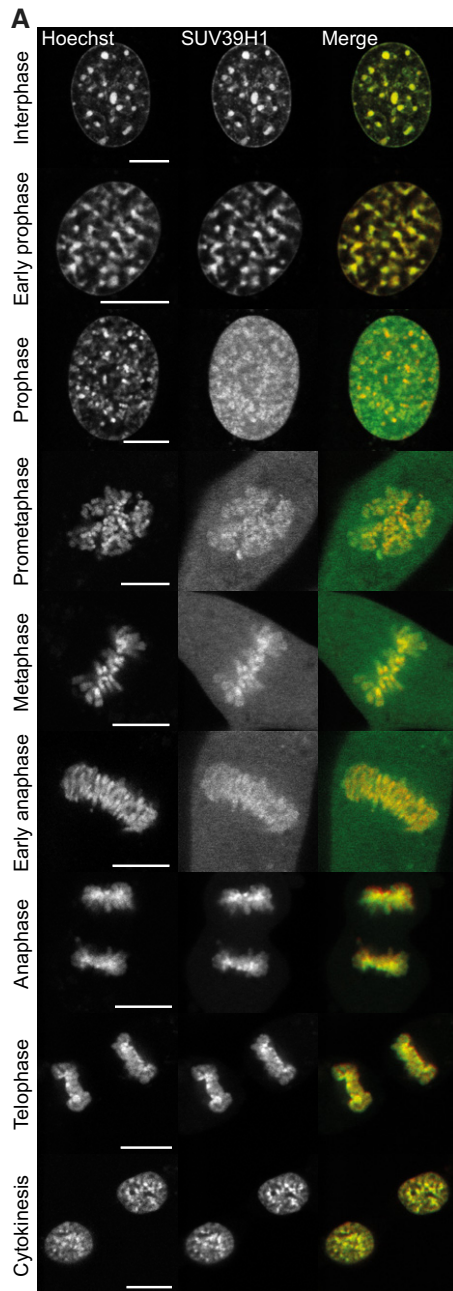
A

B

Figure 5. Chromatin bookmarking by SUV39H1 during the complete cell cycle.

A   Nuclear distribution of SUV39H1-GFP in living cells during different cell cycle phases. SUV39H1-GFP remained stably associated to mitotic chromatin (stained with Hoechst 33342) during all phases of the cell cycle. Scale bars, 10 μm.

B   FRAP measurements of SUV39H1-GFP bound to condensed chromosomes in mitotic cells. Since euchromatin and PCH cannot be distinguished on mitotic chromosomes, the immobilized fraction of $5 \pm 3\%$ was compared to the weighted average of immobile SUV39H1 in PCH and euchromatin in interphase cells (Supplementary Tables S2 and S6). Error bars correspond to SEM.

SUV39H1 bound to the nuclear lamina (Fig 6) as well as the size of histone methylation domains that have been found around chromatin-tethered proteins (Erdel *et al*, 2013).

Our quantitative model focuses on the signature heterochromatin mark H3K9me3 and its interacting proteins, HP1 and SUV39H, in an extended chromatin segment (300 nucleosomes or ~60 kb DNA). Each nucleosome can either reside in the unmodified state "n" or in the H3K9 trimethylated state "m" (Fig 7B). Depending on the presence of HP1 ("H") and SUV39H ("S"), the chromatin-bound complexes "Hm", "Sm", and "SHm" can assemble. The PCH-specific high-affinity binding sites for SUV39H and HP1 are referred to as origins "o", which can either be free, occupied by SUV39H ("So") or HP1 ("Ho") alone, or by the HP1-SUV39H complex ("SHo"). According to our experimental data, every 8th nucleosome in PCH and every 71st nucleosome in euchromatin is an origin (see Supplementary Materials and Methods, Mathematical modeling of PCH network). Based on the experimentally measured immobile SUV39H fractions and concentrations, every 21st origin, that is every 170th nucleosome, is in the *SHo* state at a given point of time. All parameters used in the modeling and their sources are given in Supplementary Table S7.

The model quantitatively accounts for the different experimentally observed types of binding sites for SUV39H1 and HP1 and their occupancy. For the H3K9 trimethylation reaction, we distinguish different pathways. Freely mobile SUV39H at a concentration c_s methylates nucleosomes with a basal rate $k_m \cdot c_s$. H3K9 trimethylation by other histone methylases like G9A/SETDB1 is accounted for as an additional reaction with rate constant k_u in PCH and $k_e + k_u$ in euchromatin. Finally, chromatin-bound SUV39H catalyzes H3K9 trimethylation via chromatin looping. The efficiency for trimethylating H3K9 in a nucleosome at distance b from the SUV39H-bound site corresponds to $k_m \cdot j_M(b)$. Here, $j_M(b)$ is the local concentration of the respective complex in proximity of the target nucleosome (Erdel *et al*, 2013) (Fig 7A). Importantly, we do not assume that chromatin-bound SUV39H is intrinsically more active than free SUV39H but that the decisive factor is the enhanced local concentration of the former.

For our model, the association and dissociation rates and the concentrations of free proteins were taken as determined from the FRAP and FCS experiments (Supplementary Materials and Methods, Supplementary Table S7). To simplify the model, we combined the parameters for SUV39H1 and SUV39H2 weighted according to their concentrations into a unified SUV39H enzyme (Supplementary Table S7). The rate constant for H3K9me3 demethylation was fixed to $k_{-m} = 0.0013$ min^{-1} according to mass spectrometry experiments in HeLa cells (Zee *et al*, 2010). The unspecific methylation rate k_u, the
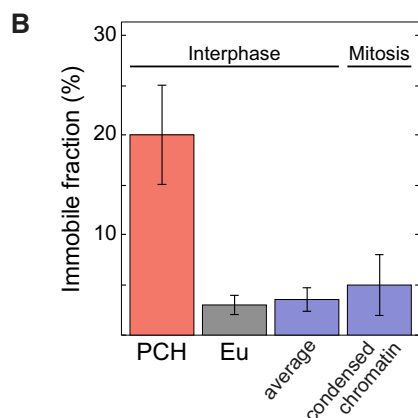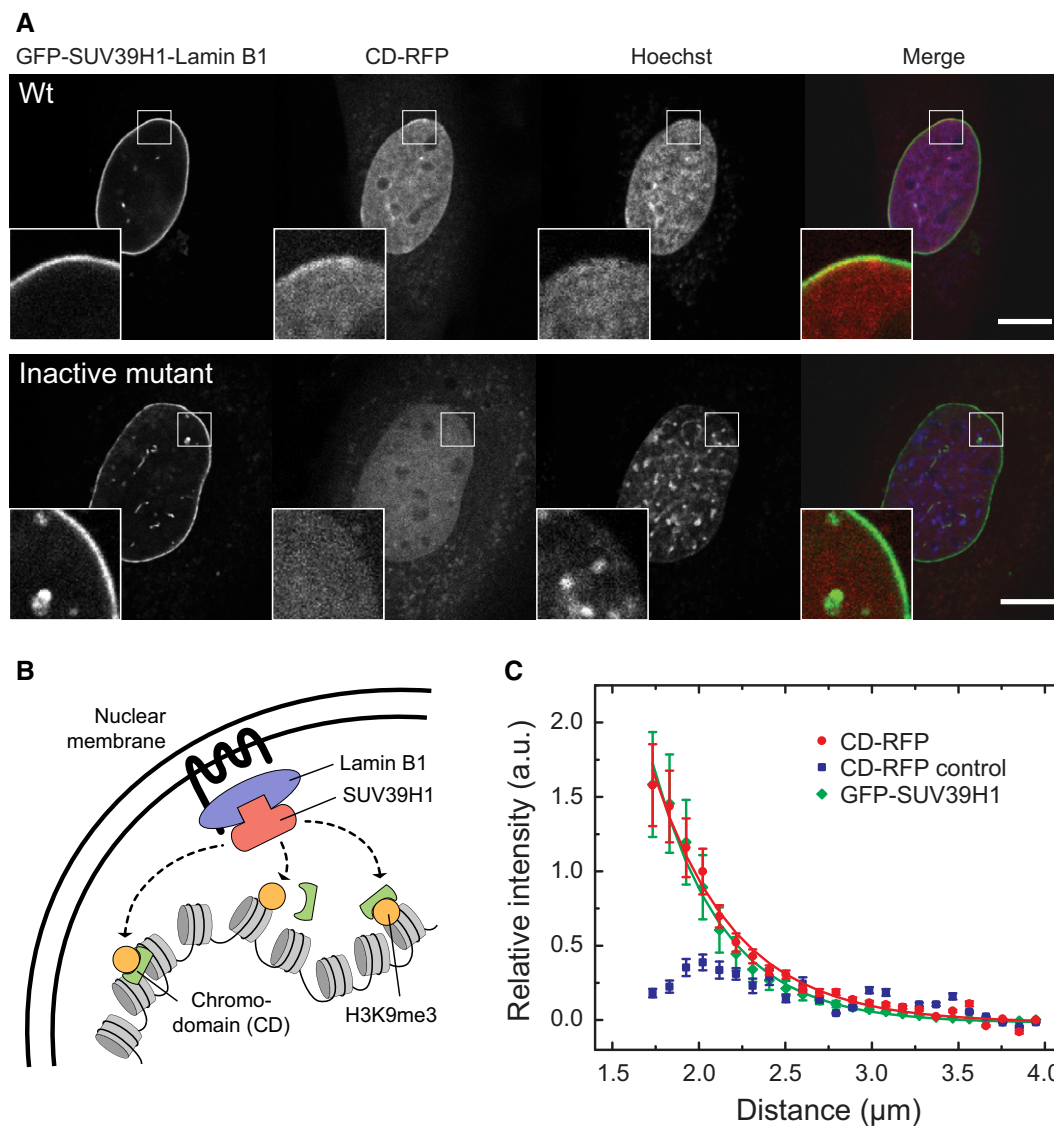
Figure 6.   Propagation of H3K9me3 by stably tethered SUV39H1 to nucleosomes in its spatial proximity.

A   Establishment of H3K9me3 domains by GFP-SUV39H1 recruited to the nuclear lamina via GBP-Lamin B1 in iMEF *Suv39h* dn cells. H3K9me3 was detected via CD-RFP and appeared in a confined region adjacent to the nuclear lamina (see inset). When the inactive mutant SUV39H1-H324L-GFP was recruited, no enrichment of CD-RFP was observed. Scale bar, 10 μm.

B   Cartoon model depicting the experimental setup in panel A.

C   Averaged radial fluorescence intensity profiles from the lamina to the center of the nucleus measured for the experiments described in panel A. The profile of CD-RFP reflects the H3K9me3 levels and was measured in cells transfected with GFP-SUV39H1 (red) or the inactive SUV39H1-H324L-GFP mutant (blue, control). The recruitment of GFP-SUV39H1 (green) resulted in a lamina-confined enrichment with a width of 0.40 ± 0.02 μm as determined by fitting the data to an exponential decay curve. While wild-type SUV39H1 methylated the surrounding chromatin within a confined area of 0.47 ± 0.03 μm width (red), SUV39H1-H324L (blue) did not increase the methylation (blue) in this region. Error bars correspond to SEM.

euchromatin-specific rate k_e, and the SUV39H-dependent methylation rate k_m were fitted to yield the measured steady-state levels of H3K9me3 in PCH (38%) and euchromatin (28%) of wild-type cells (Fig 3C). The system was formulated as a set of deterministic ordinary differential equations (ODEs) to calculate the steady-state probabilities of each nucleosome to be in a particular state for a given set of conditions and, in parallel, simulated stochastically (Fig 7C and D; Supplementary Model Code). The model simulations show that the relatively sparse binding events of SUV39H at the origin sites

are sufficient to account for the increased H3K9me3 levels in PCH compared to euchromatin (Fig 7C and D). At any given nucleosome, the methylation state fluctuates over time (Fig 7D). However, the time average is consistently described by the stochastic and deterministic models and yields the observed enrichment of H3K9me3 in PCH over euchromatin as well as the measured occupancies of HP1 and SUV39H. Thus, we conclude that PCH-specific high-affinity SUV39H/HP1 binding sites can robustly maintain the PCH-specific H3K9me3 levels via a DNA looping mechanism.
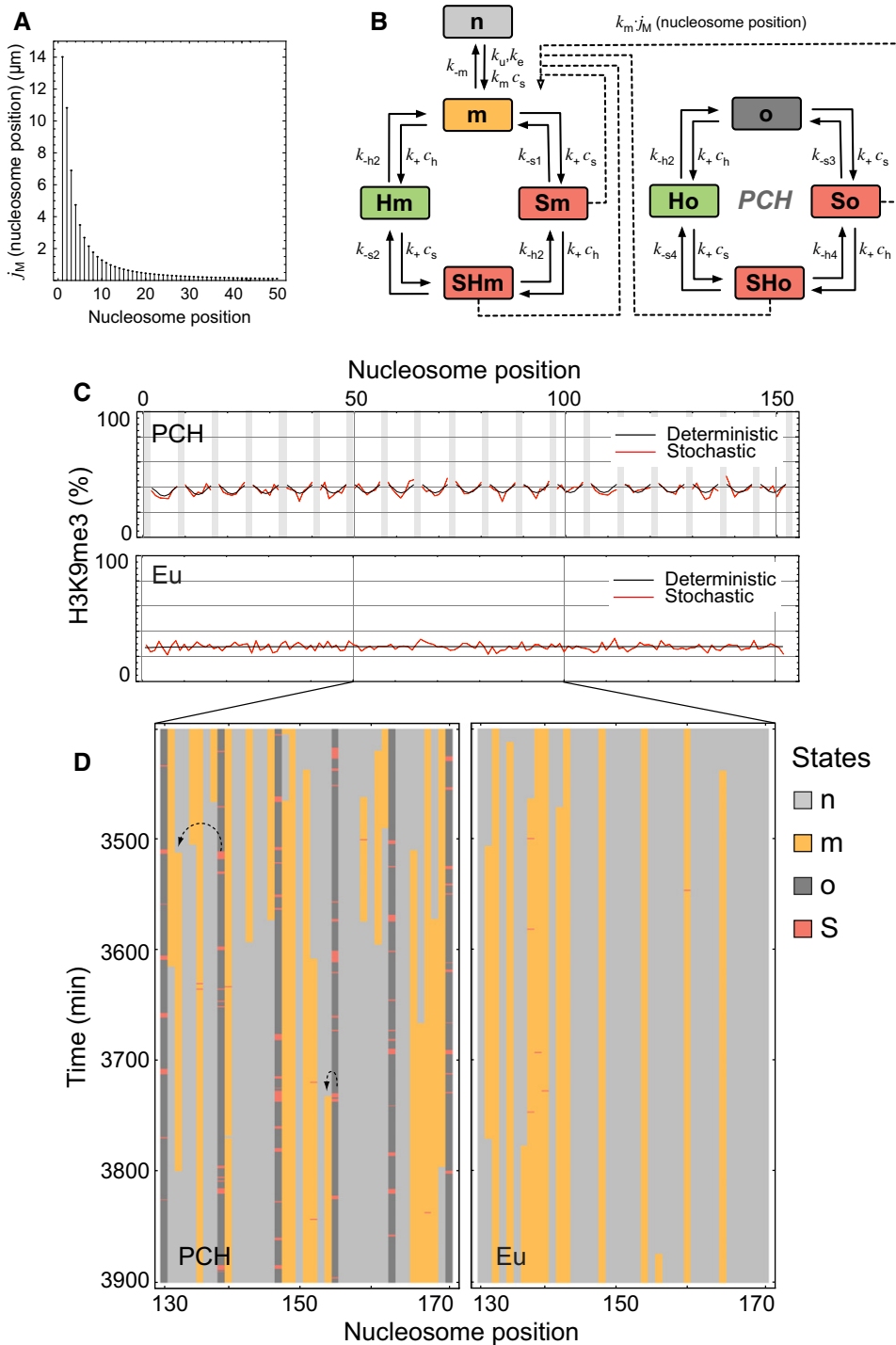
Figure 7. Quantitative model for H3K9 trimethylation in PCH.

A   Probability of interactions between two nucleosomes due to chromatin looping as expressed by their local molar concentration j_M. Based on the data for chromatin interactions during recombination in living cells (Ringrose *et al*, 1999), the dependence of j_M on the separation distance from a SUV39H-bound nucleosome was calculated as described previously (Rippe, 2001; Erdel *et al*, 2013).

B   PCH network model scheme. The model includes transitions between the following states according to the indicated rate constants: "*n*", nucleosome without H3K9me3; "*m*", H3K9me3 modified; "*o*", origin that represents a high-affinity binding site for SUV39H. HP1 and SUV39H bound to these sites are represented by *H* and *S*, respectively, to form the states "*Hm*", "*Sm*", "*SHm*", "*Ho*", "*So*", and "*SHo*". All SUV39H-bound states (red) enhance methylation of adjacent unmodified nucleosomes through chromatin looping. See text and Supplementary Table S7 for further details.

C   Steady-state distribution of methylation levels for a chromatin segment in PCH or euchromatin. The deterministic and stochastic distributions are depicted in black and red, respectively. Stochastic solutions were averaged over 5,000 min. The nucleation origins (both occupied and unoccupied) are marked in gray.

D   Stochastic simulation for a region of 40 nucleosomes. Same color code for nucleosome states and origins as in panel B.

Stochastic simulations reveal that PCH-specific features are robustly maintained for the experimentally determined parameter range

Several experimental and theoretical studies showed that the epigenetic silencing mechanisms can be sensitive to stochastic effects either due to the presence of positive feedback loops in nucleosome modification (Sneppen *et al*, 2008), long-range nucleosomal interactions (Dodd *et al*, 2007), the cooperativity in recruitment of histone modifiers (Sedighi & Sengupta, 2007) or simply due to low protein concentrations. Accordingly, we evaluated our model with respect to the degree of intrinsic noise that can cause stochastic focusing effects by conducting Monte Carlo simulations according to the Gillespie stochastic simulation algorithm. An example for the resulting fluctuations of the states in which individual nucleosomes are present in PCH or in euchromatin is depicted in Fig 7D. Relatively sparse binding events of SUV39H at the "*o*" sites are sufficient to increase H3K9me3 levels compared to euchromatin. For both the PCH and euchromatin state, we simulated 100 individual time traces up to 5,000 min starting from an initially naive non-modified fiber (Fig 7D). The low variability of H3K9me3 in steady state revealed that the level of intrinsic noise in our model is very low when averaged over the entire nucleosome chain, with a standard deviation of approximately 3% from the population-mean for PCH. As expected, the spatial steady-state distribution of H3K9me3 modifications over the entire chain agreed well with the deterministic solutions for all conditions (Fig 7C). Thus, we conclude that the system robustly maintains the PCH-specific H3K9me3 levels.

The cellular response to perturbations of the H3K9me3 state is accurately predicted by the network model

We systematically investigated the predictions of our model with respect to the response of the system to perturbations induced by (i) lowering the HP1 concentration, (ii) increasing the H3K9me3 demethylation activity or (iii) changing the concentration of origin sites. First, we evaluated the distribution of H3K9me3 levels in model simulations for different HP1 concentrations. SUV39H binding and H3K9me3 levels gradually decreased when lowering the HP1 concentrations, consistent with the behavior observed in the HP1 knockdown experiments (Fig 8A and B). Second, we mimicked the increase of H3K9me3 demethylation activity by raising the corresponding parameter k_m. This resulted in a gradual decrease of H3K9me3 in PCH, which contradicts the notion of bistable states. To test this behavior of the system experimentally, we overexpressed JMJD2C, an H3K9me3-specific histone demethylase, to reduce H3K9 trimethylation (Fig 8C). H3K9me3 levels were evaluated in PCH of single cells on fluorescence microscopy images, normalized to the DAPI signal, and correlated with the JMJD2C-GFP expression levels. The relation of demethylation rate and H3K9me3 levels predicted from our model was in good agreement with the experimental data and showed a gradual decrease of H3K9me3 in PCH with increasing demethylation activity (Fig 8C). Third, we evaluated the dependence of H3K9me3 in PCH on the concentration of origin sites (Fig 8D). We found an approximately linear response of the H3K9me3 levels up to the wild-type "*o*" site concentration range of approximately 30 μM.

From simulations of the kinetics of methyl mark propagation in virtual H3K9me3 induction experiments, we conclude that all transient perturbations on the minute time scale will not affect the overall PCH H3K9me3 levels due to the slow response of the system (Fig 8E). The simulations were started from the completely unmodified PCH state (e.g. all nucleosomes in state "*n*" and "*o*" sites at every 8th nucleosome), and the H3K9me3 level was followed over time. The steady-state PCH level of 38% was reached after approximately 33 h, corresponding to a propagation rate of 0.35 nucleosomes per hour from a given nucleation site. Notably, these kinetics are comparable to the value of 0.18 nucleosomes per hour measured experimentally for H3K9me3 propagation at the *POU5F1* promoter in mouse fibroblasts when inducing H3K9 trimethylation by tethering HP1α (Hathaway *et al*, 2012). One key parameter to modulate H3K9me3 levels in PCH is the SUV39H concentration (Fig 8F), which might vary between cell types. A 2-fold increase or decrease of the wild-type SUV39H concentration as observed between ESCs and MEFs would raise or lower H3K9me3 levels in PCH from an average value of 38% to about 51% or 28%, respectively.

In summary, we found that the predictions made by our model were in very good agreement with experiments. We conclude that it introduces an appropriate representation of the available data reported here and elsewhere that are relevant for the epigenetic network centered on H3K9me3 in mouse fibroblasts. The model quantitatively describes the properties of euchromatin and PCH determined here under different conditions and explains how a cell can robustly maintain the PCH state without the requirement to invoke additional components such as boundary proteins that bind to chromatin and block linear PCH spreading.

Discussion

Here, we present a comprehensive analysis of the epigenetic network that silences the transcription of major satellite repeats in mouse fibroblasts. Based on data from advanced fluorescence microscopy methods and ChIP-seq, we explain how chromatin and protein interactions of MECP2, MBD1, DNMT1, SUV39H1, SUV39H2, JMJD2B/C, HP1α, HP1β, HP1γ, SUV4-20H1, and SUV4-20H2 are linked to 5meC, H3K9me3, and H4K20me3 modifications in PCH. From our quantitative analysis, we derive a predictive mathematical model that provides insight on how the silenced PCH state in fibroblasts is stably maintained and how it could be transmitted through the cell cycle. As mentioned above, H3K9me3 levels and transcriptional silencing in PCH vary between cell types (Supplementary Fig S2). The underlying mechanisms are only partly understood and beyond the scope of the present study. Nevertheless, our modeling framework provides an approach to evaluate the effect of key parameters. For example, differential regulation could rely on changing the composition of the nucleation complex (Fig 8B) or SUV39H abundance (Fig 8F). In addition, it is noted that SUV39H activity itself is controlled by posttranslational modifications like acetylation (Vaquero *et al*, 2007), methylation (Wang *et al*, 2013), or phosphorylation (Park *et al*, 2014), which links it to additional cellular pathways.

Stably bound PCH complexes of SUV39H require the simultaneous presence of DNA methylation, MECP2, H3K9me3, and HP1

To rationalize our results, we propose that a network of interactions between 5meC, MECP2, MBD1, SUV39H, H3K9me3, and HP1 is responsible for the stably PCH-bound SUV39H complexes that are immobile on the time scale of minutes (Fig 4E, Table 1). Additional factors might further stabilize SUV39H as discussed below. Based on our AUC, FCCS, and F2H experiments, we conclude that most HP1 is present as a homo- or heterodimer in the cell and interacts with SUV39H1 that is in a monomer–dimer equilibrium (Fig 2, Supplementary Fig S5). This interaction is needed for stable SUV39H binding and H3K9 trimethylation in PCH as demonstrated in the triple knockdown of all HP1 isoforms (Fig 3A and B). The link between immobilized HP1 and SUV39H as well as the H3K9 trimethylation mark was further corroborated by FRAP measurements of HP1 in *Suv39h* dn cells, where H3K9me3 reduction and the loss of the binding partner SUV39H led to a strong increase in HP1 mobility and the loss of immobile HP1 (Supplementary Fig S4C) (Müller *et al*, 2009).

By quantifying parameters needed for PCH network modeling, our study provides an important extension of previously published FRAP studies of HP1 (Cheutin *et al*, 2003; Festenstein *et al*, 2003; Schmiedeberg *et al*, 2004; Dialynas *et al*, 2007). The concentration of immobilized HP1α/β/γ (1–3 µM, depending on cell cycle phase) and immobile SUV39H (~1.4 µM) in PCH measured here is compatible with an HP1 dimer interacting with a SUV39H dimer. The presence of PCH-bound SUV39H-HP1 complexes is consistent with our ChIP-seq analysis of SUV39H1, SUV39H2, HP1β, and H3K9me3, which were enriched at silenced but not at active intergenic/intronic major satellite repeats (Fig 4). These findings are in very good agreement with previous studies: (i) A SUV39H1 mutant lacking its N-terminal chromodomain (SUV39H1-ΔN89) and thus being unable to interact with HP1 showed a homogeneous distribution throughout the nucleus and strongly reduced chromatin interactions in mammalian cell lines (Krouwels *et al*, 2005). (ii) HP1 dimerization was found to be important for maintaining H3K9me3 in yeast (Haldar *et al*, 2011). (iii) *In vitro* experiments showed that SUV39H1 interacts with HP1 by binding the molecular surface formed by dimerization of the chromoshadow-domain (Aagaard *et al*, 1999; Yamamoto & Sonoda, 2003; Nozawa *et al*, 2010).

Both HP1 and SUV39H1 are able to recognize H3K9me3 (Lachner *et al*, 2001; Jacobs & Khorasanizadeh, 2002; Jacobs *et al*, 2004), and the modification may confer some specificity for PCH binding via local H3K9me3 clusters, since each of the two chromodomains in an HP1 dimer may bind to one H3K9me2/3 residue (Thiru *et al*, 2004). Nevertheless, it is apparent from our quantification that H3K9me3 alone is not sufficient to stably and specifically tether the HP1-SUV39H complex to PCH. While high-affinity SUV39H binding was hardly present in euchromatin and the stably tethered SUV39H pool was enriched approximately 16- to 50-fold in PCH with respect to euchromatin, H3K9me3 levels were only moderately higher in PCH than in euchromatin (~1.4-fold). Rather, our quantitative chromatin interaction analysis suggests that SUV39H is tethered to PCH via interactions with multiple factors including MECP2, MBD1, and HP1 (Figs 1B, C and 2C, Supplementary Fig S5B). Since MECP2 binding is linked to 5meC (Nan *et al*, 1996), 5meC contributes to SUV39H immobilization. Further, H3K9me3 and 5meC are interrelated as

iMEF *Suv39h* dn cells showed reduced DNA methylation at major satellite repeats (Lehnertz *et al*, 2003; Fuks, 2005) although MECP2 and 5meC colocalized with PCH also in the absence of SUV39H (Supplementary Fig S2B). Notably, 5meC enrichment is not sufficient for PCH formation since a subset of intergenic major satellite repeats displays high 5meC levels but was devoid of SUV39H and transcriptionally active (Fig 4C and D). The above conclusions are supported by a number of previous findings: (i) Interactions of SUV39H1 with MECP2 have been demonstrated (Lunyak *et al*, 2002; Fujita *et al*, 2003). (ii) Krouwels *et al* showed that DNA demethylation increases SUV39H1 mobility and reduces the fraction of immobile SUV39H1, whereas HP1 mobility remained unchanged (Krouwels *et al*, 2005). This is compatible with our model since only 1–2% of total HP1 were present in the immobilized HP1-SUV39H complex. (iii) The loss of a DNMT1 complex reduced pericentric H3K9 methylation levels in human HeLa cells (Xin *et al*, 2004). (iv) The knockout of MECP2 in neuronal cells resulted in aberrantly low levels of H3K9me3 in PCH but not in euchromatin (Thatcher & LaSalle, 2006).

We conclude that the stability and specificity of the SUV39H-HP1-MECP2/MBD1 complex in PCH involves protein–protein interactions between these factors and some contribution from an increased 5meC level. Nevertheless, it is likely to be enhanced by additional protein factors. Since the PAX3 and PAX9 transcription factors were not stably bound at PCH (Supplementary Fig S1B and S4B), they are unlikely to play a direct role in stabilizing the HP1-SUV39H nucleation complex. Rather, PAX proteins might regulate the abundance of transcripts in PCH that potentially act as a binding platform for downstream factors (Maison *et al*, 2011). A number of other factors have been linked to PCH. For example, it was shown that the Mi-2/NuRD complex, which contains several interaction partners of SUV39H and HP1, is necessary to maintain the H3K9me3 mark in PCH (Sims & Wade, 2011). The contribution of such additional factors that enhance SUV39H binding in addition to MECP2 and/or MBD1 is implicitly considered in our quantitative model via the use of the experimentally determined enrichment of the SUV39H high-affinity binding sites in PCH that is independent of their exact molecular composition.

Relatively sparse stably bound SUV39H nucleation complexes are sufficient to propagate H3K9me3 via chromatin looping

The stably bound SUV39H-HP1-MECP2/MBD1 complex in PCH was present at a concentration of approximately 1 µM as inferred from the concentrations of its constituting components of 1.4 µM (dimeric HP1 isoforms), 0.7 µM (dimeric SUV39H1 and SUV39H2), 1.4 µM (MECP2), and 0.2 µM (MBD1), while the nucleosome concentration in PCH was approximately 230 µM (Supplementary Table S7). Thus, bound SUV39H is sparsely distributed. We propose that the H3K9me3 modification is propagated via looping of the nucleosome chain to nucleosomes in spatial proximity from these complexes (Figs 6B and 8G). By ectopically tethering SUV39H1 to the nuclear lamina, we demonstrated experimentally that SUV39H immobilization indeed leads to the locally confined enrichment of H3K9me3 (Fig 6). Thus, chromatin-bound SUV39H might interact with substrate nucleosomes on the same chain or from another chromosome in spatial proximity. Our results are fully consistent with the experimental results from the DamID approach developed by van
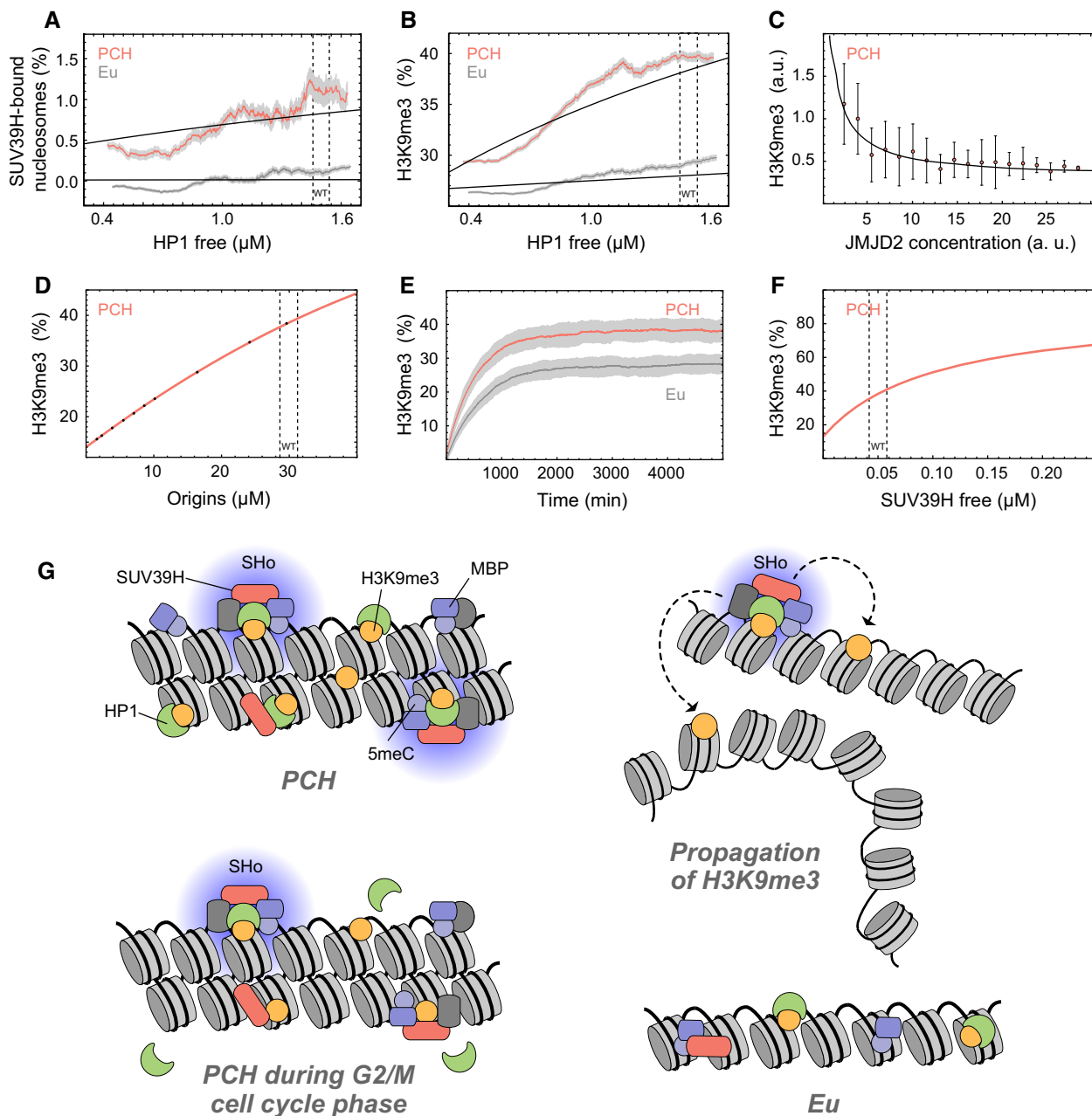
Figure 8. Prediction of PCH features from network model.

A   Dependence of SUV39H enrichment on HP1 concentration in PCH (red) and euchromatin (gray). Model predictions (black lines) were compared to the experimental values determined in the triple-knockdown experiments shown in Fig 3.

B   Same as panel A but for H3K9me3 instead of SUV39H.

C   Dependence of H3K9me3 levels on the concentration of the H3K9me3 demethylase JMJD2C. Error bars correspond to SD. The model prediction (solid line) agreed very well with the experimental data (points) derived from over-expression of JMJD2C-GFP.

D   Predicted average H3K9me3 levels in PCH versus concentration of the origins.

E   Stochastic time evolution of H3K9 trimethylation in PCH and euchromatin from a completely H3K9me3-deficient state. Red and dark gray traces are averages of 100 single stochastic trajectories with the standard deviation shown in light gray.

F   Dependence of H3K9me3 in PCH on SUV39H concentration. This parameter varies between different mouse cell types. For example, in ESCs the combined SUV39H1/2 concentration is 2-fold reduced compared to NIH-3T3 fibroblasts as estimated from their normalized RNA expression levels.

G   "Nucleation and looping" model for the propagation of H3K9me3 in PCH. The high-affinity binding sites with immobilized HP1 and SUV39H represent the SUV39H nucleation complex (Fig 4E; "SHo" in Fig 7B), which is highly specific for PCH. In contrast, the low-affinity binding sites composed of single protein factors were found throughout the whole nucleus, that is in both PCH and euchromatin. While soluble SUV39H proteins can methylate unmodified nucleosomes, the SUV39H nucleation complex provides a high local concentration of the enzyme and is responsible for the majority of catalytically productive collisions in PCH. Due to chromatin looping, the chromatin-bound SUV39H complexes can either methylate adjacent nucleosomes on the same chain or in 3D at other loci that reside in spatial proximity. The persistence of stably chromatin-bound SUV39H throughout the cell cycle (Fig 5) sustains the H3K9me3 modification.

Steensel et al that uses adenine methylation by DNA adenine methyl-transferase (Dam) as readout for interaction. Both the extension of adenine methylation from chromatin-tethered Dam (van Steensel & Henikoff, 2000) as well as the extension of this DNA methylation from Dam tethered to the nuclear lamina (Kind et al, 2013) are in excellent agreement with our mechanism for setting H3K9me3 from SUV39H-bound sites on chromatin or the nuclear lamina.

We would like to emphasize that the propagation of H3K9me3 via the assembly of additional SUV39H-HP1-MECP2/MBD1 nucleation complexes is inherently limited in 3D without the requirement for additional insulator proteins: (i) Only sites that also have pre-existing DNA methylation and bound MECP2/MBD1 in addition to H3K9me3 could lead to nucleation complex assembly. A newly formed H3K9me3 site alone would not be sufficient. (ii) The formation of productive nucleation sites is limited by the available amount of SUV39H. (iii) The H3K9 trimethylation activity originating from the nucleation complexes occurs only within the looping distance of chromatin around these complexes. Typical spreading distances for H3K9me3 limited by the diffusive motion of the chromatin fiber are 5–10 kb, in agreement with other experimental studies discussed elsewhere (Erdel et al, 2013). (iv) There is no preferred direction for diffusive motion of chromatin-bound SUV39H molecules and collisions rather occur in three dimensions with all nucleosomes in spatial proximity that could also be located on a different chromosome. This provides a straightforward explanation for the spherical shape of chromocenters, which may contain pericentromeric repeats from more than one chromosome (Probst & Almouzni, 2008).

SUV39H bookmarks PCH during all cell cycle stages

According to our model, the reestablishment of H3K9me3 in PCH at newly assembled and unmodified histones after replication is mediated by SUV39H that remains bound throughout the cell cycle (Figs 5 and 8G, Supplementary Fig S1C). This process is likely to involve the SUV39H interaction partners MECP2 and MBD1 that show the same persistent binding enhanced by 5meC. This link between H3K9me3 and 5meC is in line with the previous report that the epigenetic inheritance of H3K9me3 involves DNA methylation (Hathaway et al, 2012). Furthermore, a relatively small fraction of HP1 was still immobilized at PCH during G2 phase in the FRAP experiments, which amounts to a significant concentration of approximately 1 μM due to the high level of total HP1. This is consistent with the detection of HP1α/β/γ in a quantitative proteomics analysis of mitotic chromosomes (Ohta et al, 2010), and the presence of HP1α and HP1γ at (peri-)centromeric chromatin on metaphase spreads (Nozawa et al, 2010; Hahn et al, 2013). In addition, SUV39H and HP1 were detected at nascent chromatin following DNA replication (Alabert et al, 2014). Thus, we conclude that the SUV39H nucleation sites persist during all phases of the cell cycle. The constitutive presence of the SUV39H enzymes at PCH together with the finding that SUV39H1 is sufficient to establish de novo H3K9me3 domains when immobilized at the nuclear lamina (Fig 6) has important mechanistic implications: It strongly suggests that the PCH-associated SUV39H molecules are responsible for locally reestablishing the H3K9me3 modification after its dilution during replication (Fig 8G). Thus, immobilized SUV39H molecules might act as bookmarking factors that stably transmit the PCH state through the cell cycle.

H3K9me3 can robustly be maintained in PCH via the nucleation and looping mechanism

Linking modifications of histone residues to their readout by specific protein domains is an important aspect of current theoretical models that describe how epigenetic networks establish and maintain specific chromatin states based on dynamic nucleosome modifications (Dodd et al, 2007; Angel et al, 2011; Hathaway et al, 2012; Hodges & Crabtree, 2012). These include positive feedback loops where modified histones (directly or indirectly) recruit enzymes that catalyze a similar modification on nearby nucleosomes. One class of these models is characterized by relatively robust bistable chromatin states that can stably co-exist for a certain set of conditions (Dodd et al, 2007; Angel et al, 2011). This originates from the presence of multiple positive feedback loops as well as "long-range" interactions along the nucleosome chain. To limit the spreading of a distinct modification to chromatin outside the domain under consideration, the existence of boundary factors is invoked. If H3K9me3 was able to spread within PCH via such a mechanism, one would have to explain how spreading is confined in 3D for the 28 ± 1 chromocenters per nucleus with an average volume of 2.69 ± 0.04 μm^3 or approximately 6 Mbp of DNA (Cantaloube et al, 2012). Accordingly, the cell would have to maintain a rather elaborate spherical boundary structure for the 3D confinement of H3K9me3 to PCH, for which there is no evidence. It is also noted that for H3K27me3, the view that boundary factors like CTCF are required to limit domain spreading along the nucleosome chain has been challenged by two recent studies (Schwartz et al, 2012; Van Bortle et al, 2012). Nevertheless, the "nucleation and looping" mechanism proposed here would be fully compatible with the function of insulators as architectural factors that confine the 3D organization of chromatin by establishing interactions between distant sites that would promote or inhibit long-range contacts between nucleosomes and chromatin-bound epigenetic modifiers (Ong & Corces, 2014). Furthermore, we measured that H3K9me3 was less than 2-fold reduced in euchromatin, which suggests that H3K9me3-dependent feedback loops are rather weak. For strong feedback, it would be difficult to explain why the mark would not spread throughout the rest of the genome via the same mechanism as in PCH. Finally, we did not find evidence for bistable H3K9me3 states when perturbing the balance between H3K9me3 methylation and demethylation (Figs 3A, B and 8A–C). Rather, the H3K9me3 distribution obtained from measurements of single cells in dependence of the HP1 concentration showed a gradual transition from wild-type levels to those measured in Suv39h dn cells (Fig 3B).

Recently, an alternative model derived from experiments in which HP1α was recruited to the POU5F1 promoter to induce heterochromatin formation and gene repression was introduced (Hathaway et al, 2012; Hodges & Crabtree, 2012). The experimentally determined H3K9me3 domain with smoothly decreasing borders was modeled with a 1D-lattice model for a chain of 257 nucleosomes, in which the modification is propagated by nearest-neighbor interactions from the nucleation site along the chain. Here, we detected the endogenous equivalent of these ectopic nucleation sites for high-affinity binding of SUV39H complexes in PCH. However, the constraints on protein–chromatin interactions and protein concentrations imposed from our experiments were not compatible with forming stable H3K9me3 domains via linear

nearest-neighbor spreading. Furthermore, it provided insufficient specificity with respect to the presence/absence of the high-affinity nucleation sites found in PCH versus euchromatin. In contrast, our nucleation and looping model schematically depicted in Fig 8G was found to be robust with respect to maintaining the experimentally measured PCH features: (i) It provides an intrinsic limit for the SUV39H-dependent extension of H3K9me3 within the system. (ii) Stochastic number fluctuations of cellular factors have little effect (Fig 7C and D). (iii) Perturbations of SUV39H1 binding (Fig 8A), histone demethylation activity (Fig 8C), or the concentrations of SUV39H high-affinity sites (Fig 8D) change the H3K9me3 level only gradually and in a reversible manner. (iv) Transient perturbations of the system in the range of minutes were insignificant, since the H3K9me3 propagation rate is slow with only 0.35 nucleosomes per hour (Fig 8E).

Furthermore, the response of the quantitative model (Fig 7B) toward perturbations was tested experimentally by HP1 knockdown and overexpression of the histone demethylase JMJD2C. In these experiments, a gradual change of the H3K9me3 level depending on HP1 (Figs 3A and 8A, B) or JMJD2C (Fig 8C) concentration was measured, which was reproduced by the model. Likewise, the steady-state methylation level was not bistable since the looping-mediated propagation rate of H3K9me3 decreases approximately linearly with the SUV39H occupancy at the nucleation site. This is consistent with the gradual reduction of GFP expression from the activated *POU5F1* promoter observed in MEFs after triggering HP1 recruitment (Hathaway *et al*, 2012).

Concluding Remarks

Our findings lead us to propose that in mouse fibroblast cells the PCH state is maintained by a nucleation and looping mechanism, in which the H3K9me3 modifications originate from relatively sparsely distributed nucleation sites of stably bound SUV39H complexes (Fig 4E). The local extension of the H3K9me3 modification occurs via looping of the nucleosome chain to mediate methylation of nucleosomes by a chromatin-bound HP1-SUV39H complex in spatial proximity against an unspecific demethylation activity provided by JMJD2 enzymes (Fig 8G). This mechanism is site-specific and robust toward number fluctuations of its components. SUV39H–chromatin complexes persisted through the cell cycle and could act as bookmarking factors for memorizing PCH silencing of transcription (Fig 5). Our model lacks bistable states and it does neither involve nearest-neighbor feedback loops for linear spreading of H3K9me3 nor the presence of locus-specific boundary factors to limit such a process. The predicted behavior of the system according to the nucleation and looping model in response to perturbations was in excellent agreement with the experimental findings. Additionally, it is well suited to rationalize general features of cellular systems that establish, maintain, or modulate epigenetic patterns of characteristic domain size (Erdel *et al*, 2013). The proposed mechanism is fully consistent with results of studies on the distribution of H3K9 methylation along the nucleosome chain upon chromatin-tethering of HP1 (Hathaway *et al*, 2012) or the yeast homologue of SUV39H (Kagansky *et al*, 2009), as well as with the shape of the H3K27me3 domain observed in *Arabidopsis* that is involved in silencing the floral repressor FLC (Angel *et al*, 2011). Thus, its

conceptual features might be relevant for heritable functional chromatin states at other genomic loci.

Materials and Methods

Cell lines

Experiments were conducted with GFP and RFP constructs in the murine NIH-3T3 fibroblast cell line or in immortalized mouse embryonic fibroblasts (iMEF) wild-type and mutant cell lines (Peters *et al*, 2001; Schotta *et al*, 2008; Müller *et al*, 2009). Autofluorescent proteins were either expressed as stable (inducible) cell lines or introduced via transient transfection as described in the Supplementary Materials and Methods.

Fluorescence microscopy imaging, FRAP, and FCS

Confocal imaging, FRAP and FCS experiments, and associated data analysis were conducted with a Leica TCS SP5 or Zeiss LSM 710 confocal laser scanning microscope as described previously (Müller *et al*, 2009; Erdel *et al*, 2010) and in the Supplementary Materials and Methods. Immunofluorescence was conducted with primary anti-H3K9me3 (Millipore, Abcam ab8898), anti-HP1α (Euromedex, 2HP-1H5-AS), anti-HP1β (Euromedex, 1MOD-1A9-AS), anti-HP1γ (Euromedex, 2MOD-1G6-AS) or anti-H4K20me3 (Abcam, ab9053) antibodies and a secondary goat anti-rabbit/mouse Alexa 568 antibody or anti-rabbit/mouse Alexa 633 antibody (Invitrogen, Molecular Probes).

Protein enrichments and H3K9 trimethylation levels were measured from high-resolution microscopy images using the ImageJ software as described in the Supplementary Materials and Methods. FRAP measurements were fitted either to a diffusion model, a binding model or a reaction-diffusion model that incorporates both diffusion and binding processes. The data from the model that yielded the best fit was used for further analysis and modeling (Müller *et al*, 2009).

Protein interaction analysis by FCCS, F2H, ChIP-seq and AUC

Protein–protein interaction analysis of the soluble nuclear fraction in living cells was done by FCCS (Erdel *et al*, 2010), and interactions of chromatin-bound proteins were measured via a fluorescent two-hybrid assay (F2H) in the cell nucleus as reported before (Chung *et al*, 2011). ChIP-seq experiments were conducted as described previously (Teif *et al*, 2012); the data produced have been deposited to the GEO database (accession number GSE58555). Measurements of HP1 association states with recombinant proteins were performed by analytical ultracentrifugation according to the workflow given in our previous work (Kepert *et al*, 2003; Fejes Tóth *et al*, 2005). Details on all methods and associated data analysis are given in the Supplementary Materials and Methods section.

Network modeling

The model of the epigenetic network was calculated for a chromatin fiber of 300 nucleosomes. Each nucleosome on the fiber was able to collide with others via chromatin looping following the collision

probability determined by the local concentration of one nucleosome in the proximity of the others as described previously (Rippe *et al*, 1995; Rippe, 2001; Erdel *et al*, 2013). The resulting values for an increased local concentration of nucleosomes in the proximity of the first nucleosome at the 0-position due to chromatin looping is shown in Fig 7A with the concentration of high-affinity binding sites ("origins") measured as described in the text. The model consists of a system of ordinary differential equations (ODEs). The core variables constituting the network (Fig 7B) are the local probability of methylation and the local probabilities of occupation by HP1, SUV39H, and HP1-SUV39H complex that depend on time and the position of nucleosomes and nucleation origins on DNA. The model variables, parameters, and reference values are summarized in Supplementary Table S7. For the euchromatin fiber system, the ODEs lack the nucleation origins. Stochastic kinetic traces and stochastic steady-state distributions were simulated with the Gillespie stochastic simulation algorithm (Gillespie, 2007) implemented in C++. The state of each nucleosome was derived numerically based on the deterministic formalism implemented in Mathematica 9.0 (Wolfram Research). See Supplementary Materials and Methods for details on model implementation and fitting.

Supplementary information for this article is available online: http://msb.embopress.org

Author contributions

KMO, FE, TH, and KR designed the study. KMO, JPM, AR, MH, CB, QZ, and SK acquired the experimental data. KMO, JPM, AR, MH, AM, QZ, SK, GS, TH, and KR analyzed and interpreted the data. AM, TH, FE, and KR conducted calculations and mathematical modeling. Manuscript writing was done by KMO, FE, AR, AM, TH, and KR with contributions from all authors regarding critical revisions.

Conflict of interest

The authors declare that they have no conflict of interest.

References

Aagaard L, Laible G, Selenko P, Schmid M, Dorn R, Schotta G, Kuhfittig S, Wolf A, Lebersorger A, Singh PB, Reuter G, Jenuwein T (1999) Functional mammalian homologues of the *Drosophila* PEV-modifier Su(var)3-9 encode centromere-associated proteins which complex with the heterochromatin component M31. *EMBO J* 18: 1923–1938

Agarwal N, Hardt T, Brero A, Nowak D, Rothbauer U, Becker A, Leonhardt H, Cardoso MC (2007) MeCP2 interacts with HP1 and modulates its heterochromatin association during myogenic differentiation. *Nucleic Acids Res* 35: 5402–5408

Alabert C, Bukowski-Wills JC, Lee SB, Kustatscher G, Nakamura K, de Lima Alves F, Menard P, Mejlvang J, Rappsilber J, Groth A (2014) Nascent chromatin capture proteomics determines chromatin dynamics during DNA replication and identifies unknown fork components. *Nat Cell Biol* 16: 281–293

Angel A, Song J, Dean C, Howard M (2011) A polycomb-based switch underlying quantitative epigenetic memory. *Nature* 476: 105–108

Arand J, Spieler D, Karius T, Branco MR, Meilinger D, Meissner A, Jenuwein T, Xu G, Leonhardt H, Wolf V, Walter J (2012) *In vivo* control of CpG and non-CpG DNA methylation by DNA methyltransferases. *PLoS Genet* 8: e1002750

Bachman KE, Rountree MR, Baylin SB (2001) Dnmt3a and Dnmt3b are transcriptional repressors that exhibit unique localization properties to heterochromatin. *J Biol Chem* 276: 32282–32287

Ball LJ, Murzina NV, Broadhurst RW, Raine AR, Archer SJ, Stott FJ, Murzin AG, Singh PB, Domaille PJ, Laue ED (1997) Structure of the chromatin binding (chromo) domain from mouse modifier protein 1. *EMBO J* 16: 2473–2481

Berger SL, Kouzarides T, Shiekhattar R, Shilatifard A (2009) An operational definition of epigenetics. *Genes Dev* 23: 781–783

Brero A, Easwaran HP, Nowak D, Grunewald I, Cremer T, Leonhardt H, Cardoso MC (2005) Methyl CpG-binding proteins induce large-scale chromatin reorganization during terminal differentiation. *J Cell Biol* 169: 733–743

Bulut-Karslioglu A, Perrera V, Scaranaro M, de la Rosa-Velazquez IA, van de Nobelen S, Shukeir N, Popow J, Gerle B, Opravil S, Pagani M, Meidhof S, Brabletz T, Manke T, Lachner M, Jenuwein T (2012) A transcription factor-based mechanism for mouse heterochromatin formation. *Nat Struct Mol Biol* 19: 1023–1030

Byrum SD, Taverna SD, Tackett AJ (2013) Purification of a specific native genomic locus for proteomic analysis. *Nucleic Acids Res* 41: e195.

Campos EI, Reinberg D (2009) Histones: annotating chromatin. *Annu Rev Genet* 43: 559–599

Cantaloube S, Romeo K, Le Baccon P, Almouzni G, Quivy JP (2012) Characterization of chromatin domains by 3D fluorescence microscopy: an automated methodology for quantitative analysis and nuclei screening. *BioEssays* 34: 509–517

Cheutin T, McNairn AJ, Jenuwein T, Gilbert DM, Singh PB, Misteli T (2003) Maintenance of stable heterochromatin domains by dynamic HP1 binding. *Science* 299: 721–725

Chin HG, Esteve PO, Pradhan M, Benner J, Patnaik D, Carey MF, Pradhan S (2007) Automethylation of G9a and its implication in wider substrate specificity and HP1 binding. *Nucleic Acids Res* 35: 7313–7323

Chung I, Leonhardt H, Rippe K (2011) *De novo* assembly of a PML nuclear subcompartment occurs through multiple pathways and induces telomere elongation. *J Cell Sci* 124: 3603–3618

Clapier CR, Cairns BR (2009) The biology of chromatin remodeling complexes. *Annu Rev Biochem* 78: 273–304

Craig JM, Earle E, Canham P, Wong LH, Anderson M, Choo KH (2003) Analysis of mammalian proteins involved in chromatin modification reveals new metaphase centromeric proteins and distinct chromosomal distribution patterns. *Hum Mol Genet* 12: 3109–3121

Dialynas GK, Terjung S, Brown JP, Aucott RL, Baron-Luhr B, Singh PB, Georgatos SD (2007) Plasticity of HP1 proteins in mammalian cells. *J Cell Sci* 120: 3415–3424

Dodd IB, Micheelsen MA, Sneppen K, Thon G (2007) Theoretical analysis of epigenetic cell memory by nucleosome modification. *Cell* 129: 813–822

Easwaran HP, Schermelleh L, Leonhardt H, Cardoso MC (2004) Replication-independent chromatin loading of Dnmt1 during G2 and M phases. *EMBO Rep* 5: 1181 – 1186

Efroni S, Duttagupta R, Cheng J, Dehghani H, Hoeppner DJ, Dash C, Bazett-Jones DP, Le Grice S, McKay RD, Buetow KH, Gingeras TR, Misteli T, Meshorer E (2008) Global transcription in pluripotent embryonic stem cells. *Cell Stem Cell* 2: 437 – 447

Eissenberg JC, Reuter G (2009) Cellular mechanism for targeting heterochromatin formation in *Drosophila*. *Int Rev Cell Mol Biol* 273: 1 – 47

Erdel F, Schubert T, Marth C, Langst G, Rippe K (2010) Human ISWI chromatin-remodeling complexes sample nucleosomes via transient binding reactions and become immobilized at active sites. *Proc Natl Acad Sci USA* 107: 19873 – 19878

Erdel F, Krug J, Längst G, Rippe K (2011a) Targeting chromatin remodelers: signals and search mechanisms. *Biochim Biophys Acta* 1809: 497 – 508

Erdel F, Müller-Ott K, Baum M, Wachsmuth M, Rippe K (2011b) Dissecting chromatin interactions in living cells from protein mobility maps. *Chromosome Res* 19: 99 – 115

Erdel F, Müller-Ott K, Rippe K (2013) Establishing epigenetic domains via chromatin-bound histone modifiers. *Ann N Y Acad Sci* 1305: 29 – 43

Esteve PO, Chin HG, Smallwood A, Feehery GR, Gangisetty O, Karpf AR, Carey MF, Pradhan S (2006) Direct interaction between DNMT1 and G9a coordinates DNA and histone methylation during replication. *Genes Dev* 20: 3089 – 3103

Fejes Tóth K, Mazurkiewicz J, Rippe K (2005) Association states of the nucleosome assembly protein 1 and its complexes with histones. *J Biol Chem* 280: 15690 – 15699

Festenstein R, Pagakis SN, Hiragami K, Lyon D, Verreault A, Sekkali B, Kioussis D (2003) Modulation of heterochromatin protein 1 dynamics in primary Mammalian cells. *Science* 299: 719 – 721

Fischle W, Wang Y, Jacobs SA, Kim Y, Allis CD, Khorasanizadeh S (2003) Molecular basis for the discrimination of repressive methyl-lysine marks in histone H3 by polycomb and HP1 chromodomains. *Genes Dev* 17: 1870 – 1881

Fischle W, Tseng BS, Dormann HL, Ueberheide BM, Garcia BA, Shabanowitz J, Hunt DF, Funabiki H, Allis CD (2005) Regulation of HP1-chromatin binding by histone H3 methylation and phosphorylation. *Nature* 438: 1116 – 1122

Fodor BD, Kubicek S, Yonezawa M, O'Sullivan RJ, Sengupta R, Perez-Burgos L, Opravil S, Mechtler K, Schotta G, Jenuwein T (2006) Jmjd2b antagonizes H3K9 trimethylation at pericentric heterochromatin in mammalian cells. *Genes Dev* 20: 1557 – 1562

Fodor BD, Shukeir N, Reuter G, Jenuwein T (2010) Mammalian Su(var) genes in chromatin control. *Annu Rev Cell Dev Biol* 26: 471 – 501

Fujita N, Takebayashi S, Okumura K, Kudo S, Chiba T, Saya H, Nakao M (1999) Methylation-mediated transcriptional silencing in euchromatin by methyl-CpG binding protein MBD1 isoforms. *Mol Cell Biol* 19: 6415 – 6426

Fujita N, Watanabe S, Ichimura T, Tsuruzoe S, Shinkai Y, Tachibana M, Chiba T, Nakao M (2003) Methyl-CpG binding domain 1 (MBD1) interacts with the Suv39h1-HP1 heterochromatic complex for DNA methylation-based transcriptional repression. *J Biol Chem* 278: 24132 – 24138

Fuks F, Hurd PJ, Deplus R, Kouzarides T (2003) The DNA methyltransferases associate with HP1 and the SUV39H1 histone methyltransferase. *Nucleic Acids Res* 31: 2305 – 2312

Fuks F (2005) DNA methylation and histone modifications: teaming up to silence genes. *Curr Opin Genet Dev* 15: 490 – 495

Gillespie DT (2007) Stochastic simulation of chemical kinetics. *Annu Rev Phys Chem* 58: 35 – 55

Grewal SI, Jia S (2007) Heterochromatin revisited. *Nat Rev Genet* 8: 35 – 46

Hahn M, Dambacher S, Dulev S, Kuznetsova AY, Eck S, Worz S, Sadic D, Schulte M, Mallm JP, Maiser A, Debs P, von Melchner H, Leonhardt H, Schermelleh L, Rohr K, Rippe K, Storchova Z, Schotta G (2013) Suv4-20h2 mediates chromatin compaction and is important for cohesin recruitment to heterochromatin. *Genes Dev* 27: 859 – 872

Haldar S, Saini A, Nanda JS, Saini S, Singh J (2011) Role of Swi6/HP1 self-association-mediated recruitment of Clr4/Suv39 in establishment and maintenance of heterochromatin in fission yeast. *J Biol Chem* 286: 9308 – 9320

Hathaway NA, Bell O, Hodges C, Miller EL, Neel DS, Crabtree GR (2012) Dynamics and memory of heterochromatin in living cells. *Cell* 149: 1447 – 1460

Hayakawa T, Haraguchi T, Masumoto H, Hiraoka Y (2003) Cell cycle behavior of human HP1 subtypes: distinct molecular domains of HP1 are required for their centromeric localization during interphase and metaphase. *J Cell Sci* 116: 3327 – 3338

Hiragami K, Festenstein R (2005) Heterochromatin protein 1: a pervasive controlling influence. *Cell Mol Life Sci* 62: 2711 – 2726

Hirota T, Lipp JJ, Toh BH, Peters JM (2005) Histone H3 serine 10 phosphorylation by Aurora B causes HP1 dissociation from heterochromatin. *Nature* 438: 1176 – 1180

Hodges C, Crabtree GR (2012) Dynamics of inherently bounded histone modification domains. *Proc Natl Acad Sci USA* 109: 13296 – 13301

Jacobs SA, Khorasanizadeh S (2002) Structure of HP1 chromodomain bound to a lysine 9-methylated histone H3 tail. *Science* 295: 2080 – 2083

Jacobs SA, Fischle W, Khorasanizadeh S (2004) Assays for the determination of structure and dynamics of the interaction of the chromodomain with histone peptides. *Meth Enzymol* 376: 131 – 148

Kagansky A, Folco HD, Almeida R, Pidoux AL, Boukaba A, Simmer F, Urano T, Hamilton GL, Allshire RC (2009) Synthetic heterochromatin bypasses RNAi and centromeric repeats to establish functional centromeres. *Science* 324: 1716 – 1719

Kepert JF, Fejes Tóth K, Caudron M, Mücke N, Langowski J, Rippe K (2003) Conformation of reconstituted mononucleosomes and effect of linker histone H1 binding studied by scanning force microscopy. *Biophys J* 85: 4012 – 4022

Kind J, Pagie L, Ortabozkoyun H, Boyle S, de Vries SS, Janssen H, Amendola M, Nolen LD, Bickmore WA, van Steensel B (2013) Single-cell dynamics of genome-nuclear lamina interactions. *Cell* 153: 178 – 192

Kourmouli N, Jeppesen P, Mahadevhaiah S, Burgoyne P, Wu R, Gilbert DM, Bongiorni S, Prantera G, Fanti L, Pimpinelli S, Shi W, Fundele R, Singh PB (2004) Heterochromatin and tri-methylated lysine 20 of histone H4 in animals. *J Cell Sci* 117: 2491 – 2501

Krouwels IM, Wiesmeijer K, Abraham TE, Molenaar C, Verwoerd NP, Tanke HJ, Dirks RW (2005) A glue for heterochromatin maintenance: stable SUV39H1 binding to heterochromatin is reinforced by the SET domain. *J Cell Biol* 170: 537 – 549

Kwon SH, Workman JL (2008) The heterochromatin protein 1 (HP1) family: put away a bias toward HP1. *Mol Cells* 26: 217 – 227

Lachner M, O'Carroll D, Rea S, Mechtler K, Jenuwein T (2001) Methylation of histone H3 lysine 9 creates a binding site for HP1 proteins. *Nature* 410: 116 – 120

Lehnertz B, Ueda Y, Derijck AA, Braunschweig U, Perez-Burgos L, Kubicek S, Chen T, Li E, Jenuwein T, Peters AH (2003) Suv39h-mediated histone H3

lysine 9 methylation directs DNA methylation to major satellite repeats at pericentric heterochromatin. *Curr Biol* 13: 1192–1200

Lewis JD, Meehan RR, Henzel WJ, Maurer-Fogy I, Jeppesen P, Klein F, Bird A (1992) Purification, sequence, and cellular localization of a novel chromosomal protein that binds to methylated DNA. *Cell* 69: 905–914

Lorthongpanich C, Cheow LF, Balu S, Quake SR, Knowles BB, Burkholder WF, Solter D, Messerschmidt DM (2013) Single-cell DNA-methylation analysis reveals epigenetic chimerism in preimplantation embryos. *Science* 341: 1110–1112

Loyola A, Tagami H, Bonaldi T, Roche D, Quivy JP, Imhof A, Nakatani Y, Dent SY, Almouzni G (2009) The HP1alpha-CAF1-SetDB1-containing complex provides H3K9me1 for Suv39-mediated K9me3 in pericentric heterochromatin. *EMBO Rep* 10: 769–775

Lunyak VV, Burgess R, Prefontaine GG, Nelson C, Sze SH, Chenoweth J, Schwartz P, Pevzner PA, Glass C, Mandel G, Rosenfeld MG (2002) Corepressor-dependent silencing of chromosomal regions encoding neuronal genes. *Science* 298: 1747–1752

Maison C, Almouzni G (2004) HP1 and the dynamics of heterochromatin maintenance. *Nat Rev Mol Cell Biol* 5: 296–304

Maison C, Bailly D, Roche D, de Oca RM, Probst AV, Vassias I, Dingli F, Lombard B, Loew D, Quivy JP, Almouzni G (2011) SUMOylation promotes *de novo* targeting of HP1alpha to pericentric heterochromatin. *Nat Genet* 43: 220–227

Martens JH, O'Sullivan RJ, Braunschweig U, Opravil S, Radolf M, Steinlein P, Jenuwein T (2005) The profile of repeat-associated histone lysine methylation states in the mouse epigenome. *EMBO J* 24: 800–812

Mateescu B, England P, Halgand F, Yaniv M, Muchardt C (2004) Tethering of HP1 proteins to chromatin is relieved by phosphoacetylation of histone H3. *EMBO Rep* 5: 490–496

McBryant SJ, Adams VH, Hansen JC (2006) Chromatin architectural proteins. *Chromosome Res* 14: 39–51

McManus KJ, Biron VL, Heit R, Underhill DA, Hendzel MJ (2006) Dynamic changes in histone H3 lysine 9 methylations: identification of a mitosis-specific function for dynamic methylation in chromosome congression and segregation. *J Biol Chem* 281: 8888–8897

Meissner A, Mikkelsen TS, Gu H, Wernig M, Hanna J, Sivachenko A, Zhang X, Bernstein BE, Nusbaum C, Jaffe DB, Gnirke A, Jaenisch R, Lander ES (2008) Genome-scale DNA methylation maps of pluripotent and differentiated cells. *Nature* 454: 766–770

Melcher M, Schmid M, Aagaard L, Selenko P, Laible G, Jenuwein T (2000) Structure-function analysis of SUV39H1 reveals a dominant role in heterochromatin organization, chromosome segregation, and mitotic progression. *Mol Cell Biol* 20: 3728–3741

Meshorer E, Misteli T (2006) Chromatin in pluripotent embryonic stem cells and differentiation. *Nat Rev Mol Cell Biol* 7: 540–546

Müller KP, Erdel F, Caudron-Herger M, Marth C, Fodor BD, Richter M, Scaranaro M, Beaudouin J, Wachsmuth M, Rippe K (2009) Multiscale analysis of dynamics and interactions of heterochromatin protein 1 by fluorescence fluctuation microscopy. *Biophys J* 97: 2876–2885

Nan X, Tate P, Li E, Bird A (1996) DNA methylation specifies chromosomal localization of MeCP2. *Mol Cell Biol* 16: 414–421

Nielsen AL, Oulad-Abdelghani M, Ortiz JA, Remboutsika E, Chambon P, Losson R (2001) Heterochromatin formation in mammalian cells: interaction between histones and HP1 proteins. *Mol Cell* 7: 729–739

Nozawa RS, Nagao K, Masuda HT, Iwasaki O, Hirota T, Nozaki N, Kimura H, Obuse C (2010) Human POGZ modulates dissociation of HP1alpha from mitotic chromosome arms through Aurora B activation. *Nat Cell Biol* 12: 719–727

Ohta S, Bukowski-Wills JC, Sanchez-Pulido L, Alves Fde L, Wood L, Chen ZA, Platani M, Fischer L, Hudson DF, Ponting CP, Fukagawa T, Earnshaw WC, Rappsilber J (2010) The protein composition of mitotic chromosomes determined using multiclassifier combinatorial proteomics. *Cell* 142: 810–821

Ong CT, Corces VG (2014) CTCF: an architectural protein bridging genome topology and function. *Nat Rev Genet* 15: 234–246

Park SH, Yu SE, Chai YG, Jang YK (2014) CDK2-dependent phosphorylation of Suv39H1 is involved in control of heterochromatin replication during cell cycle progression. *Nucleic Acids Res* 42: 6196–6207

Peters AH, O'Carroll D, Scherthan H, Mechtler K, Sauer S, Schofer C, Weipoltshammer K, Pagani M, Lachner M, Kohlmaier A, Opravil S, Doyle M, Sibilia M, Jenuwein T (2001) Loss of the Suv39h histone methyltransferases impairs mammalian heterochromatin and genome stability. *Cell* 107: 323–337

Probst AV, Almouzni G (2008) Pericentric heterochromatin: dynamic organization during early development in mammals. *Differentiation* 76: 15–23

Ringrose L, Chabanis S, Angrand PO, Woodroofe C, Stewart AF (1999) Quantitative comparison of DNA looping *in vitro* and *in vivo*: chromatin increases effective DNA flexibility at short distances. *EMBO J* 18: 6630–6641

Rippe K, von Hippel PH, Langowski J (1995) Action at a distance: DNA-looping and initiation of transcription. *Trends Biochem Sci* 20: 500–506

Rippe K (2001) Making contacts on a nucleic acid polymer. *Trends Biochem Sci* 26: 733–740

Rosnoblet C, Vandamme J, Volkel P, Angrand PO (2011) Analysis of the human HP1 interactome reveals novel binding partners. *Biochem Biophys Res Com* 413: 206–211

Rothbauer U, Zolghadr K, Muyldermans S, Schepers A, Cardoso MC, Leonhardt H (2008) A versatile nanotrap for biochemical and functional studies with fluorescent fusion proteins. *Mol Cell Proteomics* 7: 282–289

Schermelleh L, Haemmer A, Spada F, Rosing N, Meilinger D, Rothbauer U, Cardoso MC, Leonhardt H (2007) Dynamics of Dnmt1 interaction with the replication machinery and its role in postreplicative maintenance of DNA methylation. *Nucleic Acids Res* 35: 4301–4312

Schmiedeberg L, Weisshart K, Diekmann S, Meyer Zu Hoerste G, Hemmerich P (2004) High- and low-mobility populations of HP1 in heterochromatin of mammalian cells. *Mol Biol Cell* 15: 2819–2833

Schotta G, Ebert A, Krauss V, Fischer A, Hoffmann J, Rea S, Jenuwein T, Dorn R, Reuter G (2002) Central role of *Drosophila* SU(VAR)3-9 in histone H3-K9 methylation and heterochromatic gene silencing. *EMBO J* 21: 1121–1131

Schotta G, Lachner M, Sarma K, Ebert A, Sengupta R, Reuter G, Reinberg D, Jenuwein T (2004) A silencing pathway to induce H3-K9 and H4-K20 trimethylation at constitutive heterochromatin. *Genes Dev* 18: 1251–1262

Schotta G, Sengupta R, Kubicek S, Malin S, Kauer M, Callen E, Celeste A, Pagani M, Opravil S, De La Rosa-Velazquez IA, Espejo A, Bedford M, Nussenzweig A, Busslinger M, Jenuwein T (2008) A chromatin-wide transition to H4K20 mono-methylation impairs genome integrity and programmed DNA rearrangements in the mouse. *Genes Dev* 22: 2048–2061

Schreiber SL, Bernstein BE (2002) Signaling network model of chromatin. *Cell* 111: 771–778

Schwartz YB, Linder-Basso D, Kharchenko PV, Tolstorukov MY, Kim M, Li HB, Gorchakov AA, Minoda A, Shanower G, Alekseyenko AA, Riddle NC, Jung YL, Gu T, Plachetka A, Elgin SC, Kuroda MI, Park PJ, Savitsky M, Karpen GH, Pirrotta V (2012) Nature and function of insulator protein binding sites in the Drosophila genome. *Genome Res* 22: 2188–2198

Sedighi M, Sengupta AM (2007) Epigenetic chromatin silencing: bistability and front propagation. *Phys Biol* 4: 246−255

Sims JK, Wade PA (2011) Mi-2/NuRD complex function is required for normal S phase progression and assembly of pericentric heterochromatin. *Mol Biol Cell* 22: 3094−3102

Smallwood A, Esteve PO, Pradhan S, Carey M (2007) Functional cooperation between HP1 and DNMT1 mediates gene silencing. *Genes Dev* 21: 1169−1178

Sneppen K, Micheelsen MA, Dodd IB (2008) Ultrasensitive gene regulation by positive feedback loops in nucleosome modification. *Mol Syst Biol* 4: 182

Souza PP, Volkel P, Trinel D, Vandamme J, Rosnoblet C, Heliot L, Angrand PO (2009) The histone methyltransferase SUV420H2 and heterochromatin proteins HP1 interact but show different dynamic behaviours. *BMC Cell Biol* 10: 41

van Steensel B, Henikoff S (2000) Identification of *in vivo* DNA targets of chromatin proteins using tethered dam methyltransferase. *Nat Biotechnol* 18: 424−428

Tachibana M, Sugimoto K, Nozaki M, Ueda J, Ohta T, Ohki M, Fukuda M, Takeda N, Niida H, Kato H, Shinkai Y (2002) G9a histone methyltransferase plays a dominant role in euchromatic histone H3 lysine 9 methylation and is essential for early embryogenesis. *Genes Dev* 16: 1779−1791

Taddei A, Maison C, Roche D, Almouzni G (2001) Reversible disruption of pericentric heterochromatin and centromere function by inhibiting deacetylases. *Nat Cell Biol* 3: 114−120

Taverna SD, Li H, Ruthenburg AJ, Allis CD, Patel DJ (2007) How chromatin-binding modules interpret histone modifications: lessons from professional pocket pickers. *Nat Struct Mol Biol* 14: 1025−1040

Teif VB, Vainshtein Y, Caudron-Herger M, Mallm JP, Marth C, Hofer T, Rippe K (2012) Genome-wide nucleosome positioning during embryonic stem cell development. *Nat Struct Mol Biol* 19: 1185−1191

Thatcher KN, LaSalle JM (2006) Dynamic changes in Histone H3 lysine 9 acetylation localization patterns during neuronal maturation require MeCP2. *Epigenetics* 1: 24−31

Thiru A, Nietlispach D, Mott HR, Okuwaki M, Lyon D, Nielsen PR, Hirshberg M, Verreault A, Murzina NV, Laue ED (2004) Structural basis of HP1/PXVXL motif peptide interactions and HP1 localisation to heterochromatin. *EMBO J* 23: 489−499

Van Bortle K, Ramos E, Takenaka N, Yang J, Wahi JE, Corces VG (2012) Drosophila CTCF tandemly aligns with other insulator proteins at the borders of H3K27me3 domains. *Genome Res* 22: 2176−2187

Vaquero A, Scher M, Erdjument-Bromage H, Tempst P, Serrano L, Reinberg D (2007) SIRT1 regulates the histone methyl-transferase SUV39H1 during heterochromatin formation. *Nature* 450: 440−444

Wang D, Zhou J, Liu X, Lu D, Shen C, Du Y, Wei FZ, Song B, Lu X, Yu Y, Wang L, Zhao Y, Wang H, Yang Y, Akiyama Y, Zhang H, Zhu WG (2013) Methylation of SUV39H1 by SET7/9 results in heterochromatin relaxation and genome instability. *Proc Natl Acad Sci USA* 110: 5516−5521

Waterston RH, Lindblad-Toh K, Birney E, Rogers J, Abril JF, Agarwal P, Agarwala R, Ainscough R, Alexandersson M, An P, Antonarakis SE, Attwood J, Baertsch R, Bailey J, Barlow K, Beck S, Berry E, Birren B, Bloom T, Bork P *et al* (2002) Initial sequencing and comparative analysis of the mouse genome. *Nature* 420: 520−562

Wilson VL, Jones PA (1984) Chemical carcinogen-mediated decreases in DNA 5-methylcytosine content of BALB/3T3 cells. *Carcinogenesis* 5: 1027−1031

Xin H, Yoon HG, Singh PB, Wong J, Qin J (2004) Components of a pathway maintaining histone modification and heterochromatin protein 1 binding at the pericentric heterochromatin in Mammalian cells. *J Biol Chem* 279: 9539−9546

Yamagata K, Yamazaki T, Miki H, Ogonuki N, Inoue K, Ogura A, Baba T (2007) Centromeric DNA hypomethylation as an epigenetic signature discriminates between germ and somatic cell lineages. *Dev Biol* 312: 419−426

Yamamoto K, Sonoda M (2003) Self-interaction of heterochromatin protein 1 is required for direct binding to histone methyltransferase, SUV39H1. *Biochem Biophys Res Com* 301: 287−292

Zee BM, Levin RS, Xu B, LeRoy G, Wingreen NS, Garcia BA (2010) *In vivo* residue-specific histone methylation dynamics. *J Biol Chem* 285: 3341−3350

Zolghadr K, Mortusewicz O, Rothbauer U, Kleinhans R, Goehler H, Wanker EE, Cardoso MC, Leonhardt H (2008) A fluorescent two-hybrid assay for direct visualization of protein interactions in living cells. *Mol Cell Proteomics* 7: 2279−2287

Supplementary Information

Specificity, propagation and memory of pericentric heterochromatin

Katharina Müller-Ott, Fabian Erdel, Anna Matveeva, Jan-Philipp Mallm, Anne Rademacher, Matthias Hahn, Caroline Bauer, Qin Zhang, Sabine Kaltofen, Gunnar Schotta, Thomas Höfer, Karsten Rippe

Content

Supplementary Materials and Methods

- Plasmid vectors and cell lines
- Cell culture, transfections and siRNA knockdown
- Immunostaining
- Immunoprecipitation, gel electrophoretic analysis and western blots
- Real-time quantitative PCR (RT-qPCR)
- Analytical ultracentrifugation of recombinant HP1 proteins
- Chromatin immunoprecipitation and ChIP-seq data analysis
- Confocal laser scanning microscopy (CLSM) and image analysis
- Fluorescence recovery after photobleaching (FRAP) and fluorescence (cross-) correlation spectroscopy (FCS/FCCS) data acquisition
- Testing the SUV39H long-range methylation activity via a lamina-recruitment assay
- Measurements of endogenous protein concentrations and calculation of free protein fraction
- Protein-protein interaction analysis via the fluorescent two-hybrid (F2H) assay

Supplementary Data Analysis

- Fluorescence recovery after photobleaching
- Fluorescence correlation spectroscopy
- Fluorescence cross-correlation spectroscopy
- Estimates of kinetic association rate and equilibrium dissociation constants for SUV39H and HP1
- Calculation of H3K9me3 levels
- Mathematical modeling of the pericentric heterochromatin network

Supplementary Tables S1-S7

- Table S1. FCS analysis of HP1α, HP1β, HP1γ and SUV39H1.
- Table S2. FRAP analysis of GFP-tagged proteins.
- Table S3. Measured and calculated molecular weights and hydrodynamic parameters.
- Table S4. Summary of protein-protein associations.
- Table S5. Perturbations of PCH features.
- Table S6. Cell cycle-dependent mobility of SUV39H1 and HP1α.
- Table S7. Parameters used for modeling the PCH network.

Supplementary Figures S1-S5

- Figure S1. CLSM images of nuclear localization of PCH factors in NIH-3T3 mouse embryonic fibroblasts.
- Figure S2. Major repeat transcription measured by RT-qPCR and CLSM analysis of PCH organization in different cell types and knock-out cell lines.
- Figure S3. Quantification of protein parameters in living cells by FCS and FRAP
- Figure S4. FRAP analysis of JMJD2C, PAX3 and HP1β in *Suv39h* dn and *Suv4-20h* dn cells.
- Figure S5. Protein-protein interaction analysis of HP1 and SUV39H1 by FCCS and F2H experiments.

Supplementary References

Supplementary Materials and Methods

Plasmid vectors and cell lines

The coding sequences of mouse HP1α, HP1β and HP1γ were cloned into pEGFP-C1 (Clontech) or pTagRFP-C1 (Evrogen) to construct expression vectors for the autofluorescent fusion proteins GFP-HP1α/β/γ or TagRFP-HP1α/β/γ. As an *in vivo* detector for H3K9me3 the chromodomain (CD) of HP1β was inserted into pTagRFP-N. The murine SUV39H1 coding sequence was cloned into either the pEGFP-N1 (Clontech) or the pTagRFP-C1/-N1 (Evrogen) vector (in the following abbreviated as RFP) to generate fluorescently labeled SUV39H1 constructs. The point mutations H320R and H324L (Rea et al, 2000) were introduced into the *Suv39h1* sequence and cloned into the pEGFP-C1 vector. Murine SUV39H2, SUV4-20H1 and SUV4-20H2 were transferred into the vectors pEGFP-N1 or pmCHERRY-N1. Plasmids with GFP-tagged methyl-CpG-binding proteins MBD1, MBD2, MBD3 and MECP2 were kindly provided by Adrian Bird. The pJMJD2C-GFP plasmid was obtained from Barna Fodor (Fodor et al, 2006) and pPAX3/5/7-EGFP and pCAGGS-PAX9-EGFP IRES-Puro were kindly provided by Thomas Jenuwein (Bulut-Karslioglu et al, 2012).

The mRFP1-labeled histone H2A (H2A-RFP) and the GFP-binder (GBP)-LacI construct were described previously (Chung et al, 2011; Jegou et al, 2009) as was the GBP-Lamin B1 plasmid (Rothbauer et al, 2008) and the GFP-HP1α NIH-3T3 cell line (Müller et al, 2009). GFP-HP1β, GFP-HP1γ and H2A-RFP expressing NIH-3T3 clones were derived after stable transfection with the plasmids described above. The NIH-3T3 SUV39H1-GFP Tet-off cell line was kindly provided by Masato Yonezawa and Thomas Jenuwein. To investigate the interdependencies of protein binding and protein mobility, we compared measurements in wild-type immortalized mouse embryonic fibroblast (iMEF wt) cells and double-null (dn) mutant cells for either the H3K9-specific or the H4K20-specific histone methylases. Both cell lines, iMEF *Suv39h* dn and iMEF *Suv4-20h* dn have been described previously in (Peters et al, 2001) and (Schotta et al, 2008). Protein recruitment experiments were conducted in a human osteosarcoma U2OS cell line with stably integrated *lac* operator (*lac*O) arrays at three different telomeres (clone F6B2) (Jegou et al, 2009).

Cell culture, transfections and siRNA knockdown

NIH-3T3 cells and derived cell lines as well as the mouse embryonic fibroblast cell lines were cultured in DMEM high glucose medium containing 2 mM L-glutamine (PAA) supplemented with 10 % FCS (PAA) and 1 % penicillin/streptomycin (PAA). For NIH-3T3

SUV39H1-GFP cells 3 µg/ml doxycycline was added to the culture medium to prevent protein overexpression. For induction, the cells were transferred to a new dish without doxycycline two days before the experiment. U2OS F6B2 cells were cultured in regular DMEM medium supplemented with 2 mM L-glutamine, 10 % FCS and 1 % penicillin/streptomycin. For FRAP and FCS experiments, cells were cultured in Labtek chambers (Nunc) and were kept in standard medium using a CO_2-connected environmental chamber. Alternatively, Leibovitz's L15 medium (Invitrogen) supplemented with 10 % FCS and 1 % penicillin/streptomycin was used during live experiments. For mobility measurements in mitotic NIH-3T3 SUV39H1-GFP cells, nocodazole (Sigma) was added for 19 h at a final concentration of 100 ng/ml to increase the number of mitotic cells. Inhibition of histone deacetylases in NIH-3T3 or NIH-3T3 SUV39H1-GFP cells was conducted by addition of trichostatin A (TSA) to the medium for up to 5 days at a concentration of 100 ng/ml. Medium and TSA were renewed daily.

Mouse embryonic stem cells (ESCs) from 129P2/Ola mice were cultured in Powerstem ESPro1 medium (Pan-Biotech). Neural progenitor cells (NPCs) were generated from ESCs. The differentiation into NPCs was induced by formation of embryoid bodies in Stempan medium (Pan-Biotech) for 4 d followed by treatment with 5 µM retinoic acid for 4 d. Neuronal embryoid bodies were dissociated and seeded on matrigel (BD Biosciences) in neuronal stem cell medium (Pan-Biotech) for 4 d. Transient (co-)transfection of cells was performed with lipofectamine 2000 (Invitrogen) or turbofect reagent (Thermo Scientific) according to the manufacturers' protocol. Lipofectamine 2000 was used for the transfection of siRNAs against HP1α, HP1β and HP1γ or a mock siRNA (silencer select siRNAs, Ambion: HP1α (Cbx5) 5'-CAC AGA UUG UGA UAG CAU UTT-3', HP1β (Cbx1) 5'-GGA UUG CCC UGA CCU UAU UTT-3', HP1γ (Cbx3) 5'-CAC AGA UGC UGA UAA UAC UTT-3', negative control #2). A mix of 60-120 nM of each siRNA was added to the cells. Cells were fixed and immunostained for microscopy analysis after 48 h. For transfection of human cells (U2OS F6B2) the effectene transfection reagent (Qiagen) was used according to the manufacturers' protocol and cells were fixed 24 h after transfection.

Immunostaining

For immunofluorescence imaging, cells were fixed on glass coverslips with 4 % paraformaldehyde, permeabilized for 3-5 min with 0.5 % triton X-100 in PBS or CSK-buffer (100 mM NaCl, 300 mM sucrose, 3 mM $MgCl_2$ and 10 mM PIPES pH 6.8, 0.5 % triton X-100) and blocked with 10 % goat serum in PBS or alternatively with 3 % BSA in PBS.

Immunostaining of fixed cells was conducted with primary anti-H3K9me3 (Millipore; Abcam ab8898), anti-HP1α (Euromedex, 2HP-1H5-AS), anti-HP1β (Euromedex, 1MOD-1A9-AS), anti-HP1γ (Euromedex, 2MOD-1G6-AS), anti-H4K20me3 (Abcam, ab9053) or anti-5-methylcytosine (Calbiochem, 16233D3) antibodies, and subsequent visualization was performed with a secondary goat anti-rabbit/mouse Alexa 568 antibody or anti-rabbit/mouse Alexa 633 antibody (Invitrogen). Cells were mounted with Prolong Gold antifade reagent (Invitrogen) containing 4',6-diamidino-2'-phenylindole (DAPI) for the staining of chromatin/DNA. For immunofluorescent labeling of 5-methylcytosine, fixed cells were denatured with 4 N HCl and 1 % triton X-100 in water for 15 min. After three washing steps with PBS supplemented with 0.002 % NP-40, blocking and antibody labeling was conducted as described above.

Immunoprecipitation, gel electrophoretic analysis and western blots

NIH-3T3 cells stably expressing GFP-HP1β and GFP-HP1γ were lysed in an ice-cold buffer containing 10 mM Tris-HCl pH 7.5, 150 mM NaCl, 0.5 mM EDTA, 0.1 % NP-40, 1 mM PMSF, and a complete protease inhibitor cocktail (Roche) for 30 min. For the analysis of the lowly abundant SUV39H1, NIH-3T3 SUV39H1-GFP cells were induced for 48 h and lysed with a buffer containing 50 mM Tris-HCl, pH 7.5, 200 mM NaCl, 5 mM EDTA, 1 % triton X-100 supplemented with PMSF and protease inhibitor cocktail. Subsequently, endogenous and GFP-tagged SUV39H1 were immunoprecipitated to concentrate the protein by addition of 2.5 µg of anti-SUV39H1 antibody (Abcam ab38637) bound to protein G magnetic beads (Roth) at 4 °C overnight and crosslinked to the beads with DMP (dimethyl pimelimidate dihydrochloride). Antigen was eluted from the beads with 0.1 M glycine pH 2.5, and samples were analyzed by SDS-PAGE. Further analysis was either by Coomassie staining for immunoprecipitated SUV39H1 or by western blotting after transfer to a nitrocellulose membrane (Whatman) with the following primary antibodies: anti-HP1β (Abcam, ab10478, 1 : 500), anti-HP1γ (Euromedex, 2MOD-1G6-AS, 1 : 1000) and anti-SUV39H1 (Cell Signaling, 1 : 800) and HRP-conjugated anti-mouse IgG or anti-rabbit IgG secondary antibodies (Cell Signaling, 1:1000).

For quantification a chemiluminescent ECL reagent (1 ml 0.1 M Tris-HCl, pH 7.5 supplemented with 0.25 mg luminol, 0.3 µl H_2O_2, 100 µl DMSO, 0.11 mg para-hydroxycoumarin acid) was used and the signal was recorded using an INTAS ChemoCam Imager equipped with a 16-bit camera. The protein ratio was quantified with an ImageJ-based intensity analysis of the protein bands from western blots (HP1α/β/γ).

Real-time quantitative PCR (RT-qPCR)

Total RNA was extracted from three different samples (ESCs, iMEF wt and iMEF *Suv39h* dn cells) with the RNeasy Mini Kit (Qiagen) including an additional DNase digestion step with 50 U DNase I at 37 °C for 1 h. First-strand cDNA was transcribed from 2 µg RNA using 8.3 µM random hexamer primers (Thermo Scientific), 0.83 mM dNTPs and 10 U/µl SuperScript II reverse transcriptase (Invitrogen). Residual RNA fragments were digested by addition of 10 U RNase H. 1 % of the cDNA was used as input for the RT-qPCR conducted with a Light Cycler 480 SybrGreen I Master mix (Roche) and 0.5 µM of specific primers with a StepOne Real Time PCR-System (Applied Biosystems). For the RT-qPCR standard curve total RNA (20 µg/µl) of ESCs was used and the resulting cDNA was applied from 0.2-60 ng/µl. The following primer sequences were used: minor forward, 5'-AAT GAT AAA AAC CAC ACT GTA GAA CAT-3', minor reverse, 5'-ATG TTT CTC ATT GTA ACT CAT TGA TAT AC-3', major forward, 5'-TGG CGA GAA AAC TGA AAA TCA CG-3', major reverse, 5'-TCT TGC CAT ATT CCA CGT CCT AC-3', GAPDH forward, 5'-TAT GTC GTG GAG TCT ACT GG-3' and GAPDH reverse 5'-ACA CCC ATC ACA AAC ATG GG-3'.

Analytical ultracentrifugation of recombinant HP1 proteins

Analytical ultracentrifugation (AUC) experiments of full-length HP1β and its isolated chromodomain (CD) and chromoshadow domain (CSD) in approximately physiological buffer was characterized by analytical ultracentrifugation (AUC) with a Beckman Instruments Optima XL-A with absorbance optics at 20 °C as described previously (Fejes Tóth et al, 2005; Kepert et al, 2003). The construct for mouse full-length HP1β as well as its CD (residues 10-80) and CSD (residues 104-185) were kindly provided by Natasha Murzina. Proteins were expressed in *E.coli* BL21 pLysE cells from pET 16d (full-length protein and CSD) or pET 24d (CD) vectors with an N-terminal His-tag. Cleared cell lysates were incubated with 0.5 ml of Ni-NTA resin (Qiagen) per liter of bacterial culture and allowed to bind for at least one hour. After washing the resin with increasing concentrations of imidazole (0-20 mM), the proteins of interest were eluted with 200 mM imidazole in 20 mM Tris-HCl, pH 7.5 supplemented with 100 mM KCl. Protein fractions were pooled and further purified by size-exclusion chromatography.

AUC experiments with full length HP1β and its CD and CSD domains were conducted in a buffer containing 10 mM Tris-HCl, pH 7.5 and 100 mM KCl in the range from 1-30 µM

monomer concentration. Absorbance was recorded at 280 nm or 230 nm. Partial specific volumes $\bar{v}$ as listed in Supplementary Table S3 were calculated with the program Sednterp V1.05 by J. Philo, D. Hayes and T. Laue (Laue et al, 1992). The same program was used to compute buffer densities and viscosities. The sedimentation velocity runs were conducted at 48 000 rpm with 0.003 cm spacing in the continuous scan mode. Data were analyzed with the programs Sedfit 9.4 (Schuck, 2003) and dcdt+, version 1.16 (Philo, 2000). Sedimentation equilibrium experiments were conducted at 10 000, 15 000 and 20 000 rpm using a spacing of 0.001 cm and 10 replicates in the step-wise scan mode. Data were analyzed with the Ultrascan software, version 8.0 (Demeler, 2005). Equilibrium data sets from three different protein loading concentrations at three speeds were used for global curve fitting analysis to a one-component model. To determine the stability of the HP1β dimer the AUC analysis was extended to lower protein concentrations by absorbance detection of the concentration profile at 230 nm. The extinction coefficient at this wavelength was about 6 times higher than at 280 nm with a value of $\sum_{230}$ = 183 000 M^{-1} cm^{-1} so that measurements down to 1 µM could be conducted.

Chromatin immunoprecipitation and ChIP-seq data analysis

ChIP-seq experiments were conducted as described previously (Teif et al, 2012). For each sample, 1 x 10^6 cells were cross-linked with 1 % formaldehyde for 10 minutes and chromatin was rendered accessible using a swelling buffer (25 mM Hepes, pH 7.8, 1 mM $MgCl_2$, 10 mM KCl, 0.1% NP-40, 1 mM DTT). Chromatin was sheared to 220 bp fragments for HP1 and SUV39H and to 150 bp for histone modifications by sonication. After IgG preclearance, the sheared chromatin was incubated with 4 µg of antibody directed against H3K9me3 (Abcam, ab8898), H3K36me3 (Abcam, ab9050), SUV39H1 (Abcam, ab12405), SUV39H2 (Abcam, ab5264) or HP1β (Euromedex, *1MOD-1A9*-AS) and protein G magnetic beads overnight. After washes with sonication buffer (10 mM Tris-HCl, pH 8.0, 200 mM NaCl, 1 mM EDTA, 0.5% N-lauroylsarcosine, 0.1% Na-deoxycholate), high-salt-buffer (50 mM Hepes pH 7.9, 500 mM NaCl, 1mM EDTA, 1% triton X-100, 0.1% Na-deoxycholate, 0.1% SDS), lithium buffer (20 mM Tris-HCl pH 8.0, 1 mM EDTA, 250 mM LiCl, 0.5 % NP-40, 0.5 % Na-deoxycholate) and 10 mM Tris-HCl, chromatin was eluted from magnetic beads and the crosslink was reversed over night at 65 °C. After RNase A and proteinase K digestion, DNA was purified and cloned into a barcoded sequencing library for the Illumina HiSeq2000 sequencing platform (single reads of 50 bp length).

For ChIP-seq data analysis the reads were uniquely mapped with Bowtie without mismatches to the mm9 mouse genome. From 42 intergenic/intronic major gamma satellite (GSAT) repeats annotated in the Repeatmasker software only 16 were uniquely mappable. The read density at these 16 genomic positions was normalized to the total read number and the enrichment was calculated by dividing the read density of ChIP by input samples. To calculate the coverage over the pericentric major satellite repeat consensus sequence (GGA CCT GGA ATA TGG CGA GAA AAC TGA AAA TCA CGG AAA ATG AGA AAT ACA CAC TTT AGG ACG TGA AAT ATG GCG AGG AAA ACT GAA AAA GGT GGA AAA TTT AGA AAT GTC CAC TGT AGG ACG TGG AAT ATG GCA AGA AAA CTG AAA ATC ATG GAA AAT GAG AAA CAT CCA CTT GAC GAC TTG AAA AAT GAC GAA ATC ACT AAA AAA CGT GAA AAA TGA GAA ATG CAC ACT GAA, (Lehnertz et al, 2003)), the repeat sequence was circularized to allow all reads to map to two adjacent repeats. Normalization and enrichment was then calculated as described above. Errors were calculated from two independent ChIP-seq experiments. ChIP-seq data produced in the current study have been deposited in the GEO database (accession number GSE58555).

Confocal laser scanning microscopy (CLSM) and image analysis

For standard confocal imaging a Leica TCS SP5 confocal laser scanning microscope was used as described previously (Müller et al, 2009). 3D image stacks were taken with 0.4 µm sections. For quantitative analysis of protein enrichment and chromatin density in pericentric heterochromatin relative to euchromatin, images were acquired with a Zeiss LSM 710 confocal microscope equipped with a UV-diode and an Argon multi-line laser, a 63x/1.4 NA oil DIC III objective and high sensitivity avalanche photodiode detectors (APD-imaging). Image analysis was conducted with the ImageJ software. Protein enrichment in PCH as defined by DAPI-dense foci was calculated by measuring the mean intensity values in the protein or histone modification channels (either GFP/RFP-tagged or immunofluorescently labeled) in those foci relative to the average intensity measured outside of these regions after correction for background noise. The comparative analysis of H3K9me3 levels in iMEF wt and iMEF *Suv39h* dn cells was conducted by quantitating immunostaining signals in PCH and euchromatin for both cell lines on the same slide. Measured signals were converted to H3K9me3 levels by using the nuclear trimethylation level of 28 ± 2 % in wild-type NIH-3T3 cells determined by mass spectrometry (Fodor et al, 2006) as well as the relative genomic fraction of 3.6 % for major satellite repeats (Waterston et al, 2002). A similar analysis was conducted for the HP1 triple knockdown (TKD) experiments. After maximum intensity

projection, protein expression and methylation levels were analyzed as described above. To estimate knockdown levels, the HP1 intensity of HP1 siRNA-transfected cells was compared to that of mock siRNA-transfected cells and normalized to this value.

2D confocal images of JMJD2C-GFP expressing cells were segmented using binary masks for the nucleus and PCH foci (derived from DAPI images) to yield the per-nucleus-expression of JMJD2C-GFP and the H3K9me3 enrichment in PCH foci. The H3K9me3 immunofluorescence signal was normalized to the DAPI signal and averaged over all pixels belonging to an individual PCH focus. The JMJD2C-GFP expression level was given as the mean JMJD2C-GFP signal of all pixels belonging to an individual nucleus. With these parameters, the H3K9me3 enrichment versus the corresponding JMJD2C-GFP expression level was determined and discretized into 20 equally sized bins of JMJD2C-GFP levels.

Cell cycle states were assigned based on a combination of different markers that included the punctuate PCNA distribution observed during S phase, the localization of HP1 to PCH, which is indicative of G1 or S phase, and the phosphorylation of histone H3 at serine 10, which occurs during G2/M phase. While PCNA and H3S10p were used for fixed samples, the co-transfection of PCNA and/or HP1 was used to identify cell cycle phases in living cells.

Fluorescence recovery after photobleaching (FRAP) and fluorescence (cross-) correlation spectroscopy (FCS/FCCS) data acquisition

For FRAP experiments, images were acquired on a Leica TCS SP5 confocal microscope at 128 x 128 pixels and 1400 Hz scanning speed at a time resolution of 115 ms per image. Typically, 25-50 images were acquired before bleaching twice (i.e. 230 ms) at 100 % laser power. Subsequently, images were acquired for 4 min. The FRAP data analysis is described in the Supplementary Data Analysis section.

FCS and FCCS experiments were conducted with a Zeiss LSM 710 microscope equipped with a 63x/NA 1.2 water immersion objective with correction collar and a ConfoCor3 unit using the program ZEN (Zeiss). GFP and RFP excitation was done with a 488 nm Argon laser line and a 561 nm laser line of a diode-pumped solid-state laser. Emitted signals were recorded through a BP 505-540 IR and a LP 580 filter to separate both channels.

The calibration of the focal volume dimensions was done with an aqueous solution of TetraSpeck beads (Life Technologies). For F(C)CS measurements, confocal images were taken to determine the region for the fluctuation measurements in the cytoplasm, euchromatin and heterochromatin. Concentration fluctuations of fluorescently labeled

molecules were recorded for 60 s and the intensity signal was subjected to a time correlation analysis to obtain auto- or cross-correlation functions. The data analysis is described below.

SUV39H long-range methylation activity upon lamina-recruitment

To test the ability of SUV39H1 to methylate nucleosomes at some spatial distance, we tethered GFP-SUV39H1 or inactive SUV39H1-H324L-GFP (negative control) to the nuclear lamina via a GFP binding protein (GBP) fused to Lamin B1 (GBP-Lamin B1). H3K9me3 levels in iMEF *Suv39h* dn cells were detected by a red fluorescent construct of the HP1 chromodomain (CD-RFP) after transfection with GBP-Lamin B1 and GFP-SUV39H1 or SUV39H1-H324L-GFP. H3K9me3 enrichment at the nuclear lamina was determined by averaging the fluorescence intensity profiles of GFP-tagged SUV39H and CD-RFP from the nuclear boundary towards the nucleus center over the entire nuclear lamina. By fitting these profiles for GFP-SUV39H1 and CD-RFP with an exponential function, the full width at half-maximum was determined, which describes the spatial extension of the newly formed H3K9me3 modification domains.

Measurements of endogenous protein concentrations and calculation of free protein fraction

The concentrations of GFP-tagged SUV39H1, HP1α/β/γ and SUV4-20H proteins in eu- and heterochromatin were measured by FCS in cell lines that stably expressed these proteins as described previously (Müller et al, 2009) (Supplementary Table S1). The ratios between endogenous and GFP-tagged proteins were determined by quantitative analysis of immunoprecipitated protein or cell lysate on Coomassie-stained gels and by western blotting (Supplementary Fig S3 B, C, Supplementary Table S1, Table 1). The corresponding concentrations for SUV4-20H were derived from FCS measurements in ESCs with a GFP knock-in at the C-terminus of the endogenous genes. Since SUV4-20H concentrations do not change significantly during differentiation of ESCs (Efroni et al, 2008), these concentrations were used here also for fibroblasts. The concentrations of SUV39H2, MECP2 and MBD1 were estimated from RNA expression levels determined by RNA-seq in MEFs. In these cells a SUV39H1 to SUV39H2 transcript ratio of 3.4 : 1 was determined, the transcript ratio of SUV39H1 to MECP2 was 0.34 : 1 and that of SUV39H1 to MBD1 was 1.36 : 1.

Based on the endogenous protein concentration the free protein concentration of HP1 and SUV39H was calculated as follows: The diffusion coefficient measured with FCS reflects

both freely diffusive and transiently bound proteins. The (effective) diffusion coefficient measured in euchromatin was smaller due to chromatin-binding interactions compared to the diffusion coefficient of free protein measured in the cytoplasm. The ratio between both values is $D_{\mathrm{FCS,Eu}}/D_{\mathrm{FCS,Cyto}} = 1/\left(1+k_{\mathrm{on}}^{*}/k_{\mathrm{off}}\right)$ (Sprague et al, 2004) with pseudo-association rate k_{on}^{*} and dissociation rate k_{off}. Accordingly, the free protein fraction f_{free} was calculated from $f_{\mathrm{free}} = k_{\mathrm{off}}/\left(k_{\mathrm{on}}^{*}+k_{\mathrm{off}}\right) = 1/\left(1+k_{\mathrm{on}}^{*}/k_{\mathrm{off}}\right)$. The free protein concentration c_{free} was then obtained by multiplying f_{free} with the concentration of the total mobile protein pool that contributes to the effective diffusion coefficient measured by FCS. In euchromatin this protein fraction was represented by binding site classes I and II for HP1 and by class I for SUV39H (see Table 1 and Supplementary Data Analysis "Fluorescence recovery after photobleaching" below).

Protein-protein interaction analysis via the fluorescent two-hybrid (F2H) assay

The interaction of HP1 dimers with SUV39H could not be measured reliably by FCCS due to the large difference between SUV39H1 and HP1 concentrations that leads to a high background from the HP1 signal. Furthermore, SUV39H1 proteins were bound to chromatin with high affinity and thus were subject to fluorescence photobleaching, rendering them unsuitable for FCCS experiments. Accordingly, we applied the fluorescent two-hybrid assay (F2H) to study interactions of HP1, SUV39H1, MECP2 and MBD1 in living cells. The GFP-labeled protein was tethered to integration sites of *lac* operator (*lac*O) repeats referred to as a *lac*O-array in a U2OS cell line (F6B2) via a bacterial LacI repressor fused to a GFP-binding protein (LacI-GBP) as described previously (Chung et al, 2011; Rothbauer et al, 2006; Zolghadr et al, 2008). For the interaction analysis 3D image stacks spaced 0.25 µm along the z-axis were recorded. Maximum intensity projections of these stacks were then analyzed for recruitment of the GFP-tagged protein to the *lac*O-arrays and colocalization of the RFP-labeled interaction partner at these foci (Fig 2C, Supplementary Fig S5B). Spots were counted as positive for colocalization if the background-corrected RFP-signal at the *lac*O-arrays was at least 1.7-fold above the average nuclear intensity level. This type of analysis was conducted for the dimerization of SUV39H1 (SUV39H1-GFP, SUV39H1-RFP) and to evaluate the interactions of MBD-proteins (MBD1 and MECP2) with HP1 or SUV39H.

Supplementary Data Analysis

Fluorescence recovery after photobleaching

FRAP analysis was carried out with the software FREDIS (Müller et al, 2009) by fitting the time evolution of the intensity integrated over an effective 1.9 µm bleach spot (1.5 µm bleaching diameter plus 0.4 µm broadening due to fast diffusion processes occurring during the bleach) either to a diffusion model, to a reaction model or to a reaction-diffusion model that incorporates both diffusion and binding processes based on the theoretical framework by (Sprague et al, 2004). To select the best fit model for each FRAP curve, the F-ratio was calculated that accounts for the relative change in the sum of residuals and the relative change in degrees of freedom of two different models. In general, the reaction-diffusion model gave the best results except for HP1 and SUV4-20H in euchromatin that were described best by an effective diffusion model. This model is appropriate if either no binding sites or binding sites with very high dissociation rates are present. The latter results in an effective diffusion coefficient D_{eff} and a parameter f_{im} that describes the fraction of proteins immobilized during the measurement. The reaction-diffusion model describes the recovery in the presence of a high affinity binding site characterized by the dissociation constant k_{off}, the equilibrium constant K^*_{eq} and the fraction of transiently bound molecules. The diffusion coefficients obtained in the nucleus were significantly smaller than the free diffusion coefficient measured by FCS (see below) in the cytoplasm. Since free diffusion is expected to be similar in the cytoplasm and the nucleus (Pack et al, 2006), the reduced diffusion coefficient extracted from both diffusion and reaction-diffusion model can be explained by transient chromatin interaction that cannot be resolved and thus reflects low affinity binding referred to here as class I binding sites. Due to the 115 ms time resolution of a single image frame, the residence time at class I sites can be estimated to be ≤ 0.5 s. The immobile fraction extracted from both fit models depicts the highest affinity binding sites and was identified as binding class IV. Binding classes II and III were extracted from reaction-diffusion fits. In addition, we compared mobility parameters in euchromatin and PCH for a given protein to determine the minimal number of binding site classes that described our experimental data in a consistent manner. For example, we observed that the kinetic off-rate of SUV39H1 in PCH from the reaction-diffusion fit was more than three-fold lower than in euchromatin. Accordingly, we interpreted the heterochromatic off-rate as an average value for the interaction with both euchromatin and PCH binding sites and recalculated the data with a reaction-diffusion model with two binding states. Based on the assumption that the bound fraction and the residence time (k_{off}^{-1}) are the weighted averages of the bound

fractions/residence times of class II and class III, the kinetic rate constants for class II and class III are given by

$$k_{\text{off.III}} = \frac{k_{\text{off,eff}} k_{\text{off.II}} \left(k_{\text{on,eff}} k_{\text{off,II}} - k_{\text{on,II}} k_{\text{off,eff}} \right)}{k_{\text{on,eff}} k_{\text{off,II}}^2 - k_{\text{on,II}} k_{\text{off,eff}}^2}$$

$$k_{\text{on,III}} = \frac{\left(k_{\text{on,eff}} k_{\text{off,II}} - k_{\text{on,II}} k_{\text{off,eff}} \right)^2}{k_{\text{on,eff}} k_{\text{off,II}}^2 - k_{\text{on,II}} k_{\text{off,eff}}^2}$$

(1)

Since class II was assigned to the binding reaction in euchromatin, the rates $k_{\text{on,III}}$ and $k_{\text{off,III}}$ were obtained based on the euchromatic values $k_{\text{on,II}} / k_{\text{off,II}}$ and the average heterochromatic values $k_{\text{on,eff}} / k_{\text{off,eff}}$.

For HP1 in euchromatin the diffusion model was applied but resulted in a very small effective diffusion coefficient. Thus, we concluded that the low affinity binding sites identified in PCH with a reaction-diffusion model fit were also present in euchromatin but at a lower concentration. Accordingly, we refitted the recovery curves with a reaction-diffusion model and fixed k_{off} at the value that was measured in heterochromatin.

Fluorescence correlation spectroscopy

Data analysis including calculation of the autocorrelation function (ACF) was conducted with a half-automated self-written FCS analysis software tool termed Spatiotemporal Correlation Suite (STCor). STCor reads the Zeiss fluctuation raw data files (*.raw) and calculates the autocorrelation function according to the formalism described in our previous work (Müller et al, 2009). The ACFs were fit to an anomalous diffusion model with one (cytoplasm) or two (eu-/heterochromatin) components. Protein concentrations were calculated in STCor from the particle number within the focal volume obtained from the fit. The (effective) diffusion coefficients were calculated from the measured diffusion times compared to the diffusion time and the diffusion coefficient of Tetraspeck beads (Muller et al, 2008). The anomaly parameter characterizing the nonlinear time dependence of the mean squared particle displacement was obtained for both fractions and typically was > 1 for the second fraction. Since this is indicative of confined diffusion behavior and typically observed for proteins that interact transiently with chromatin in FCS measurements, the second component reflects chromatin translocations that can be observed as slow intensity fluctuations of chromatin-bound fluorescently labeled molecules (Erdel et al, 2011; Erdel et al, 2010; Müller et al, 2009).

Fluorescence cross-correlation spectroscopy

The interaction of GFP- and RFP-tagged proteins in NIH-3T3 cells was measured by fluorescence cross-correlation spectroscopy with a Zeiss LSM 710 ConfoCor3 as described above. The presence of endogenous unlabeled protein as well as complexes containing only particles labeled with one color (e.g. (HP1)$_2$, (GFP-HP1)$_2$ or (RFP-HP1)$_2$) reduces the FCCS signal. Thus, the fraction of the total amount of proteins incorporated into a multimeric complex was calculated from the amplitudes of the auto- (ACF) and cross-correlation functions (XCF). For this analysis, spectral crosstalk was corrected according to

$$G_{\text{green}}(\tau) = G_{\text{green}}^*(\tau)$$

$$G_{\text{red}}(\tau) = \frac{1}{(1-\gamma)^2}\left(G_{\text{red}}^*(\tau) - 2\gamma G_{\text{cross}}^*(\tau) + \gamma^2 G_{\text{green}}^*(\tau)\right) \qquad (2)$$

$$G_{\text{cross}}(\tau) = \frac{1}{1-\gamma}\left(G_{\text{cross}}^*(\tau) - \gamma G_{\text{green}}^*(\tau)\right)$$

Here, G_i^* are the measured correlation functions including crosstalk and G_i are the corrected correlation functions. Further, $\gamma = \kappa \langle I_g \rangle \langle I_r \rangle^{-1}$ with κ being the brightness of the green fluorophore (GFP) in the red channel divided by its brightness in the green channel, and $\langle I_g \rangle$ and $\langle I_r \rangle$ representing the average intensity in the green and red channel, respectively. A similar crosstalk correction was reported recently by (Bacia et al, 2012). To measure the brightness of GFP in the red channel, cells were transfected with inert GFP protein and a standard measurement was conducted with both lasers and detection in both the red and the green channel. Data fitting of the crosstalk corrected functions was done as described previously (Erdel et al, 2010; Müller et al, 2009) using the STCor software.

The degree of cross-correlation, *ratioG*, i.e. the fraction of double-labeled molecules normalized to the number of molecules of each 'color' was calculated according to

$$ratio\, G = \frac{G_{\text{cross}}(0)}{G_{\text{green}}(0) \cdot G_{\text{red}}(0)} . \qquad (3)$$

Here, $G_{\text{cross}}(0)$ denotes the amplitude of the cross-correlation function and $G_{\text{green}}(0)$ and $G_{\text{red}}(0)$ denote the amplitudes of the autocorrelation function in the green and the red channel at lag time $\tau = 0$, respectively. The fraction of monomeric protein Θ that is incorporated into a homodimeric complex is related to *ratio G* via

$$ratioG = \Theta \sqrt{\frac{\lambda_g \lambda_r}{(1 + \lambda_g \Theta)(1 + \lambda_r \Theta)}} \qquad (4)$$

Here, λ_g and λ_r are the label degrees for the green and red species, respectively. This result is obtained by using the definition of the correlation function for partially labeled pools (Erdel et al, 2010; Weidemann et al, 2002). This relation can be inverted to obtain the fraction of proteins in dimeric complexes based on the label degrees and *ratio G*:

$$\Theta = \sqrt{\frac{\left(\lambda_g + \lambda_r\right)^2 ratioG^4}{4\lambda_g^2\lambda_r^2\left(ratioG^2 - 1\right)^2} - \frac{ratioG^2}{\lambda_g\lambda_r\left(ratioG^2 - 1\right)}} - \frac{\left(\lambda_g + \lambda_r\right)ratioG^2}{2\lambda_g\lambda_r\left(ratioG^2 - 1\right)} \tag{5}$$

Estimates of kinetic association rate and equilibrium dissociation constants for SUV39H and HP1

Dissociation constants for the independent binding of SUV39H and HP1 can be estimated from FRAP data as follows: The pseudo-affinity $K_{eq}^* = k_{on}^*/k_{off} = k_{on}c_s/k_{off} \approx 5.1$ for HP1 was derived from the FRAP fit curves (Supplementary Table S2). Since binding to trimethylated H3K9 residues is the main chromatin interaction of HP1 in the nucleus (Müller et al, 2009), the substrate concentration c_s in the above equation can be approximated with the concentration of trimethylated nucleosomes, which equals roughly 100 µM in heterochromatin (Fodor et al, 2006; Wachsmuth et al, 2008). Based on these values the association rate for HP1 was calculated according to $k_{on} = K_{eq,HP1}^* k_{off,HP1}/c_s \approx 1.8 \cdot 10^4 M^{-1}s^{-1}$. This corresponds well to association rates measured for other nuclear proteins (Phillip et al, 2012). The dissociation constant for HP1 is $K_{d,HP1} = k_{off,HP1}/k_{on} = c_s/K_{eq,HP1}^* \approx 20\mu M$. This rather low affinity reflects the transient binding behavior observed for the majority of HP1 molecules. As shown by FCS measurements in the cytosol, the free diffusion coefficients of HP1 and SUV39H are similar (Supplementary Table S1), suggesting that their (diffusion-limited) association rate can be approximated with the same value (Berg & von Hippel, 1985). Accordingly, the dissociation constant for transient SUV39H binding was estimated from the dissociation rate determined by FRAP in heterochromatin (Supplementary Table S2) to be $K_{d,SUV39H} = k_{off,SUV39H}/k_{on} \approx 3.5\mu M$. Thus, individual HP1 and SUV39H molecules bind relatively weakly to chromatin. However, due to their interaction, the affinity of the HP1-SUV39H complex to chromatin is much higher. Assuming that the individual chromatin binding contributions in the HP1-SUV39H complex are additive with binding energies ΔG_{HP1} for HP1 and ΔG_{SUV39H} for SUV39H1 one obtains $\Delta G_{HP1-SUV39H} = \Delta G_{HP1} + \Delta G_{SUV39}$, which corresponds to $K_{d,HP1-SUV39H} = \exp\left(-\left(\Delta G_{HP1} + \Delta G_{SUV39H}\right)/RT\right) \approx 0.07nM$ for the HP1-SUV39H

complex (with $\Delta G_{HP1} \approx 27$ kJ/mol and $\Delta G_{SUV39H} \approx 31$ kJ/mol). Since HP1 and SUV39H interact with each other in a dynamic equilibrium, this K_d value can be considered to represent a lower limit.

Calculation of H3K9me3 levels

To estimate the relative methylation rates in eu- and heterochromatin we used a simplified description in which the nucleosomes can adopt an unmodified state (U), a methylated state (M) and also an 'anti-modified' state, i.e. carrying the opposing acetylation modification (A):

$$A \underset{k_a}{\overset{k_{-a}}{\rightleftharpoons}} U \underset{k_{-m}}{\overset{k_m}{\rightleftharpoons}} M$$
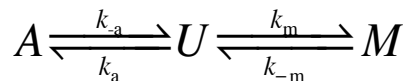
This model in steady-state is described by the following equations:

$$\frac{\partial M}{\partial t} = U \cdot k_m - M \cdot k_{-m} = 0$$

$$\frac{\partial A}{\partial t} = U \cdot k_a - A \cdot k_{-a} = 0 \tag{6}$$

$$\frac{\partial U}{\partial t} = M \cdot k_{-m} + A \cdot k_{-a} - U \cdot (k_a + k_m) = 0$$

With the normalization $M + A + U = 1$, the steady-state methylation level for this system is given by

$$M(K, r) = \frac{r}{1 + K + r} \tag{7}$$

with the rate ratios $K = k_a / k_{-a}$ and $r = k_m / k_{-m}$. Using the relative H3K9me3 levels determined by immunostaining (Supplementary Fig S2B, Fig 3C), the following relations for the rate constants are obtained:

$$r_{Eu,wt} = \left(\frac{k_m}{k_{-m}} \right)_{Eu,wt} = \frac{M(1+K)}{1-M} \qquad r_{Eu,KO} = \left(\frac{k_m}{k_{-m}} \right)_{Eu,KO} = \frac{M c_2 (1+K)}{1 - M c_2}$$

$$r_{Het,wt} = \left(\frac{k_m}{k_{-m}} \right)_{PCH,wt} = \frac{M c_1 (1+K)}{1 - M c_1} \quad r_{PCH,KO} = \left(\frac{k_m}{k_{-m}} \right)_{PCH,KO} = \frac{M c_3 (1+K)}{1 - M c_3} \tag{8}$$

Here, k_m and k_{-m} are the methylation and demethylation rates for eu-/heterochromatin in the respective cell line, $M = 28$ % is the methylation level in wild-type euchromatin (Fodor et al, 2006), and c_1 - c_3 are the methylation levels of heterochromatin in wild-type cells ($c_1 = 1.4$), euchromatin in *Suv39h* dn cells ($0.75 < c_2 < 1$) and heterochromatin in *Suv39h* dn cells ($c_3 = 0.5$) relative to the methylation level of wild-type euchromatin (M), respectively. Since both SETDB1/G9A and SUV39H are known to catalyze H3K9me3, the methylation rate can be split up into the contributions from these two enzymes: $k_{m,x} = k_{SETDB1/G9A,x} + k_{SUV39H,x}$. Since

both methylases are differentially regulated in eu-/heterochromatin, individual rate constants were assigned for the different chromatin types. In *Suv39h* dn cells, the SUV39H rates are zero, i.e. $k_{\text{SUV39H,Eu,KO}} = k_{\text{SUV39H,Het,KO}} = 0$. Thus, the rates of the two enzymes are related to the expression in equation (8) by

$$\left(\frac{k_{\text{SETDB1/G9A}}}{k_{\text{-m}}}\right)_{\text{Eu}} = r_{\text{Eu,KO}} = \frac{M c_2 (1+K)}{1 - M c_2} \qquad \left(\frac{k_{\text{SUV39H}}}{k_{\text{-m}}}\right)_{\text{Eu}} = r_{\text{Eu,wt}} - r_{\text{Eu,KO}} = \frac{M(1+K)(1-c_2)}{(1-M)(1-M c_2)}$$

$$\left(\frac{k_{\text{SETDB1/G9A}}}{k_{\text{-m}}}\right)_{\text{PCH}} = r_{\text{PCH,KO}} = \frac{M c_3 (1+K)}{1 - M c_3} \qquad \left(\frac{k_{\text{SUV39H}}}{k_{\text{-m}}}\right)_{\text{PCH}} = r_{\text{PCH,wt}} - r_{\text{PCH,KO}} = \frac{M(1+K)(c_1 - c_3)}{(1 - M c_1)(1 - M c_3)}$$

$$(9)$$

The steady-state methylation levels observed by immunostaining in Fig 3C can be explained by the model given above with the values for the relative methylation rates in equations (8) and (9). For simplicity, the acetylation state was not taken into account, i.e. $k_a = 0$. This seems to be justified since less than 13% of the nucleosomes are acetylated (Fodor et al, 2006). The specificity of both methylases is reflected by the ratio of their rate constants in euchromatin and PCH, which is independent of K and amounts to

$$\frac{k_{\text{SUV39H,PCH}}}{k_{\text{SUV39H,Eu}}} = \frac{(1 - M c_2)(1 - M)(c_1 - c_3)}{(1 - c_2)(1 - M c_1)(1 - M c_3)} > 3.8, \qquad \frac{k_{\text{SETDB1/G9A,Eu}}}{k_{\text{SETDB1/G9A,PCH}}} = \frac{c_2 (1 - M c_3)}{c_3 (1 - M c_2)} > 1.8 \qquad (10)$$

As expected, SUV39H has a preference for PCH and SETDB1/G9A for euchromatin, respectively. The methylation rate of SUV39H is at least 4-fold increased in PCH and the methylation rate of G9A/SETDB1 is roughly 2-fold increased in euchromatin for the error range of our experiment ($0.75 < c_2 < 1$). For the average value $c_2 = 0.9$ an 8-fold increased methylation rate of SUV39H in PCH is obtained.

Mathematical modeling of the pericentric heterochromatin network

A chromatin fiber of 300 nucleosomes arranged on a linear 60 kb DNA fragment was modeled with a nucleosome repeat length of 200 bp. Each nucleosome on the fiber was able to contact the others via chromatin looping. The collision probability was determined as the local concentration of one nucleosome in the proximity of the others as described previously (Erdel et al, 2013; Rippe, 2001; Rippe et al, 1995). The resulting values for an increased local concentration of nucleosomes in the proximity of the first nucleosome at the 0-position due to chromatin looping is plotted in Fig 7A.

To represent the PCH state, we replaced every 8th nucleosome of the uniform euchromatic fiber by a high affinity binding site, referred to as an 'origin' (parameter '*o*' in the model). The total number of origins was determined by the model based on SUV39H concentration and the experimentally-derived association and dissociation rates of SUV39H (Supplementary Tables S2, S7) to yield 38 origins in a chain of 300 nucleosomes for the modeling work. The number of nucleation sites as represented by SUV39H-bound origins ('*SHo*') was determined from the amount of immobilized SUV39H compared to the nucleosome concentration in PCH. We computed that every 170th nucleosome or every 21st origin site was in a nucleation site state. For euchromatin the corresponding calculations yielded an origin site every 71 nucleosomes.

The mathematical model consists of a system of ordinary differential equations (ODEs) as shown below (equation 11). The core variables constituting the network (Fig 7B) are the local probability of methylation and the local probabilities of occupation by HP1, SUV39H and HP1-SUV39H complex that depend on time and the position of nucleosomes and nucleation origins on the fiber. The measured parameters for the three different HP1α/β/γ isoforms as well as for the SUV39H1 and SUV39H2 were integrated into a single 'virtual' HP1 or SUV39H protein, respectively. The model variables and parameters as well as reference values are given in Supplementary Table S7. The index *i* denotes the position of an individual nucleosome on the fiber. Nucleation origins positioned within the fiber were described by the first three equations. Their state transitions do not depend on the states of the adjacent nucleosomes and their position on the fiber.

$$\frac{do}{dt} = k_{-h2}Ho + k_{-s3}So - k_{+}(c_s + c_h)o$$

$$\frac{dSo}{dt} = k_{+}c_s o + k_{-h4}(1 - o - So - Ho) - (k_{+}c_h + k_{-s3})So$$

$$\frac{dHo}{dt} = k_{+}c_h o + k_{-s4}(1 - o - So - Ho) - (k_{+}c_s + k_{-h2})Ho$$

$$\frac{dn_i}{dt} = k_{-m}(1 - n_i - Sm_i - Hm_i - SHm_i) - n_i\left[k_u + k_m(c_s + \sum_{l=0}^{299}(SHm_l + Sm_l)j_m(|i - l|) + (SHo + So)\sum_{k=0}^{37}j_m(|i - 8k|))\right]$$

$$\frac{dHm_i}{dt} = k_{+}c_h(1 - n_i - Sm_i - Hm_i - SHm_i) + k_{-s2}SHm_i - (k_{+}c_s + k_{-h2})Hm_i$$

$$\frac{dSm_i}{dt} = k_{+}c_s(1 - n_i - Sm_i - Hm_i - SHm_i) + k_{-h2}SHm_i - (k_{+}c_h + k_{-s1})Sm_i$$

$$\frac{dSHm_i}{dt} = k_{+}c_s Hm_i + k_{+}c_h Sm_i - (k_{-s2} + k_{-h2})SHm_i$$

(11)

For euchromatin, nucleation origins were neglected due to their low abundance. Thus, the equations for euchromatin read:

$$\frac{dn_i}{dt} = k_{-m}(1 - n_i - Sm_i - Hm_i - SHm_i) - n_i \left[k_u + k_e + k_m \left(c_s + \sum_{l=0}^{299} (SHm_l + Sm_l) j_m(|i - l|) \right) \right]$$

$$\frac{dHm_i}{dt} = k_+ c_h (1 - n_i - Sm_i - Hm_i - SHm_i) + k_{-s2} SHm_i - (k_+ c_s + k_{-h2}) Hm_i$$

$$\frac{dSm_i}{dt} = k_+ c_s (1 - n_i - Sm_i - Hm_i - SHm_i) + k_{-h2} SHm_i - (k_+ c_h + k_{-s1}) Sm_i$$

$$\frac{dSHm_i}{dt} = k_+ c_s Hm_i + k_+ c_h Sm_i - (k_{-s2} + k_{-h2}) SHm_i$$

(12)

The steady state solutions for the PCH and euchromatin fiber systems as functions of HP1, JMJD2 and number of origins were numerically derived using Mathematica 9.0 (Wolfram Research). The Mathematica code of the model is provided as Supplementary Material. Following the chemical master equation formalism we converted the deterministic model into the corresponding stochastic model. Stochastic kinetic traces and steady state distributions were simulated with the Gillespie stochastic simulation algorithm (Gillespie, 2007) implemented in C++. Based on our experimental data set and quantities available from the literature data some model parameters were directly calculated and fixed (Supplementary Table S7). The remaining non-constrained parameters k_u, k_m and k_e were determined from the experimentally measured PCH and euchromatin steady state H3K9me3 levels. The resulting parameter set quantitatively reproduced the H3K9me3 levels in wild-type PCH (38 %) and in *Suv39h* double knockout PCH (13 %) as well as in wild-type euchromatin (28 %) (Fig 3C). The modeled methylation degree included the summation over all nucleosomes within the chromatin fiber in the methylated state (*m, Hm, Sm, SHm*):

$$M = \frac{100 \sum_{l=0}^{299} (1 - n_l)}{300 - Number\ (origins)}.$$

(13)

Supplementary Tables

Supplementary Table S1. FCS analysis of HP1α, HP1β, HP1γ and SUV39H1.

Protein Cell lines	Compart-ment	n	$c_{GFP-protein}$ (µM)	$c_{endog.protein}$ (µM)	D_1 (µm² s⁻¹)	α_1	D_2 (µm² s⁻¹)	α_2	$\Sigma c_{endogenous}$ (µM)
GFP-**HP1α** [a] NIH-3T3	Cyto [b]	11	0.24 ± 0.04	0.06 ± 0.04	42.1 ± 4.3 [d]	0.83 ± 0.05 [d]	–	–	Cyto [e]: 0.5 ± 0.2 Eu [e]: 18.8 ± 11.9 PCH [e]: 40.8 ± 25.2
	Eu [c]	19	1.5 ± 0.3	0.5 ± 0.3	13.9 ± 1.4 [d]	0.81 ± 0.04 [d]	0.38 ± 0.07 [d]	> 1 [d]	
	PCH	18	2.2 ± 0.5	1.0 ± 0.7	7.0 ± 1.6 [d]	0.88 ± 0.12 [d]	0.09 ± 0.04 [d]	> 1 [d]	
GFP-**HP1β** [a] NIH-3T3	Cyto [b]	10	0.13 ± 0.06	0.14 ± 0.09	43.7 ± 10.1 [d]	0.74 ± 0.05 [d]	–	–	
	Eu [c]	19	1.45 ± 0.31	3.7 ± 2.9	5.8 ± 1.4 [d]	0.79 ± 0.06 [d]	0.13 ± 0.04 [d]	> 1 [d]	
	PCH	12	2.0 ± 0.9	11.2 ± 8.7	6.7 ± 1.1 [d]	0.83 ± 0.08 [d]	0.07 ± 0.02 [d]	> 1 [d]	
GFP-**HP1γ** [a] NIH-3T3	Cyto [b]	68	0.15 ± 0.03	0.27 + 0.13	51.7 ± 4.1	0.65 ± 0.02	–	–	
	Eu [c]	53	1.8 ± 0.2	14.7 ± 11.5	6.0 ± 1.1	0.63 ± 0.01	0.11 ± 0.03	> 1	
	PCH	22	3.6 ± 0.7	28.6 ± 23.6	4.9 ± 2.2	0.66 ± 0.05	0.05 ± 0.02	> 1	
SUV39H1-GFP NIH-3T3	Cyto [b]	34	0.04 ± 0.01	0. 35 ± 0.01	25.5 ± 5.2	0.70 ± 0.02	–	–	0. 35 ± 0.01
	Eu [c]	21	0.69 ± 0.27	0.42 ± 0.22	17.6 ± 7.6	0.71 ± 0.08	0.13 ± 0.05	> 1	0.42 ± 0.22
	PCH	6	1.45 ± 0.65	3.0 ± 1.7	18.2 ± 9.0	0.65 ± 0.20	0.02 ± 0.01	> 1	3.0 ± 1.7

FCS autocorrelation functions (ACF) of GFP-labeled HP1 or SUV39H1 were analyzed with an anomalous diffusion model to derive averaged parameters from the indicated number of experiments n. This yielded diffusion coefficients D, anomaly parameters α and the concentration of GFP-tagged protein $c_{GFP-Protein}$. Endogenous SUV39H1 concentrations were determined from the ratio of SUV39H1-GFP and endogenous SUV39H1 measured by quantitative SDS-PAGE with Coomassie-staining, yielding a 0.75 ± 0.03-fold expression of SUV39H1-GFP as compared to endogenous SUV39H1. The endogenous HP1 concentrations were calculated from the ratio GFP-HP1 to endogenous HP1 measured on quantitative western blots. A 4.2 ± 0.3-fold overexpression of GFP-HP1α, a 0.92 ± 0.4-fold expression for GFP-HP1β and a 0.55 ± 0.22-fold expression of GFP-HP1γ as compared to endogenous HP1α/β/γwas determined. From the value of $c_{SUV39H1-GFP}$ or $c_{GFP-HP1}$ measured in the

cytoplasm absolute concentrations in this cellular compartment were obtained. The concentration ratios of PCH and euchromatin were derived from the fluorescence intensities of the respective proteins measured in the cytoplasm, euchromatin and PCH by quantitative APD imaging. Errors correspond to 95 % confidence intervals.

[a] NIH-3T3 GFP-HP1α/β/γ cell lines stably expressing GFP-tagged HP1 isoforms.

[b] The data for HP1/SUV39H1 in the cytoplasm were fit with a one-component anomalous diffusion model.

[c] A two-component anomalous diffusion model was required to fit the ACF of measurements within euchromatin and PCH. The faster-moving fraction with diffusion constant D_1 displayed subdiffusion behavior ($\alpha < 1$), as expected for transient binding and/or diffusion in the presence of obstacles. For the second fraction, intensity fluctuations originating from chromatin-bound molecules moving together with chromatin were very slow and displayed anomaly parameters $\alpha > 1$ (Müller et al, 2009).

[d] FCS measurements of HP1α and HP1β were published previously in (Müller et al, 2009). In the latter study, we used Alexa 488 maleimide with a too low literature value of $D = 210$ µm^2·s^{-1} as a reference. From calibration measurements with well-defined Tetraspeck beads (Muller et al, 2008), we conclude that our previous FCS analysis of HP1α/β underestimated the diffusion coefficients by a factor of roughly 1.8. Additional measurements were conducted for concentration determination.

[e] The amount of all HP1 isoforms within cytoplasm, euchromatin or heterochromatin was summed up to yield the concentration of the total pool of HP1 in the three different cellular compartments.

Supplementary Table S2. FRAP analysis of GFP-tagged proteins.

Protein Cell line	Chromatin	n	D_{eff} ($\mu m^2\ s^{-1}$)	$k_{off}\ (s^{-1})$	$k^*_{on}\ (s^{-1})$	K_{aff}	Free (%)	Bound (%)	f_{im} (%)
GFP-**HP1α** [a, b]	Eu	74	0.18 ± 0.02	–	–	–	98 ± 1	–	2 ± 1
NIH-3T3	PCH	59	0.9 ± 0.3	0.26 ± 0.06	0.7 ± 0.2	3.1 ± 1.2	24 ± 2	70 ± 2	6 ± 2
GFP-**HP1β** [a, b]	Eu	10	0.15 ± 0.04	–	–	–	97 ± 2	–	3 ± 2
NIH-3T3	PCH	8	0.4 ± 0.3	0.27 ± 0.17	1.7 ± 2.3	4.5 ± 2.4	19 ± 7	73 ± 7	8 ± 6
GFP-**HP1β** [c] iMEF *Suv39h* dn	Eu/PCH	21	0.4 ± 0.1	–	–	–	99 ± 1	–	3 ± 3
HP1β-GFP [a]	Eu	28	0.03 ± 0.003	–	–	–	94 ± 1	–	6 ± 1
iMEF wt	PCH	25	0.09 ± 0.01	0.044 ± 0.003	0.35 ± 0.05	6.9 ± 0.7	13 ± 1	76 ± 2	11 ± 1
HP1β-GFP [d]	Eu	10	0.05 ± 0.01	–	–	–	93 ± 1	–	7 ± 1
iMEF *Suv4-20h* dn	PCH	24	0.14 ± 0.02	0.08 ± 0.01	0.52 ± 0.11	6.2 ± 0.9	15 ± 1	79 ± 2	6 ± 1
GFP-**HP1γ** [a, b]	Eu	13	0.19 ± 0.04	–	–	–	98 ± 2	–	2 ± 2
NIH-3T3	PCH	13	0.5 ± 0.2	0.5 ± 0.2	2.8 ± 2.1	4.9 ± 2.3	20 ± 7	74 ± 7	6 ± 4
JMJD2C-GFP [e]	Eu	9	0.6 ± 0.3	–	–	–	98 ± 2	–	2 ± 2
NIH-3T3	PCH	7	0.4 ± 0.1	–	–	–	97 ± 3	–	3 ± 3
MBD1-GFP [a]	Eu	10	0.05 ± 0.01	–	–	–	93 ± 4	–	7 ± 4
NIH-3T3	PCH	13	0.07 ± 0.04	0.02 ± 0.01	0.07 ± 0.03	2.8 ± 0.5	24 ± 3	66 ± 5	10 ± 5
GFP-**MECP2** [a]	Eu	14	0.05 ± 0.01	–	–	–	98 ± 2	–	2 ± 2
NIH-3T3	PCH	14	0.2 ± 0.1	0.04 ± 0.02	0.2 ± 0.1	4.0 ± 0.7	17 ± 3	65 ± 8	18 ± 9
PAX3-GFP [e]	Eu	15	0.5 ± 0.2	–	–	–	98 ± 4	–	2 ± 4
NIH-3T3	PCH	19	0.7 ± 0.3	–	–	–	98 ± 3	–	2 ± 3

SUV39H1-GFP	Eu	53	0.5 ± 0.3	0.19 ± 0.1	0.5 ± 0.4	2.1 ± 0.3	32 ± 3	65 ± 3	3 ± 1
NIH-3T3	PCH	52	0.3 ± 0.1	0.06 ± 0.02	0.3 ± 0.1	4.0 ± 0.8	18 ± 3	62 ± 3	20 ± 5
SUV39H1-GFP [f]	Eu	10	0.4 ± 0.2	0.2 ± 0.1	0.5 ± 0.3	2.6 ± 0.4	29 ± 4	71 ± 3	0 ± 1
iMEF *Suv39h* dn	PCH	7	0.2 ± 0.1	0.13 ± 0.03	0.32 ± 0.05	2.6 ± 0.3	27 ± 2	70 ± 1	4 ± 3
SUV39H1-H320R-GFP [g]	Eu	6	1.8 ± 1.4	0.2 ± 0.2	0.41 ± 0.28	2.3 ± 0.7	30 ± 6	66 ± 6	4 ± 5
NIH-3T3	PCH	8	0.2 ± 0.1	0.03 ± 0.01	0.14 ± 0.09	3.4 ± 1.6	20 ± 6	55 ± 6	25 ± 8
SUV39H1-H324L-GFP [g]	Eu	12	0.5 ± 0.5	0.14 ± 0.17	0.16 ± 0.11	2.5 ± 0.8	29 ± 6	68 ± 6	3 ± 3
NIH-3T3	PCH	8	0.04 ± 0.02	0.03 ± 0.02	0.13 ± 0.16	4.8 ± 5.4	27 ± 8	67 ± 8	6 ± 3
SUV39H2-GFP	Eu	8	0.013 ± 0.008	0.004 ± 0.002	0.01 ± 0.01	2.3 ± 0.8	23 ± 6	52 ± 6	24 ± 13
NIH-3T3	PCH	28	0.014 ± 0.007	0.007 ± 0.002	0.04 ± 0.01	5.2 ± 1.3	9 ± 1	39 ± 1	52 ± 13
SUV4-20H1-GFP [a]	Eu	10	0.11 ± 0.05	–	–	–	85 ± 2	–	15 ± 8
iMEF	PCH	29	0.08 ± 0.04	0.04 ± 0.01	0.20 ± 0.11	4.1 ± 1.0	15 ± 2	54 ± 2	30 ± 5
SUV4-20H2-GFP [a]	Eu	8	0.13 ± 0.10	–	–	–	92 ± 1	–	17 ± 11
iMEF	PCH	23	0.011 ± 0.005	0.010 ± 0.004	0.05 ± 0.04	4.4 ± 1.1	8 ± 1	33 ± 1	59 ± 12

Fluorescence recovery after photobleaching (FRAP) measurements were fit with a diffusion, a reaction-diffusion and a reaction model. Parameters are given for the model that yielded the best fit. All measurements were performed in G1 and S phase cells and averaged over *n* experiments. Errors correspond to 95 % confidence intervals.

[a] The mobility of MBD1, MECP2, SUV4-20H1/2-GFP and all isoforms of HP1-GFP in euchromatin of wild-type fibroblasts was very well described by a diffusion model. The effective diffusion coefficient D_{eff} includes low affinity/transient binding contributions. For PCH a reaction-diffusion model was required to describe the data for these proteins that additionally yielded the binding rate constants listed in the table. All other measurements were fit with a reaction-diffusion model.

[b] NIH-3T3 GFP-HP1$\alpha/\beta/\gamma$ cell lines stably expressing GFP-tagged HP1 isoforms.

[c] In the iMEF *Suv39h* dn cells HP1 did not colocalize with the chromocenters, although they were still present as evident from the DAPI staining or the H2A-RFP distribution. The results in euchromatin and PCH were well described by a pure diffusion model and were indistinguishable with respect to the values determined for D_{eff} and the immobile fraction. Accordingly, only the average value of measurements in different chromatin compartments is given for the iMEF *Suv39h* dn cells.

[d] In *Suv4-20h* knockout cells HP1 still localized to PCH.

[e] The mobility of JMJD2C-GFP and PAX3-GFP in euchromatin and PCH was well described by an effective diffusion model. Cells were co-transfected with H2A-RFP to identify PCH.

[f] SUV39H1-GFP transfected into iMEF *Suv39h* dn cells was enriched at PCH in about 25% of the cells after 24 h. Chromocenters were identified by an H2A-RFP costaining. FRAP data are average values of randomly picked cells.

[g] SUV39H1 mutants that were either hyperactive (H320R) or inactive (H324L) with respect to wild-type (Rea et al, 2000). These mutants showed no changes in protein-binding rates for class II and III binding. However, the immobilized protein fraction of SUV39H1 (wild-type: 20 ± 5%) was slightly larger for the hyperactive (25 ± 8%) and smaller for the inactive protein (6 ± 3%).

Supplementary Table S3. Measured and calculated molecular weights and hydrodynamic parameters.

Complex	$M_{exp}{}^a$ (kDa)	$M_{calc}{}^b$ (kDa)	$S_{exp}{}^c$ (S)	$S_{calc}{}^d$ (S)	$D_{exp}{}^e$ ($\mu m^2 s^{-1}$)	$D_{calc}{}^d$ ($\mu m^2 s^{-1}$)	$\bar{v}{}^b$ (ml g^{-1})
HP1β	n. d.	22.7	2.0 ± 0.1	1.9	n. d.	76	0.728
HP1β-HP1β	46.7 ± 3.2	45.4	2.8 ± 0.1	2.7	76 ± 8	52	0.728
CD	9.0 ± 0.2	9.4	1.4 ± 0.1	1.2	n. d.	104	0.731
CSD-CSD	21.0 ± 0.3	21.5	1.9 ± 0.2	2.2	n. d.	92	0.726

Molecular weights and hydrodynamic parameters of recombinant mouse His-tagged full-length HP1β and its isolated chromodomain (CD) and chromoshadow domain (CSD) in the concentration range from 8-30 µM. At these concentrations HP1β formed a stable dimer via its CSD domain as apparent from the measured hydrodynamic parameters. Values refer to H_2O and a temperature of 20 °C as standard state. At low µM concentrations a *bona fide* monomeric HP1β species appeared at 2.0 ± 0.1 S with an equilibrium dissociation constant of 1-2 µM as determined from the relative molar fractions of monomer and dimer species (Fig 2A).

[a] Determined by sedimentation equilibrium ultracentrifugation and data analysis with Ultrascan (Demeler, 2005). Equilibrium data sets from three different loading concentrations at three speeds were used for a global curve fitting analysis to a one-component model.

[b] Calculated from amino acid composition with Sednterp (Laue et al, 1992) and a value of 0.546 ml g^{-1} for the partial specific volume of DNA.

[c] Determined from the averaged peak in the sedimentation coefficient $c(s)$-distribution after sedimentation velocity ultracentrifugation.

[d] Calculated from the pdb coordinates with Hydropro (Garcia De La Torre et al, 2000).

Supplementary Table S4. Summary of protein-protein associations.

	HP1α	HP1β	HP1γ	SUV39H1	SUV39H2	SUV4-20H1	SUV4-20H2	DNMT1	MBD1	MECP2
HP1α	+									
HP1β	+	+								
HP1γ	+	+	+							
SUV39H1	+	+	+	+						
SUV39H2	n.d.	n.d.	n.d.	n.d.	n.d.					
SUV4-20H1	n.d.	n.d.	n.d.	n.d.	n.d.	n.d.				
SUV4-20H2	+	+	+	n.d.	n.d.	—	+			
DNMT1[a]	+	+	n.d.	+	n.d.	n.d.	n.d.	+		
MBD1[b,d]	+	n.d.	n.d.	+	n.d.	n.d.	n.d.	n.d.	n.d.	
MECP2[c,d]	+	+	+	+	n.d.	n.d.	n.d.	+	n.d.	n.d.

Summary of protein-protein associations within the PCH network from FCCS and F2H experiments conducted in this study and supplemented with previously published data for MBD-containing proteins. The FCCS and F2H studies conducted here provide a direct readout for interaction in living mouse cells. For HP1β and its CD and CSD domains we also determined by analytical ultracentrifugation experiments that the protein forms a dimer via its CSD with a K_d of 1-2 μM for the dimerization and no higher order complex up to a concentration of 30 μM. Furthermore, the FCCS experiments demonstrated that all HP1 isoforms show homo- and heterodimerization. The HP1 interaction with either SUV39H1 or SUV4-20H2 was tested via the F2H assay and the F2H interaction analysis for SUV4-20H2 was conducted previously (Hahn et al, 2013). Interaction of HP1 and SUV39H1 with DNMT1, MBD1 and MECP2 were reported previously in the studies referenced below.

[a] HP1: (Fuks et al, 2003; Lehnertz et al, 2003; Smallwood et al, 2007). SUV39H1: (Esteve et al, 2006; Fuks et al, 2003). DNMT1: (Fellinger et al, 2009)

[b] HP1: (Fujita et al, 2003). SUV39H1: (Fujita et al, 2003)

[c] HP1: (Agarwal et al, 2007). SUV39H1: (Lunyak et al, 2002). DNMT1: (Kimura & Shiota, 2003)

[d] Tethering MBD1-GFP or GFP-MECP2 to the *lac*O-arrays resulted in the recruitment of RFP-HP1α but not of RFP-SUV39H1. Although interactions of MBD1/MECP2 and SUV39H1 have been shown in pulldown experiments (Fujita et al, 2003; Lunyak et al, 2002), this interaction was not reproduced in the F2H assay when testing for all possible combinations of N- or C-terminally tagged proteins.

Supplementary Table S5. Perturbations of PCH features.

	DAPI-dense DNA	5meC	DNMT1	MECP2	MBD1	H3K9me3	SUV39H1/2	HP1α/β/γ	H4K20me3	SUV4-20H1/2
Wild-type	+	+	+	+	+	+	+	+	+	+
Suv39h1/2 **double null**[a]	+	+	+[b]	+[b]	+[b]	–	dn[a]	–	–[c]	–[c]
JMJD2B overexpr.	+	n.d.	n.d.	n.d.	n.d.	–[d]	n.d.	n.d.	n.d.	n.d.
Suv4-20h1/2 **double null**	+	n.d.	n.d.	n.d.	n.d.	+	+	+	–[e]	dn[e]
TSA histone acetylation	–[f]	n.d.	n.d.	n.d.	n.d.	–[f]	–	–[f]	n.d.	n.d.
HP1α/β/γ knock down	+	n.d.	n.d.	n.d.	n.d.	–	–	k.d.	n.d.	n.d.
G2 phase	+	n.d.	+	n.d.	n.d.	+	+	–	+	+

The following perturbations were considered: (i) Varying the histone methylation levels of H3K9 and H4K20 by knockout of the responsible methylases or alternatively by JMJD2 overexpression, (ii) inhibiting histone methylation by enhanced acetylation due to inhibition of deacetylation via TSA, (iii) manipulating the abundance of potential interaction partners like HP1 in knockdown experiments, (iv) loss of HP1 due to H3 serine 10 phosphorylation and H3 lysine 14 acetylation during G2 phase. These parameters affected protein binding and localization to reveal interdependencies of the network. The '**+**' designation shows that the PCH condensation state, DNA or histone modifications or protein binding

remained similar to the wild-type state. In contrast, '–' indicates significant alterations. References to observations made already in previous publications are given below.

[a] The effects of both SUV39H1 and SUV39H2 deficiency were initially described in (Peters et al, 2001)

[b] DNMT1, MBD1 and MECP2 remained localizing at PCH as shown in (Brero et al, 2005; Lehnertz et al, 2003) and in Supplementary Fig S2B

[c] Loss of SUV4-20H and H4K20me3 from PCH was shown previously (Schotta et al, 2004)

[d] Due to overexpression of the H3K9me3-specific demethylase JMJD2C the H3K9me3 level was drastically reduced (Fodor et al, 2006). This effect was quantitated here (Fig 8C).

[e] *Suv4-20h* dn cells and their effect on H4K20me3 were published by Schotta et al. (Schotta et al, 2008)

[f] According to Fig S2D and previous references (Fejes Tóth et al, 2004; Maison et al, 2002; Taddei et al, 2001) histone hyperacetylation induced decondensation of heterochromatin/PCH.

Supplementary Table S6. Cell cycle-dependent mobility of SUV39H1 and HP1α.

Protein Cell line	Cell cycle	Chromatin	n	D_{eff} (µm² s^{-1})	k_{off} (s^{-1})	k^*_{on} (s^{-1})	K_{aff}	*Free* (%)	*Bound* (%)	f_{im} (%)
GFP-**HP1α** NIH-3T3	G1	Eu [a]	10	0.24 ± 0.06	–	–	–	98 ± 2	–	2 ± 2
		PCH [b]	9	0.9 ± 0.6	0.22 ± 0.09	0.6 ± 0.2	2.7 ± 0.8	27 ± 6	67 ± 6	6 ± 3
	S	Eu [a]	9	0.18 ± 0.03	–	–	–	95 ± 3	–	5 ± 3
		PCH [b]	12	1.1 ± 0.5	0.22 ± 0.04	0.7 ± 0.1	3.1 ± 0.5	24 ± 3	71 ± 3	5 ± 4
	G2	Eu [a]	14	0.17 ± 0.04	–	–	–	99 ± 1	–	1 ± 1
		PCH [b]	18	0.09 ± 0.02	–	–	–	97 ± 2	–	3 ± 2
SUV39H1-GFP NIH-3T3	G1	Eu	5	0.3 ± 0.4	0.12 ± 0.10	0.2 ± 0.2	1.5 ± 0.03	40 ± 0	59 ± 0	1 ± 1
		PCH	5	0.5 ± 0.1	0.08 ± 0.03	0.3 ± 0.2	3.4 ± 1.0	22 ± 5	71 ± 5	7 ± 7
	S	Eu	11	0.7 ± 0.7	0.6 ± 0.6	1.7 ± 2.4	2.5 ± 0.7	28 ± 5	69 ± 5	3 ± 2
		PCH	11	0.5 ± 0.4	0.15 ± 0.06	0.6 ± 0.2	3.7 ± 0.5	18 ± 3	65 ± 3	17 ± 8
	G2	Eu	13	1.1 ± 0.7	0.2 ± 0.1	0.9 ± 1.1	3.0 ± 1.5	29 ± 6	68 ± 6	3 ± 3
		PCH	12	0.3 ± 0.2	0.05 ± 0.01	0.3 ± 0.3	5.3 ± 2.8	20 ± 7	69 ± 7	11 ± 5
	M [c]	mitotic chromatin	11	6 ± 5	1.2 ± 0.4	3 ± 1	2.4 ± 0.2	28 ± 2	67 ± 2	5 ± 3

FRAP measurements were assigned to cell cycle phases via PCNA-based identification of G1 and S phase. Cells in G2 phase were identified via delocalization of co-transfected RFP-HP1α. Values refer to the average of n experiments. For SUV39H1 no significant cell cycle-dependent differences in mobility were detected. For HP1α an increased mobility in PCH was observed in G2. Errors correspond to 95 % confidence intervals.

[a] In euchromatin the GFP-HP1 mobility is well described by a diffusion-dominant model. Here, the effective diffusion coefficient D_{eff} also includes low affinity/transient binding contributions of HP1.

[b] For PCH a reaction-diffusion model was applied to yield the diffusion coefficient as well as the kinetic rate constants for binding.

[c] Due to the high mobility of mitotic cells, average values were associated with relatively high error ranges.

**Supplementary Table S7. Parameters used for modeling the PCH network.**

Parameter	Value	Comment
Nuclear volume	3259 ± 85 μm^3	NIH-3T3 mouse fibroblast cells (Cantaloube et al, 2012)
Mouse genome size	$5 \cdot 10^9$ bp	G1, diploid
PCH (fraction of major satellite rep.)	3.6 %	Mouse genome sequencing, percentage of reads (Waterston et al, 2002)
Number of chromocenters	28 ± 1	DAPI/HP1 staining and automated 3D microscopy analysis (Cantaloube et al, 2012)
Average genome content of single chromocenter	6.4 Mb	PCH genome fraction and number of chromocenters
Total volume of all chromocenters	75 ± 2 μm^3	DAPI/HP1 staining and automated 3D microscopy analysis (Cantaloube et al, 2012)
Average volume of single chromocenter	2.69 ± 0.04 μm^3	Chromocenter volume and number of chromocenters
PCH volume fraction	2.31 ± 0.06 %	Nuclear volume fraction of chromocenter volume
Eu volume fraction	97.69 ± 0.06 %	100 % minus PCH volume fraction
PCH compaction ratio	1.8 ± 0.3-fold	H2A-RFP fluorescence PCH vs. Eu (Fig 1B)
Nucleosome repeat length (NRL)	191.1 ± 0.5 bp	MNase-seq in mouse fibroblasts (Teif et al, 2012)
Nucleosomes per nucleus	$(26.2 \pm 0.1) \cdot 10^6$	Genome size / NRL
Nucleosome conc. average	134 ± 4 μM	Number of nucleosomes / nuclear volume
Nucleosome conc. PCH	234 ± 4 μM	From PCH compaction and PCH genome fraction
Nucleosome conc. Eu	130 ± 4 μM	Remaining 96.4 % genome fraction

Parameter	Value	Comment
H3K9me3 average	28 ± 2 %	Mass spectrometry NIH-3T3 (Fodor et al, 2006)
H3K9me3 wt PCH	38 ± 5 %	Fig 3C
H3K9me3 wt Eu	28 ± 2 %	Fig 3C
H3K9me3 *Suv39h* dn PCH	13 ± 2 %	Fig 3C
H3K9me3 *Suv39h* dn Eu	25 ± 4 %	Fig 3C
Concentration free HP1 dimer	1.5 µM	c_h, calculated from FCS and FRAP data as described above in "Measurements of endogenous protein concentrations…"
Concentration free SUV39H dimer	0.05 µM	c_s, calculated from FCS and FRAP data as described above in "Measurements of endogenous protein concentrations…"
Total nuclear concentration HP1 dimer	9.8 µM	Average of measured PCH and Eu concentrations weighted according to nuclear volume fraction
Total nuclear concentration SUV39H dimer	0.33 µM	Average of measured PCH and Eu concentrations weighted according to nuclear volume fraction
Specificity ratio SUV39H	> 8.3	Specificity ratio of PCH vs. euchromatin for SUV39H according to Fig 3D
Specificity ratio G9A/SETDB1	< 2.2	Specificity ratio of euchromatin vs. PCH for histone methylases G9A and SETDB1 according to Fig 3D
Methylation by SUV39H	$4.8 \cdot 10^{-4}$ µM^{-1} min^{-1}	k_m, from fit to measured methylation levels
Unspecific methylation	$1.8 \cdot 10^{-4}$ min^{-1}	k_u, from fit to measured H3K9me3 methylation that occurs both in PCH and euchromatin
Euchromatic methylation	$2.6 \cdot 10^{-4}$ min^{-1}	k_e, from fit to measured H3K9me3 methylation that is specific to euchromatin by G9A/SETDB1
Demethylation	$13 \cdot 10^{-4}$ min^{-1}	k_{-m}, from mass spectrometry experiments in HeLa cells (Zee et al, 2010)
Chromatin association rate of SUV39H and HP1	1.05 µM^{-1} min^{-1}	k_+, estimated parameter based on class II binding, see above "Estimation of kinetic association rate..."
k_{off} HP1 class II	20 min^{-1}	k_{-h2}, experimentally determined parameter
k_{off} HP1 class IV	0.5 min^{-1}	k_{-h4}, experimentally determined parameter
k_{off} SUV39H class I	120 min^{-1}	k_{-s1}, experimentally determined parameter
k_{off} SUV39H class II	11.3 min^{-1}	k_{-s2}, experimentally determined parameter
k_{off} SUV39H class III	2.0 min^{-1}	k_{-s3}, experimentally determined parameter
k_{off} SUV39H class IV	0.25 min^{-1}	k_{-s4}, experimentally determined parameter
SUV39H looping conc.	0-14 µM	j_M, from chromatin bound SUV39H (Fig 7A)

Parameter	Value	Comment
Nucleosomes without H3K9me3	72 %	Variable *n*, recovered from model
Nucleosomes with H3K9me3	28 %	Variable *m,* recovered from model with H3K9me3 averages of 38% in PCH and 28% in euchromatin
HP1-bound *m* nucleosome	5.7 µM	Variable *Hm*, concentration calculated from model based on FRAP binding rates
SUV39H-bound *m* nucleosome	0.03 µM	Variable *Sm*, concentration calculated from model based on FRAP binding rates
HP1-SUV39H *m* complex	0.01 µM	Variable *SHm*, concentration calculated from model based on FRAP binding rates
SUV39H methylation origins in PCH (free plus occupied)	29.6 µM	Variable *o*, concentration calculated from model based on FRAP binding rates
HP1-bound origins in PCH	2.0 µM	Variable *Ho*, concentration calculated from model based on FRAP binding rates
SUV39H-bound origins in PCH	0.6 µM	Variable *So*, concentration calculated from model based on FRAP binding rates
HP1-SUV39H origin complex in PCH	1.4 µM	Variable *SHo*, concentration of stably bound SUV39H dimer (class IV)

The values given for the parameters listed in the table and used for the modeling in Fig 7 and Fig 8 were either determined in this study or taken from the indicated references. Measured parameters for the concentration and chromatin interactions of the three different HP1 isoforms as well as for the SUV39H1 and SUV39H2 were integrated into a single 'virtual' HP1 or SUV39H protein, respectively. For protein concentrations the isoform values were added. For kinetic off rates, weighted averages according to relative abundance are given.
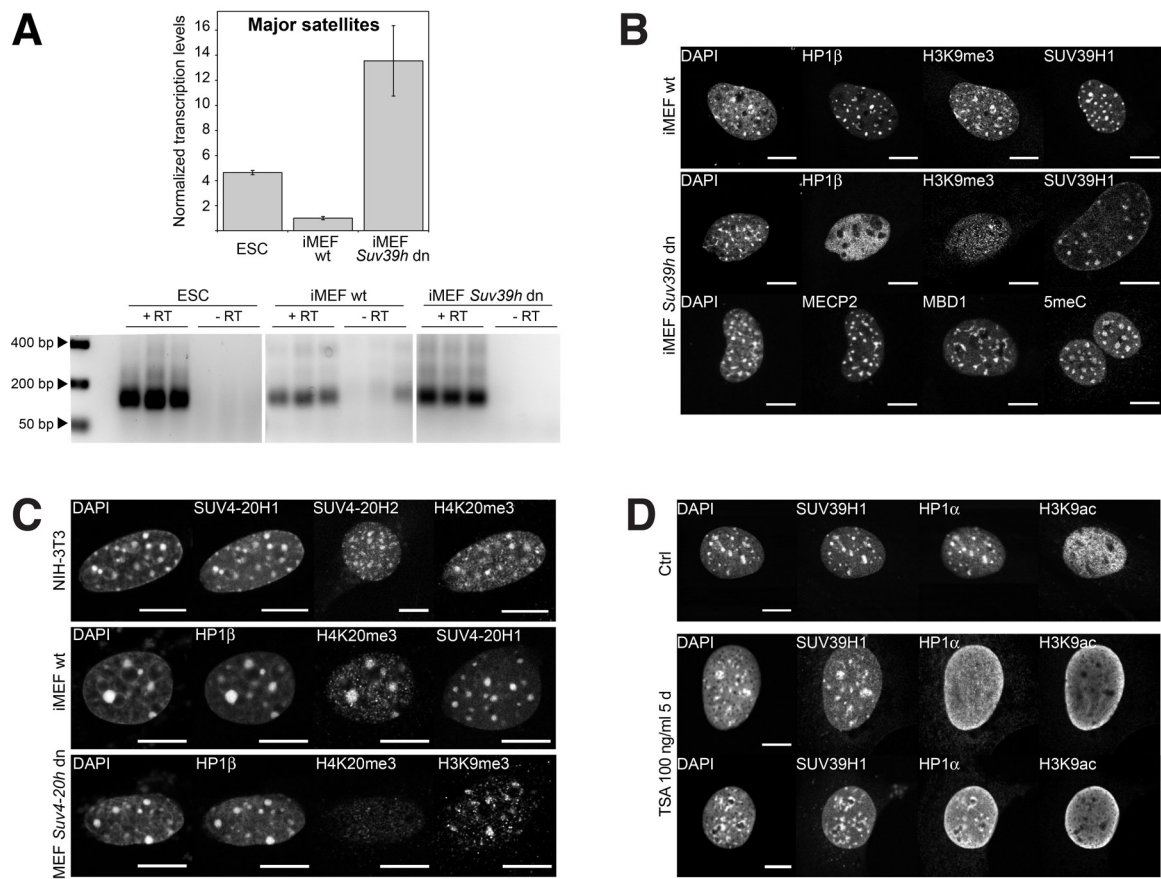
Supplementary Figures
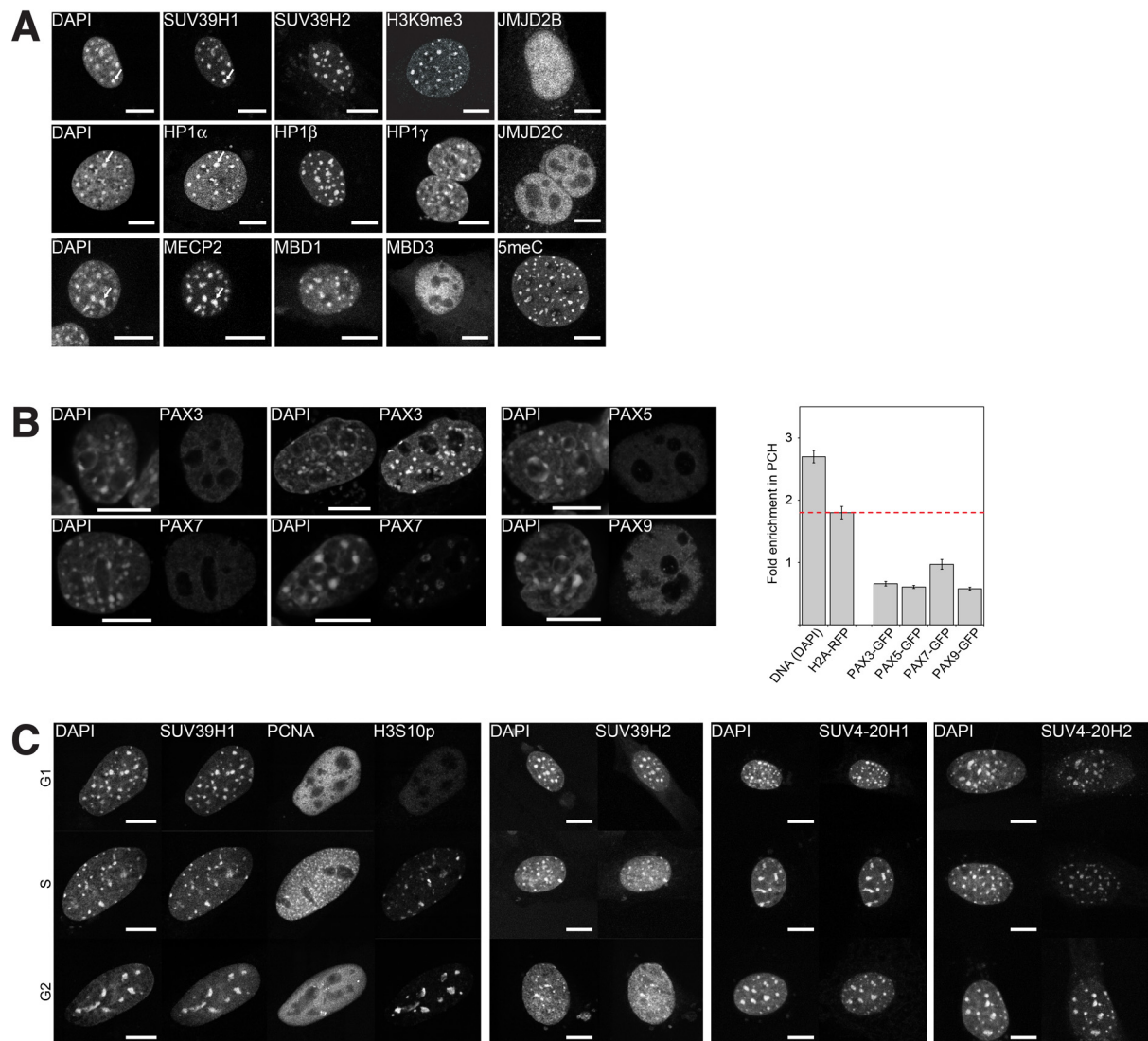
Supplementary Figure S1. CLSM images of nuclear localization of PCH factors in NIH-3T3 mouse embryonic fibroblasts.

The colocalization of GFP-tagged proteins or histone/DNA modifications visualized by immunostaining with PCH foci identified from DAPI staining was evaluated. Scale bars, 10 µm.

A The H3K9me3 mark and the responsible histone methylases SUV39H1 and SUV39H2 colocalized with the HP1 isoforms at PCH. In contrast, the H3K9-specific histone demethylases JMJD2B and JMJD2C were homogeneously distributed throughout the whole nucleus, showing no clear binding preference for euchromatin or PCH. Immunostaining for 5-methylcytosine (5meC) demonstrated the localization of highly methylated DNA in PCH regions. MECP2 and MBD1, both binding to methylated DNA

via their MBD, followed the DNA methylation pattern in PCH. MBD3, which despite having an MBD-domain is unable to bind methylated DNA, displayed a mostly euchromatic localization as reported previously (Hendrich & Bird, 1998). In general, proteins that localized to PCH displayed this behavior for all foci present in a given cell. Accordingly, they also colocalize with the other factors enriched at these sites.

B   Nuclear distribution of transcription factors PAX3, PAX5, PAX7 and PAX9 (Bulut-Karslioglu et al, 2012) that have been proposed to recruit heterochromatin factors to PCH via DNA sequence-specific binding. For all GFP-tagged PAX3/5/7/9 factors a rather homogeneous distribution was observed. PAX3 and PAX7 enrichment at PCH was only observed for a subgroup of cells with high over-expression levels (about 5% and 29%, respectively). PAX5 was used as a negative control since PCH does not contain a PAX5 binding site. Error bars correspond to SD.

C   Both SUV39H and SUV4-20H histone lysine methylases remained associated with chromatin during G1, S and G2 cell-cycle phases. SUV4-20H1 and SUV4-20H2 as well as the H4K20me3 modification set by these enzymes were enriched in PCH.

Supplementary Figure S2. Major satellite repeat transcription measured by RT-qPCR and CLSM analysis of PCH organization in different cell types and knock-out cell lines.

A   Quantification of major satellite repeat transcription levels by RT-qPCR in ESCs, iMEF wt cells and iMEF *Suv39h* dn cells. Transcription levels were about 4.6 ± 0.2-fold higher for major satellites in ESCs as compared to fully differentiated iMEF wt cells. Furthermore, transcription levels further increased to 14 ± 2-fold for major repeats in iMEF *Suv39h* dn as compared to iMEF wt. The PCR products from the negative control samples ('– RT', produced without reverse transcriptase) were used to confirm the absence of DNA contaminations. Some residual DNA was present in the third '– RT' iMEF sample, and thus this sample was not included in the quantification. Error bars correspond to SD.

B   Distribution of GFP-HP1β, H3K9me3 and SUV39H1-GFP relative to PCH in *Suv39h* dn cells that lost H3K9me3 and HP1β from PCH in agreement with previous reports (Müller et al, 2009; Peters et al, 2001). In contrast, the MBD-proteins MECP2 and MBD1 as well as 5meC remained enriched in PCH. As shown previously (Schotta et al, 2004), SUV4-

20H and H4K20me3 were lost from the chromocenters in iMEF *Suv39h* dn cells. PCH chromatin compaction in the DAPI dense chromocenters persisted in the absence of *Suv39h* and the enrichment of H3K9me3.

C   Distribution of HP1β, SUV4-20H1/2 and H4K20me3 in knockout iMEFs of both SUV4-20H isoforms. In *Suv4-20h* dn cells PCH foci lost H4K20me3 but HP1 and H3K9me3 remained enriched in the chromocenters.

D   Changes of PCH organization in NIH-3T3 cells due to inhibition of histone deacetylation by trichostatin A (TSA) treatment for 5 days induced partial PCH decondensation, with some cells showing an almost complete HP1 loss (upper panel), while in others HP1 was still present at PCH in significant amounts (lower panel). For SUV39H1 only a moderate loss of the protein from PCH was observed in response to histone hyperacetylation.
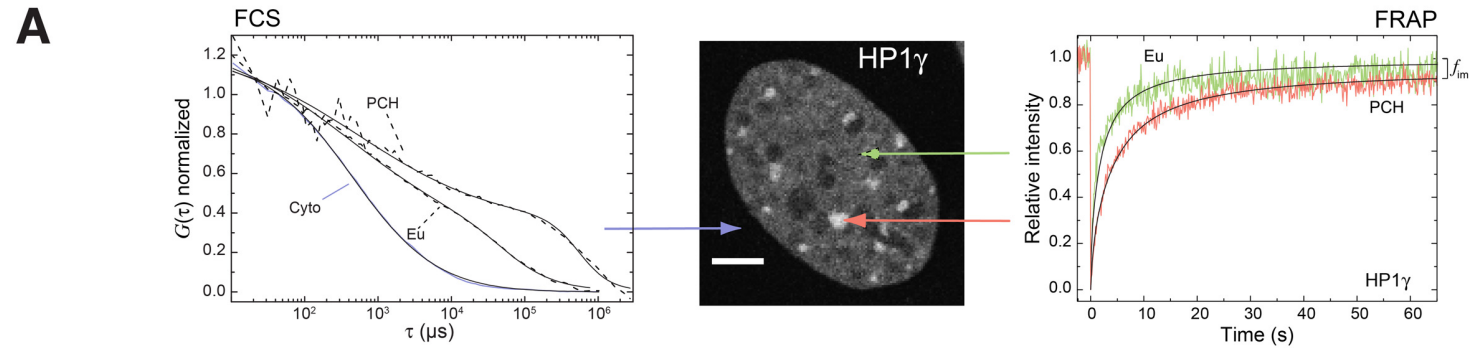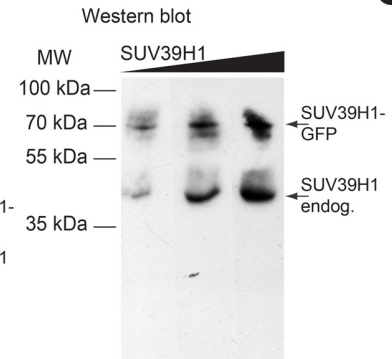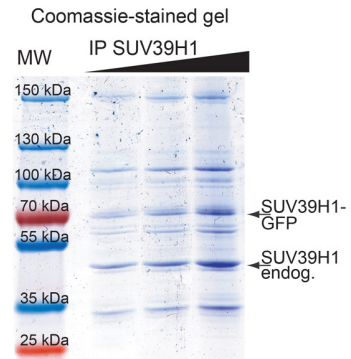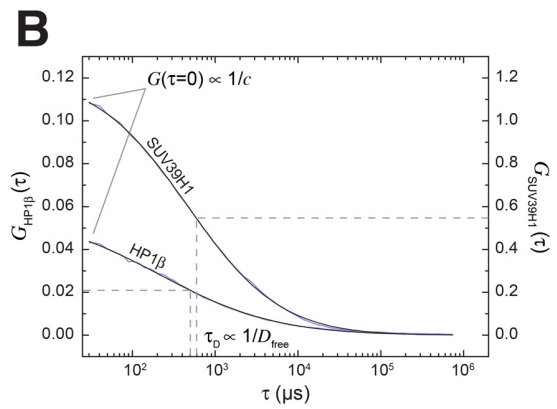
A

B

C
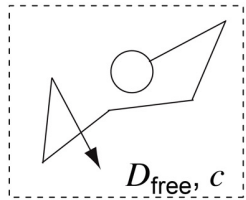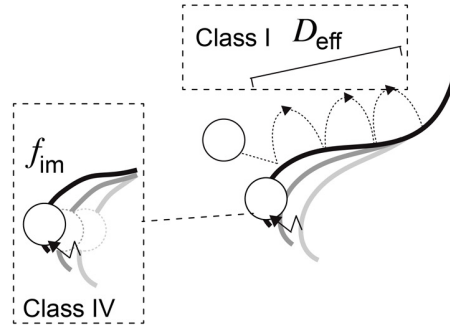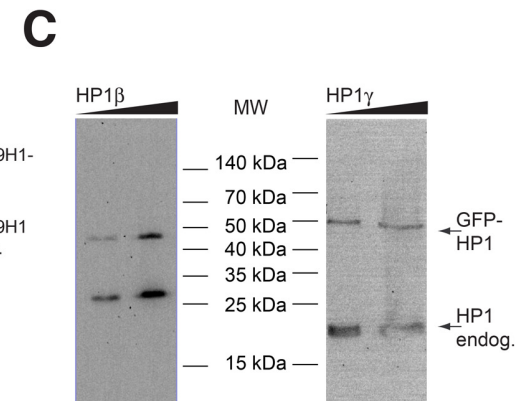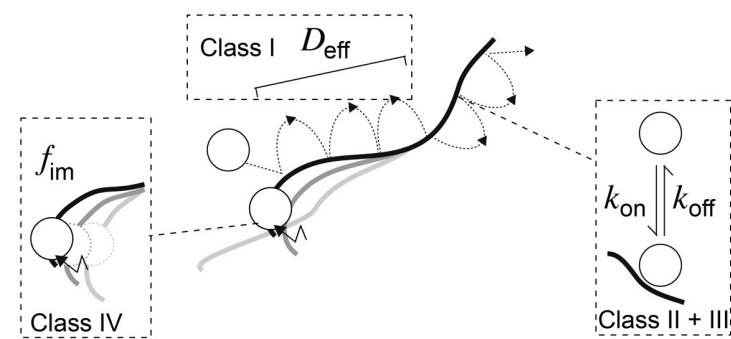
**Supplementary Figure S3. Quantification of protein parameters in living cells by FCS and FRAP**

A   Approach to determine protein mobility and chromatin interaction parameters by combining FCS and FRAP experiments at different intracellular locations. In FCS the signal intensity fluctuations of diffusing molecules are recorded and evaluated by computing the autocorrelation function depicted on the top left side. It provides the concentration c of fluorescently labeled molecules and the diffusion coefficient D as a direct readout (see also panel B). FCS measurements in the cytoplasm provide a reference value for the diffusion coefficient D_{free} in the absence of chromatin binding. Reduced mobility due to binding interactions in euchromatin and PCH is reflected in a longer diffusion time τ. FRAP experiments record the fluorescence signal before and after a high laser intensity bleach to measure the time dependence of the fluorescence signal recovery. By fitting the integrated intensity data of the bleached region to a diffusion or a reaction-diffusion model the characteristic parameters for different binding classes can be extracted: the effective diffusion coefficient D_{eff} that includes transient binding interactions, the kinetic on- and off-rates (k_{on}, k_{off}) of chromatin binding events and the protein fraction f_{im} that is immobile during the experiment. The minimal number of binding site classes needed to rationalize the data in a consistent manner was extracted from the parameters measured by FCS and FRAP as indicated. Scale bar, 10 µm.

B   Determination of endogenous protein concentrations. The amplitude of the FCS autocorrelation function is inversely proportional to the concentration of fluorescently labeled molecules. Experimental curves for HP1β and SUV39H1 in the cytoplasm are shown. FCS measurements in the cytoplasm were fit with a one-component anomalous diffusion model to extract the concentration of GFP-tagged protein in the cytoplasm. The endogenous protein concentrations were determined from the ratio of GFP-tagged protein to endogenous protein in a stably transfected cell line via Coomassie-stained SDS gels or quantitative western blots. Based on the quantification of immunoprecipitated as shown for SUV39H1(-GFP) the ratio of endogenous to labeled protein was determined and the endogenous protein concentration in the cytoplasm was calculated. The protein concentration ratios to PCH and euchromatin were derived from quantitative APD imaging, which determines average fluorescence intensities of the respective proteins in the different cellular compartments.

C   Determination of ratios of GFP-tagged to endogenous proteins for HP1β and HP1γ by western blot analysis. Corresponding values for HP1α were determined previously (Müller et al, 2009).
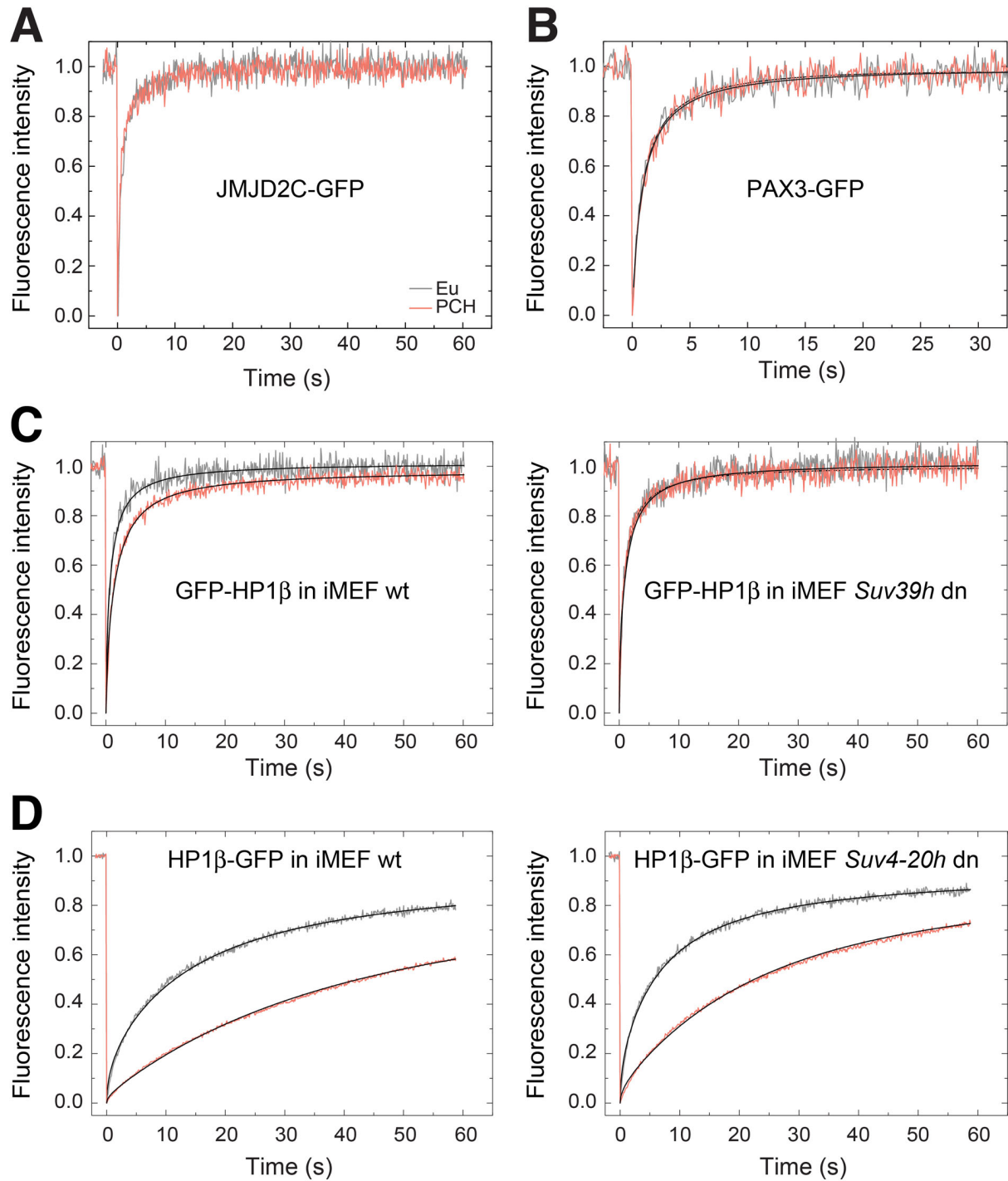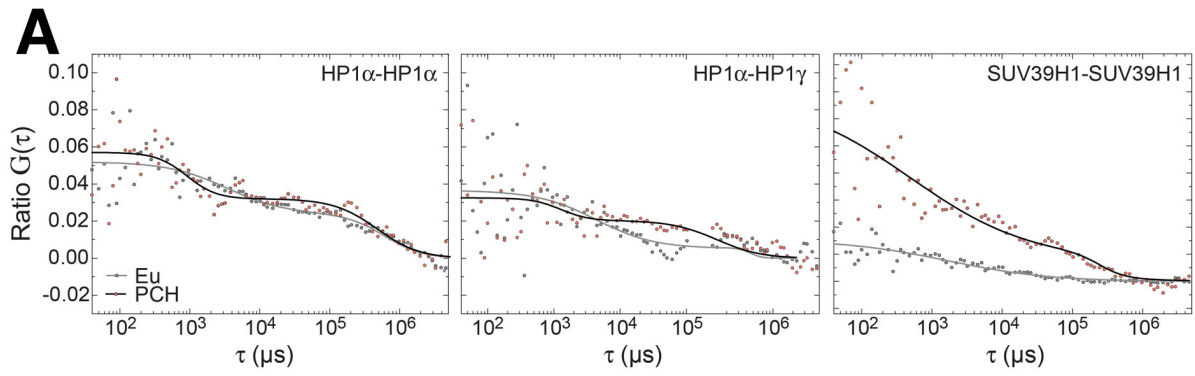
Supplementary Figure S4. FRAP analysis of JMJD2C, PAX3 and HP1β in *Suv39h* dn and *Suv4-20h* dn cells.

A   FRAP measurements of JMJD2C-GFP mobility in PCH in comparison to euchromatin. An NIH-3T3 cell line stably expressing H2A-RFP to identify PCH foci was transfected with JMJD2C-GFP, which was distributed homogeneously in the nucleus. The JMJD2C

mobility was similar in both compartments as evident from the overlay plot of the two curves.

B   Same as panel A but for PAX3-GFP, which also displayed a mostly homogeneous nuclear distribution. FRAP measurements in PCH versus euchromatin showed low chromatin binding affinity and a comparable protein mobility in both compartments.

C   FRAP measurements of HP1β in iMEF *Suv39h* dn cells. While HP1β–chromatin interactions in wt iMEFs (left panel) showed PCH-specific high-affinity binding, this feature was absent in *Suv39h* dn cells (right panel). For the latter, the recovery curves in PCH loci identified by H2A-RFP were well described by a diffusion model that yielded mobility values identical to those determined in euchromatic regions of wt iMEFs (Table S2).

D   FRAP measurements of HP1β-GFP in *Suv4-20h* dn iMEFs that lack both H4K20 methylases SUV4-20H1 and SUV4-20H2 in comparison to wt iMEFs. The mobility of HP1β in both euchromatin and PCH increased slightly while the immobile fraction was reduced in the *Suv4-20h* dn cells.
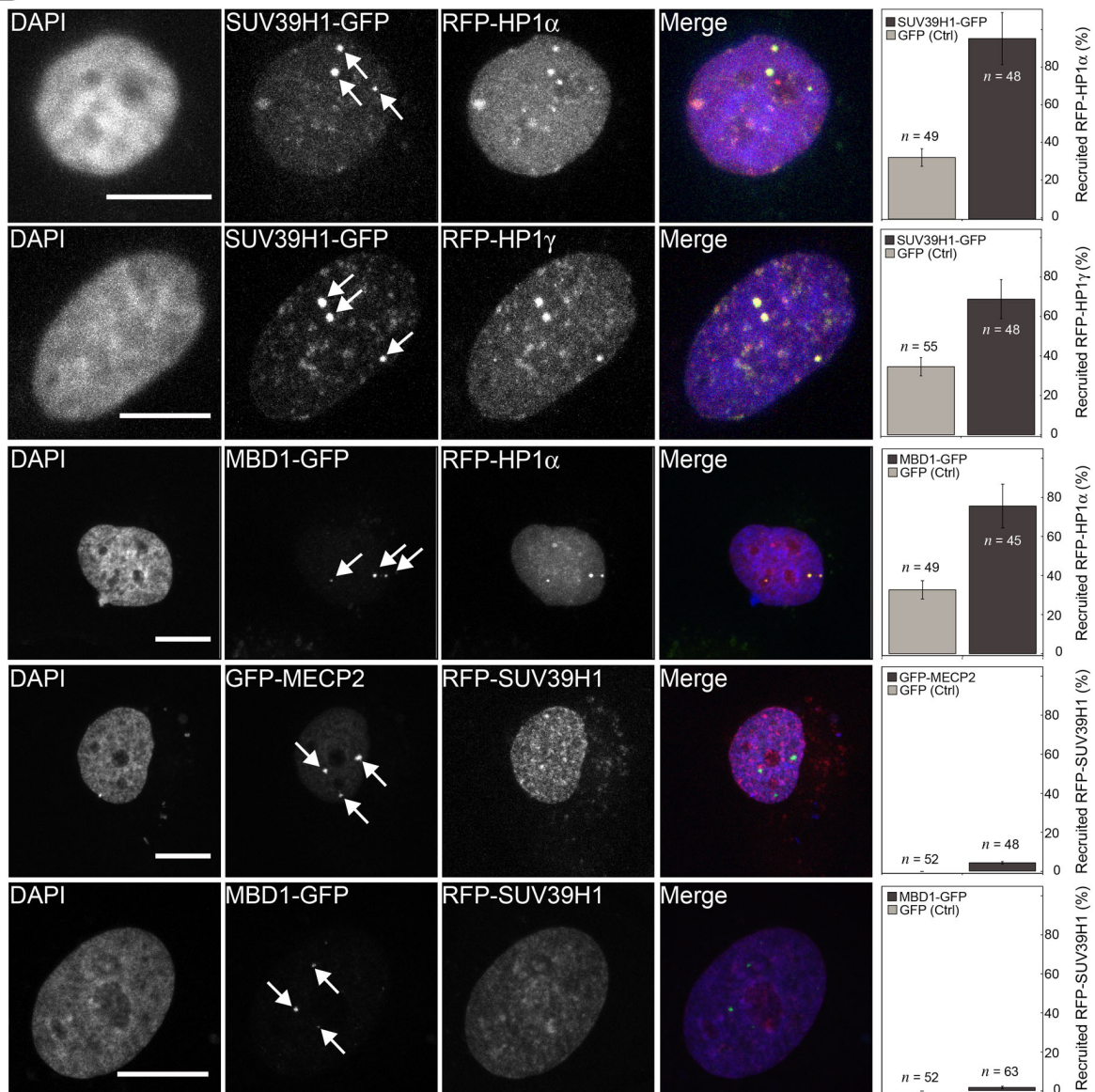
Supplementary Figure S5. Protein-protein interaction analysis of HP1 and SUV39H1 by FCCS and F2H experiments.

A FCCS measurements of interactions between HP1α and HP1γ and SUV39H1 (see Fig 2B for additional data). Quantitative analysis of FCCS curves revealed that most of the mobile HP1 pool existed as homo- or heterodimers. Furthermore, the FCCS experiments revealed self-association of soluble SUV39H1 in living cells. The soluble *bona fide* dimeric SUV39H1 protein fraction was calculated to comprise 24 ± 23 % of soluble SUV39H1 protein present at 0.34 µM concentration.

B F2H analysis of SUV39H1 and HP1 protein-protein interactions (see Fig 2C for additional data). All HP1 isoforms interacted with SUV39H1 in living cells with the percentage of colocalizations indicated in the histogram in comparison to a negative control represented by the isolated GFP domain. The relatively high residual degree of colocalization of HP1α and HP1γ in the controls probably reflects the enrichment of these proteins at the *lac*O-array in the absence of ectopic tethering. Self-association of SUV39H1 was clearly demonstrated by the F2H assay. Furthermore, both MECP2 and MBD1 recruited HP1 efficiently, while the interaction of RFP-SUV39H1 was not observed with the MBD proteins, MECP2 and MBD1. Variation of N- and C-terminal fluorescent labels in all possible combinations did not influence this result. Scale bars, 10 µm. Error bars show the SD.

Supplementary References

Agarwal N, Hardt T, Brero A, Nowak D, Rothbauer U, Becker A, Leonhardt H, Cardoso MC (2007) MeCP2 interacts with HP1 and modulates its heterochromatin association during myogenic differentiation. *Nucleic Acids Res* **35:** 5402-5408

Bacia K, Petrasek Z, Schwille P (2012) Correcting for Spectral Cross-Talk in Dual-Color Fluorescence Cross-Correlation Spectroscopy. *Chemphyschem* **13:** 1221-1231

Berg OG, von Hippel PH (1985) Diffusion-controlled macromolecular interactions. *Annu Rev Biophys Biophys Chem* **14:** 131-160

Brero A, Easwaran HP, Nowak D, Grunewald I, Cremer T, Leonhardt H, Cardoso MC (2005) Methyl CpG-binding proteins induce large-scale chromatin reorganization during terminal differentiation. *J Cell Biol* **169:** 733-743

Bulut-Karslioglu A, Perrera V, Scaranaro M, de la Rosa-Velazquez IA, van de Nobelen S, Shukeir N, Popow J, Gerle B, Opravil S, Pagani M, Meidhof S, Brabletz T, Manke T, Lachner M, Jenuwein T (2012) A transcription factor-based mechanism for mouse heterochromatin formation. *Nat Struct Mol Biol* **19:** 1023-1030

Cantaloube S, Romeo K, Le Baccon P, Almouzni G, Quivy JP (2012) Characterization of chromatin domains by 3D fluorescence microscopy: An automated methodology for quantitative analysis and nuclei screening. *BioEssays* **34:** 509-517

Chung I, Leonhardt H, Rippe K (2011) De novo assembly of a PML nuclear subcompartment occurs through multiple pathways and induces telomere elongation. *J Cell Sci* **124:** 3603-3618

Demeler B (2005) UltraScan - a comprehensive data analysis software package for analytical ultracentrifugation experiments. In *Modern Analytical Ultracentrifugation: Techniques and Methods*, Scott DJ, Harding SE, Rowe AJ (eds), pp 210-229. Cambridge: The Royal Society of Chemistry

Efroni S, Duttagupta R, Cheng J, Dehghani H, Hoeppner DJ, Dash C, Bazett-Jones DP, Le Grice S, McKay RD, Buetow KH, Gingeras TR, Misteli T, Meshorer E (2008) Global transcription in pluripotent embryonic stem cells. *Cell Stem Cell* **2:** 437-447

Erdel F, Müller-Ott K, Baum M, Wachsmuth M, Rippe K (2011) Dissecting chromatin interactions in living cells from protein mobility maps. *Chromosome Res* **19:** 99-115

Erdel F, Müller-Ott K, Rippe K (2013) Establishing epigenetic domains via chromatin-bound histone modifiers. *Ann N Y Acad Sci* **1305:** 29-43

Erdel F, Schubert T, Marth C, Langst G, Rippe K (2010) Human ISWI chromatin-remodeling complexes sample nucleosomes via transient binding reactions and become immobilized at active sites. *Proc Natl Acad Sci USA* **107:** 19873-19878

Esteve PO, Chin HG, Smallwood A, Feehery GR, Gangisetty O, Karpf AR, Carey MF, Pradhan S (2006) Direct interaction between DNMT1 and G9a coordinates DNA and histone methylation during replication. *Genes Dev* **20:** 3089-3103

Fejes Tóth K, Knoch TA, Wachsmuth M, Stöhr M, Frank-Stöhr M, Bacher CP, Müller G, Rippe K (2004) Trichostatin A induced histone acetylation causes decondensation of interphase chromatin. *J Cell Sci* **117:** 4277-4287

Fejes Tóth K, Mazurkiewicz J, Rippe K (2005) Association states of the nucleosome assembly protein 1 and its complexes with histones. *J Biol Chem* **280:** 15690-15699

Fellinger K, Rothbauer U, Felle M, Langst G, Leonhardt H (2009) Dimerization of DNA methyltransferase 1 is mediated by its regulatory domain. *J Cell Biochem* **106:** 521-528

Fodor BD, Kubicek S, Yonezawa M, O'Sullivan RJ, Sengupta R, Perez-Burgos L, Opravil S, Mechtler K, Schotta G, Jenuwein T (2006) Jmjd2b antagonizes H3K9 trimethylation at pericentric heterochromatin in mammalian cells. *Genes Dev* **20:** 1557-1562

Fujita N, Watanabe S, Ichimura T, Tsuruzoe S, Shinkai Y, Tachibana M, Chiba T, Nakao M (2003) Methyl-CpG Binding Domain 1 (MBD1) Interacts with the Suv39h1-HP1 Heterochromatic Complex for DNA Methylation-based Transcriptional Repression. *J Biol Chem* **278:** 24132-24138

Fuks F, Hurd PJ, Deplus R, Kouzarides T (2003) The DNA methyltransferases associate with HP1 and the SUV39H1 histone methyltransferase. *Nucleic Acids Res* **31:** 2305-2312

Garcia De La Torre J, Huertas ML, Carrasco B (2000) Calculation of hydrodynamic properties of globular proteins from their atomic-level structure. *Biophys J* **78:** 719-730

Gillespie DT (2007) Stochastic simulation of chemical kinetics. *Annu Rev Phys Chem* **58:** 35-55

Hahn M, Dambacher S, Dulev S, Kuznetsova AY, Eck S, Worz S, Sadic D, Schulte M, Mallm JP, Maiser A, Debs P, von Melchner H, Leonhardt H, Schermelleh L, Rohr K, Rippe K, Storchova Z, Schotta G (2013) Suv4-20h2 mediates chromatin compaction and is important for cohesin recruitment to heterochromatin. *Genes Dev* **27:** 859-872

Hendrich B, Bird A (1998) Identification and characterization of a family of mammalian methyl-CpG binding proteins. *Mol Cell Biol* **18:** 6538-6547

Jegou T, Chung I, Heuvelmann G, Wachsmuth M, Görisch SM, Greulich-Bode K, Boukamp P, Lichter P, Rippe K (2009) Dynamics of telomeres and promyelocytic leukemia nuclear bodies in a telomerase negative human cell line. *Mol Biol Cell* **20:** 2070-2082

Kepert JF, Fejes Tóth K, Caudron M, Mücke N, Langowski J, Rippe K (2003) Conformation of reconstituted mononucleosomes and effect of linker histone H1 binding studied by scanning force microscopy. *Biophys J* **85:** 4012-4022

Kimura H, Shiota K (2003) Methyl-CpG-binding protein, MeCP2, is a target molecule for maintenance DNA methyltransferase, Dnmt1. *J Biol Chem* **278:** 4806-4812

Laue TM, Shah BD, Ridgeway TM, Pelletier SL (1992) Computer aided interpretation of analytical sedimentation data for proteins. In *Analytical Ultracentrifugation in Biochemistry and Polymer Science*, Harding SE, Rowe AJ, Horton JC (eds), pp 90-125. Cambridge: Royal Society of Chemistry

Lehnertz B, Ueda Y, Derijck AA, Braunschweig U, Perez-Burgos L, Kubicek S, Chen T, Li E, Jenuwein T, Peters AH (2003) Suv39h-mediated histone H3 lysine 9 methylation directs DNA methylation to major satellite repeats at pericentric heterochromatin. *Curr Biol* **13:** 1192-1200

Lunyak VV, Burgess R, Prefontaine GG, Nelson C, Sze SH, Chenoweth J, Schwartz P, Pevzner PA, Glass C, Mandel G, Rosenfeld MG (2002) Corepressor-dependent silencing of chromosomal regions encoding neuronal genes. *Science* **298:** 1747-1752

Maison C, Bailly D, Peters AH, Quivy JP, Roche D, Taddei A, Lachner M, Jenuwein T, Almouzni G (2002) Higher-order structure in pericentric heterochromatin involves a distinct pattern of histone modification and an RNA component. *Nat Genet* **30:** 329-334

Muller CB, Weiss K, Richtering W, Loman A, Enderlein J (2008) Calibrating differential interference contrast microscopy with dual-focus fluorescence correlation spectroscopy. *Opt Express* **16:** 4322-4329

Müller KP, Erdel F, Caudron-Herger M, Marth C, Fodor BD, Richter M, Scaranaro M, Beaudouin J, Wachsmuth M, Rippe K (2009) Multiscale analysis of dynamics and interactions of heterochromatin protein 1 by fluorescence fluctuation microscopy. *Biophys J* **97:** 2876-2885

Pack C, Saito K, Tamura M, Kinjo M (2006) Microenvironment and effect of energy depletion in the nucleus analyzed by mobility of multiple oligomeric EGFPs. *Biophys J* **91:** 3921-3936

Peters AH, O'Carroll D, Scherthan H, Mechtler K, Sauer S, Schofer C, Weipoltshammer K, Pagani M, Lachner M, Kohlmaier A, Opravil S, Doyle M, Sibilia M, Jenuwein T (2001) Loss of the Suv39h histone methyltransferases impairs mammalian heterochromatin and genome stability. *Cell* **107:** 323-337

Phillip Y, Kiss V, Schreiber G (2012) Protein-binding dynamics imaged in a living cell. *Proc Natl Acad Sci USA* **109:** 1461-1466

Philo JS (2000) A method for directly fitting the time derivative of sedimentation velocity data and an alternative algorithm for calculating sedimentation coefficient distribution functions. *Anal Biochem* **279:** 151-163

Rea S, Eisenhaber F, O'Carroll D, Strahl BD, Sun ZW, Schmid M, Opravil S, Mechtler K, Ponting CP, Allis CD, Jenuwein T (2000) Regulation of chromatin structure by site-specific histone H3 methyltransferases. *Nature* **406:** 593-599

Rippe K (2001) Making contacts on a nucleic acid polymer. *Trends Biochem Sci* **26:** 733-740

Rippe K, von Hippel PH, Langowski J (1995) Action at a distance: DNA-looping and initiation of transcription. *Trends Biochem Sci* **20:** 500-506

Rothbauer U, Zolghadr K, Muyldermans S, Schepers A, Cardoso MC, Leonhardt H (2008) A versatile nanotrap for biochemical and functional studies with fluorescent fusion proteins. *Mol Cell Proteomics* **7:** 282-289

Rothbauer U, Zolghadr K, Tillib S, Nowak D, Schermelleh L, Gahl A, Backmann N, Conrath K, Muyldermans S, Cardoso MC, Leonhardt H (2006) Targeting and tracing antigens in live cells with fluorescent nanobodies. *Nat Meth* **3:** 887-889

Schotta G, Lachner M, Sarma K, Ebert A, Sengupta R, Reuter G, Reinberg D, Jenuwein T (2004) A silencing pathway to induce H3-K9 and H4-K20 trimethylation at constitutive heterochromatin. *Genes Dev* **18:** 1251-1262

Schotta G, Sengupta R, Kubicek S, Malin S, Kauer M, Callen E, Celeste A, Pagani M, Opravil S, De La Rosa-Velazquez IA, Espejo A, Bedford M, Nussenzweig A, Busslinger M, Jenuwein T (2008) A chromatin-wide transition to H4K20 mono-methylation impairs genome integrity and programmed DNA rearrangements in the mouse. *Genes Dev* **22:** 2048-2061

Schuck P (2003) On the analysis of protein self-association by sedimentation velocity analytical ultracentrifugation. *Anal Biochem* **320:** 104-124

Smallwood A, Esteve PO, Pradhan S, Carey M (2007) Functional cooperation between HP1 and DNMT1 mediates gene silencing. *Genes Dev* **21:** 1169-1178

Sprague BL, Pego RL, Stavreva DA, McNally JG (2004) Analysis of binding reactions by fluorescence recovery after photobleaching. *Biophys J* **86:** 3473-3495

Taddei A, Maison C, Roche D, Almouzni G (2001) Reversible disruption of pericentric heterochromatin and centromere function by inhibiting deacetylases. *Nat Cell Biol* **3:** 114-120

Teif VB, Vainshtein Y, Caudron-Herger M, Mallm JP, Marth C, Hofer T, Rippe K (2012) Genome-wide nucleosome positioning during embryonic stem cell development. *Nat Struct Mol Biol* **19:** 1185-1191

Wachsmuth M, Caudron-Herger M, Rippe K (2008) Genome organization: Balancing stability and plasticity. *Biochim Biophys Acta* **1783:** 2061-2079

Waterston RH, Lindblad-Toh K, Birney E, Rogers J, Abril JF, Agarwal P, Agarwala R, Ainscough R, Alexandersson M, An P, Antonarakis SE, Attwood J, Baertsch R, Bailey J, Barlow K, Beck S, Berry E, Birren B, Bloom T, Bork P et al (2002) Initial sequencing and comparative analysis of the mouse genome. *Nature* **420:** 520-562

Weidemann T, Wachsmuth M, Tewes M, Rippe K, Langowski J (2002) Analysis of ligand binding by two-colour fluorescence cross-correlation spectroscopy. *Single Mol* **3:** 49-61

Zee BM, Levin RS, Xu B, LeRoy G, Wingreen NS, Garcia BA (2010) In vivo residue-specific histone methylation dynamics. *J Biol Chem* **285:** 3341-3350

Zolghadr K, Mortusewicz O, Rothbauer U, Kleinhans R, Goehler H, Wanker EE, Cardoso MC, Leonhardt H (2008) A fluorescent two-hybrid assay for direct visualization of protein interactions in living cells. *Mol Cell Proteomics* **7:** 2279-2287